pearl
Preparing for Extreme And Rare events in coastaL regions

# D2.4 The effectiveness of integrated modelling/hazard assessment framework performed in the case study work

*Work Package 2*

*Authors: ICL, MPG, CAM, TUHH, SINTEF*

*Contributing Authors:* Savre, Julien; Herzog, Michael; Dreier, Norman; Peter Froehle; Pain, Christopher; Fang, Fangxin; Sjur Kolberg

Dissemination level:
**PP** = Restricted to other program participants (including the Commission Services).



*Acknowledgement*
The research leading to these results has received funding from the European Union Seventh Framework Programme (FP7/2007-2013) under Grant agreement n° 603663 for the research project PEARL (Preparing for Extreme And Rare events in coastaL regions).

*Disclaimer*
The deliverable D 2.4 reflects only the authors' views and the European Union is not liable for any use that may be made of the information contained herein.

## Document Information

| Project Number | ***603663*** | Acronym | **PEARL** |
|---|---|---|---|
| Full Title | Preparing for Extreme and Rare events in coastal regions | | |
| Project URL | http://www.pearl-fp7.eu/ | | |
| Document URL | | | |
| EU Project Officer | Denis Peter | | |

| Deliverable | Number | D2.4 | Title | A report describing the effectiveness of integrated modelling/hazard assessment framework performed in the case study work |
|---|---|---|---|---|
| Work Package | Number | WP2 | Title | |
| Lead Author(s) | Fangxin Fang; Christopher Pain | | | |
| Contributing Author(s) | Savre, Julien; Herzog, Michael; Dreier, Norman; Peter Froehle; Pain, Christopher; Fang, Fangxin; Sjur Kolberg | | | |

| Date of Delivery | Contractual | 01.01.2016 | Actual | 30.04.2018 |
|---|---|---|---|---|
| Status | Final | | final □ | |
| Nature | prototype □ report **Y** dissemination □ | | | |
| Dissemination level | public □ consortium **Y** | | | |

| Abstract (for dissemination, 100 words) | |
|---|---|
| Keywords | |

| Version Log | | | | |
|---|---|---|---|---|
| Issue Date | Rev. No. | Author | Change | Approved by |
| | | | | |
| | | | | |
| | | | | |
| | | | | |
| | | | | |
| | | | | |

# A report describing the effectiveness of integrated modelling/hazard assessment framework performed in the case study work

## Contents

# 1 Summary

## 1.1 Aims

The aim of work package 2 is to develop an integrated modelling/hazard assessment framework (atmosphere/ocean/waves/flooding) based on advanced numerical techniques (adaptive unstructured mesh, advanced finite element types, adaptive time schemes and adaptive spectral wave, for example). This integrated modelling/hazard assessment framework has been applied to Denmark case. The effectiveness of integrated modelling/hazard assessment framework performed in the case study work has been described in detail (Chapter 2) and integration of models for individual and coinciding flooding events in Chapter 3.

Our key achievements are:

1. Development and applications of a new integrated modelling framework (including a new multiscale adaptive unstructured atmospheric model, Spectral wave model, flooding model) for hazard assessment (Chapters 2 and 3);
2. Development of a multi-scale integrated urban flooding modelling framework which has the capabilities for one dimensional (1D), two-dimensional (2D) and three-dimensional (3D) flooding modelling. It has an adaptive multi-scale mesh spatially and temporally and the necessary coupling abilities to simulate individually and coincidence of urban pluvial (heavy precipitation) and coastal flooding (high sea level) (Chapter 3);
3. Application of the new 3D urban flooding model to a Glasgow flooding event in 2002 (Chapter 3.3);
4. Modelling extreme urban flooding events individually and in coincidence for the Greve case study. A comparison of results from the new integrated urban flood inundation model (Fluidity) and the MIKE Urban flooding model (a widely used commercial flooding software) has been carried out (Chapter 3.4).
5. Nine journal papers have been accepted or submitted or written (6 published, 2 in review, 1 submitted), 3 conference presentations;
6. The first 3D flooding model and application to the Glasgow flooding event;
7. The first adaptive unstructured mesh flooding model with cutting-edging numerical techniques (adaptive unstructured mesh, adaptive time stepping and parallel computing) (two papers have been submitted, Hu et al. 2017 a and 2017b, one of them (Hu et al. 2017 a) is in revision);
8. The first high order control-volume mesh to mesh interpolation method applied to arbitrary 2 or 3D meshes. This is critical for conservation and accurate coupling of natural hazard models. Paper published in journal of computational physics and has been one of the most downloaded papers within the journal over the last 6 months.

# 2 An integrated modelling/hazard assessment framework and application to Denmark case (Contribution from the University of Cambridge and Hamburg University of Technology)

## 2.1 Introduction

Within PEARL, the SWAN model (Booij, N., et al, 1999) has been used to analyse wave conditions on different temporal and spatial scales from the long-term overall wave conditions at the ocean model scale to the local extreme event wave conditions at the scale of the flood protection constructions. The input for SWAN is generated by the atmospheric model (ATHAM-Fluidity). Temporal and regional distributions of the wind with a time resolution of one hour are used for the simulation of the wave spectrum with SWAN.

The ATHAM Fluidity model developed here is a novel adaptive multi-scale multi-physical atmospheric modelling framework for extreme events and enable the accurate simulation of heavy precipitation events that are contributing to flooding in coastal areas as well as providing the necessary forcing to generate storm surges and wind waves, see Figure 1.1 and report D2.2 detailing the framework.

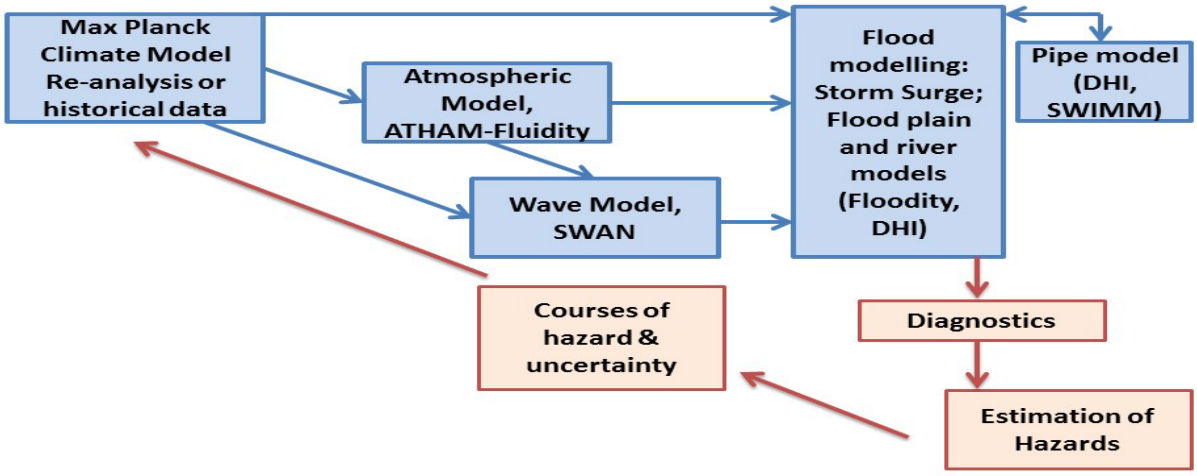


***Figure 1-1*** - One way coupling between the modelling components assumed in this work

## 2.2 Two Extreme Events

The integrated modelling framework described in this section is tested on the following two extreme events for the Greve cast study site. These two events were extracted from the free-running historical simulation performed with Max Planck's REMO climate model. It should be noted that although the REMO simulation included appropriate external forcings of greenhouse gas concentrations and solar and volcanic activity representative of the simulation period, it was not forced by reanalysis data, and so these events did not occur in reality.

- ***Extreme precipitation event – 18 August 1966***: This event was characterised by a cyclonic low pressure system centred over the Baltic Sea, bringing significant convective and frontal precipitation and North-Westerly winds over Greve. Around 70 mm of rain fell during this day.
- ***Extreme sea level event – 5 February 2000***: This event was caused by a succession of low-pressure systems moving Eastwards across Europe, which resulted in the near-surface winds over Denmark veering from a strong Westerly/North-Westerly flow in the period before the extreme (causing water to pile up in the Baltic Sea) to a weaker Southerly wind on the day of

the extreme (releasing this water back towards Greve). The maximum sea level anomaly was 98.9 cm.

### 2.2.1 Extreme Precipitation Event

This event was selected from the 10 events within the 45-year free-running REMO simulation (1960-2005) that produced the most extreme daily precipitation amounts (i.e. the accumulated 24-hr value) at the REMO grid point closest to Greve, for which MPI provided the NetCDF data files. The total duration of each data file is 5 days, centred on the day that contains the extreme. Note that the grid cell containing Greve in the REMO model (from which the precipitation values were extracted) has a horizontal extent of around 50 x 50 km. The extreme event that occurred on 18/08/1966 has been selected for the following reasons:

- The extreme ranks fairly highly (3rd) amongst the 10 possibilities in terms of total cumulated daily precipitation at Greve.
- There is a significant convective precipitation component as well as large-scale precipitation component to the event. Convective processes are particularly difficult to capture in large-scale models that must rely almost entirely on their convective parameterisation, whereas higher-resolution large-eddy simulation models can directly resolve more of the processes leading to convective precipitation. This event therefore provides an opportunity to test the added value of using PEARL's higher resolution models to dynamically downscale the larger-scale model simulation.

**Figure** 2-2 shows the synoptic situation over the course of the chosen extreme day (in increments of 6hrs) through the evolution of the large-scale and convective precipitation fields (contours) and near-surface wind fields (overlain vectors). Although coastal outlines are not shown in these rotated latitude-longitude plots, the area covered is roughly from Eastern UK to Estonia (W-E) and from South Germany to Central Norway (S-N). The location of Greve is shown by the red dot near the centre of each plot. It can be seen that this event is associated with a cyclonic low pressure system centred over the Baltic Sea, bringing significant convective and frontal precipitation and North-Westerly winds over Greve.

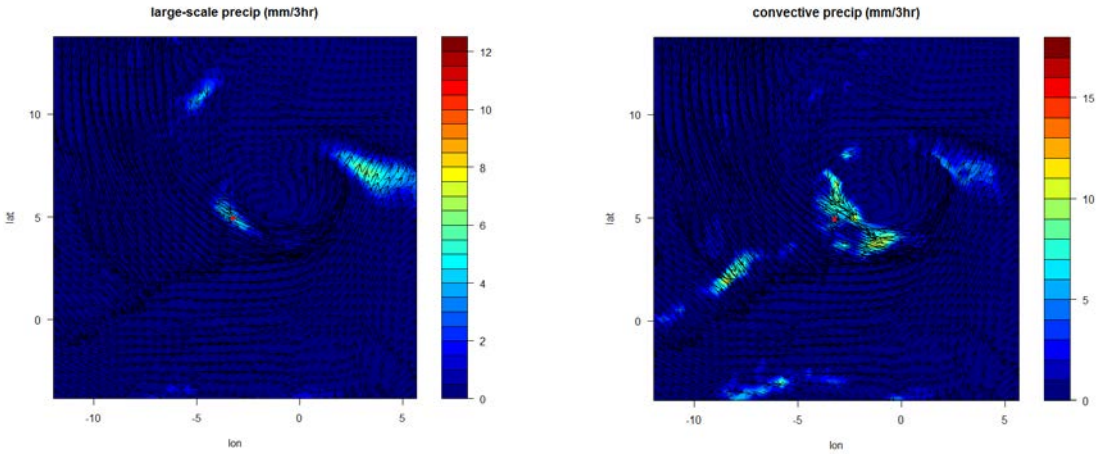


18/08/1966, 00:00

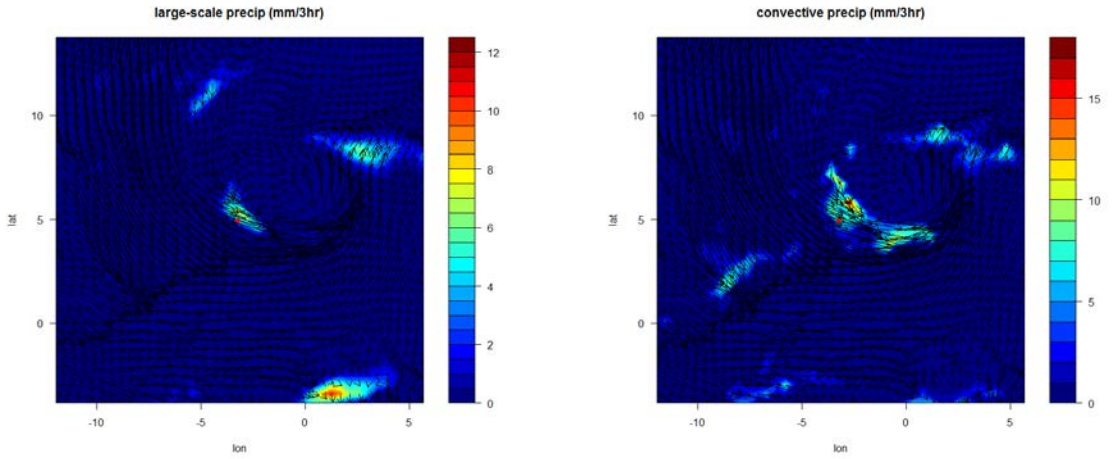


18/08/1966, 06:00

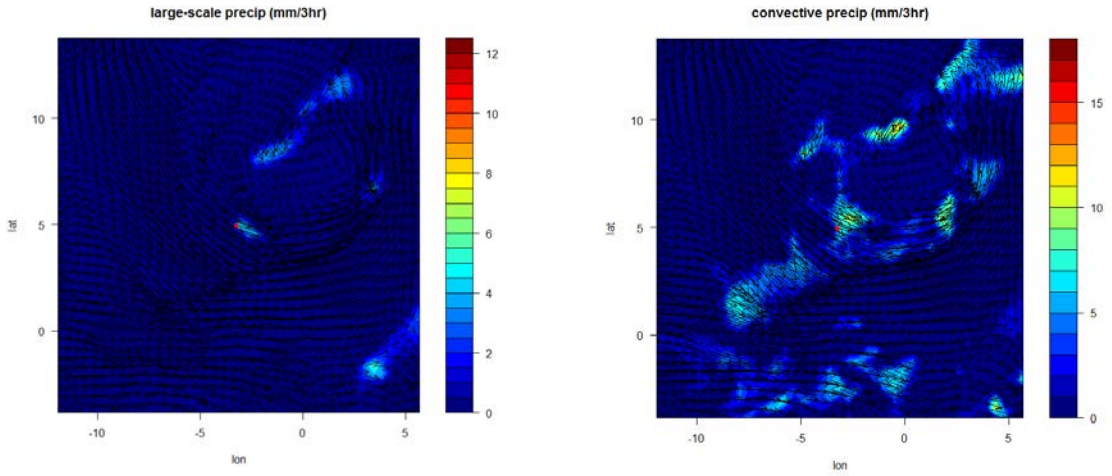


18/08/1966, 12:00

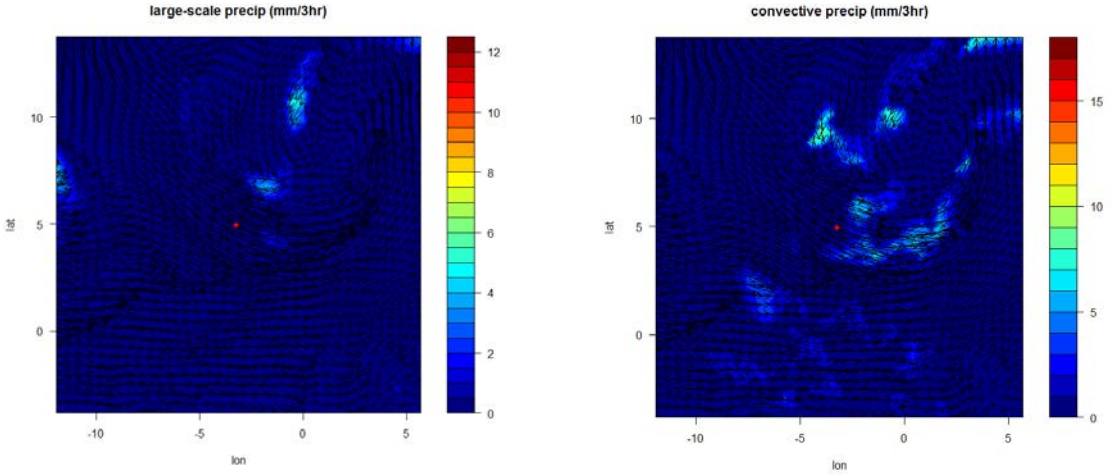


18/08/1966, 18:00

***Figure** 2-2 - Evolution of synoptic conditions during the day of the precipitation extreme. Contours: large-scale (left panels) or convective (right panels) precipitation fields. Vectors: Near-surface velocity fields. Red dot: location of Greve.*

**Figure** 2-3 shows a time-series of precipitation and accumulated precipitation (both large-scale, convective and total) for the grid cell containing Greve, over the entire 5-day period (centred on the day of the precipitation extreme, which is indicated by the vertical grey lines). During the day of the

extreme, the cumulated total precipitation was 68.2 mm, with REMO attributing 26.2 mm to large-scale precipitation and 42 mm to convective precipitation.

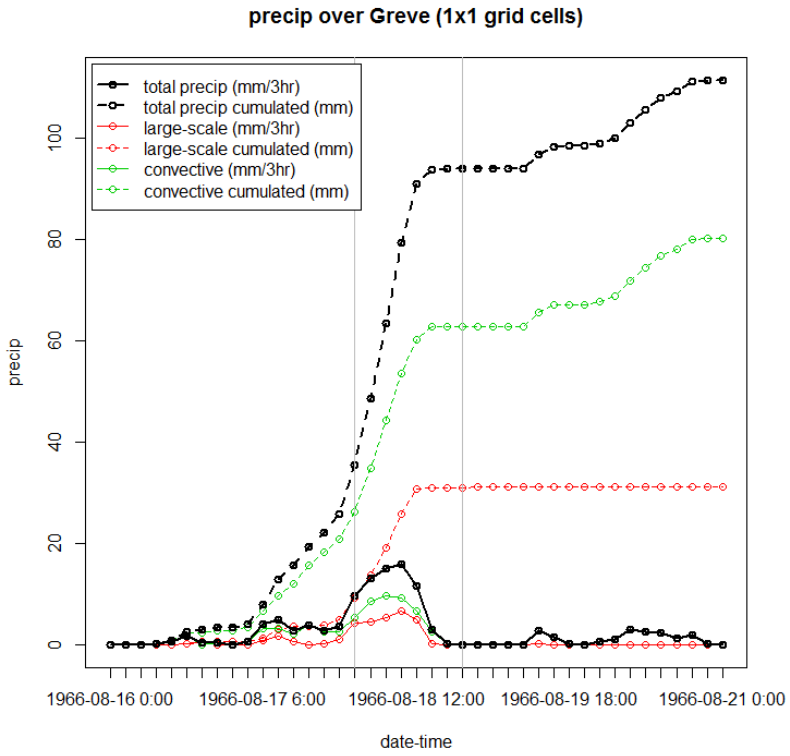


***Figure** 2-3 - Precipitation time series over the 5-day period centred on the day of the extreme (indicated by vertical grey lines)*

### 2.2.2 Extreme Sea-Level Event

This event was selected from the 8 events within the 45-year free-running REMO simulation (1960-2005) that produced the highest sea-levels at the REMO grid point over water that is closest to Greve, for which MPI again provided the NetCDF data files. Again, the total duration of each data file is 5 days, centred on the day that contains the extreme. The extreme event that occurred on 05/02/2000, with a maximum sea level of 98.9 cm, has been selected. Although this event ranked only 7$^{th}$ out of the 8 most extreme sea-level events, it was selected for the following reasons:

- The processes leading to the extreme sea-level maximum are fairly typical and well interpretable: The strong Westerly and North-Westerly winds on the days prior to the extreme caused water to pile up in the Baltic Sea, which was then released back towards Greve on the day of the extreme as the winds veered to a weaker Southerly flow.
- This event also produced the most significant precipitation on the day of the extreme out of the 8 most extreme sea-level events (8.5mm). This precipitation in combination with the high sea levels will exacerbate local flooding problems and is therefore arguably of more interest in the context of PEARL.

**Figure** 2-4 shows a time-series of near-surface wind speed and direction at the REMO grid point closest to Greve for the two days prior to, and the day of, the selected sea level extreme. It can be seen that strong North-Westerly winds on the day before the extreme weaken significantly on the day of the extreme, allowing the water that has been forced into the Baltic Sea through the Great Belt strait to travel back towards the North Sea (gravity-driven current). The wind also veers to a more Southerly direction, aiding this movement of water.

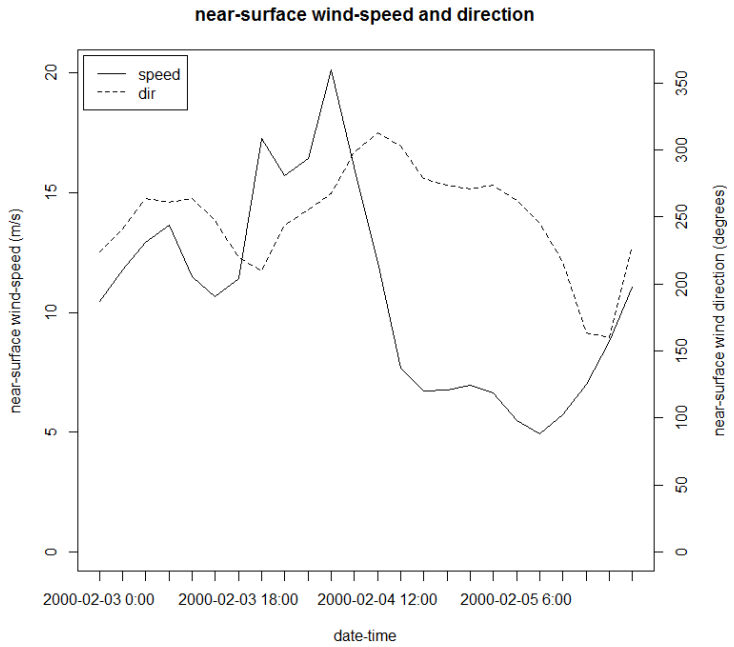


***Figure** 2-4 – Time series of near-surface wind speed and direction over Greve on the two days prior to, and the day of, the extreme sea-level event.*

**Figure** 2-5 shows the time-series of precipitation and accumulated precipitation (both large-scale, convective and total) for the grid cell containing Greve, over the entire 5-day period (centred on the day of the precipitation extreme, which is indicated by the vertical grey lines). During the day of the extreme, the cumulated total precipitation was 8.5 mm, although the value is closer to 15 mm if the first couple of output times from the next day are also included. This rain is attributed by REMO as entirely convective precipitation.

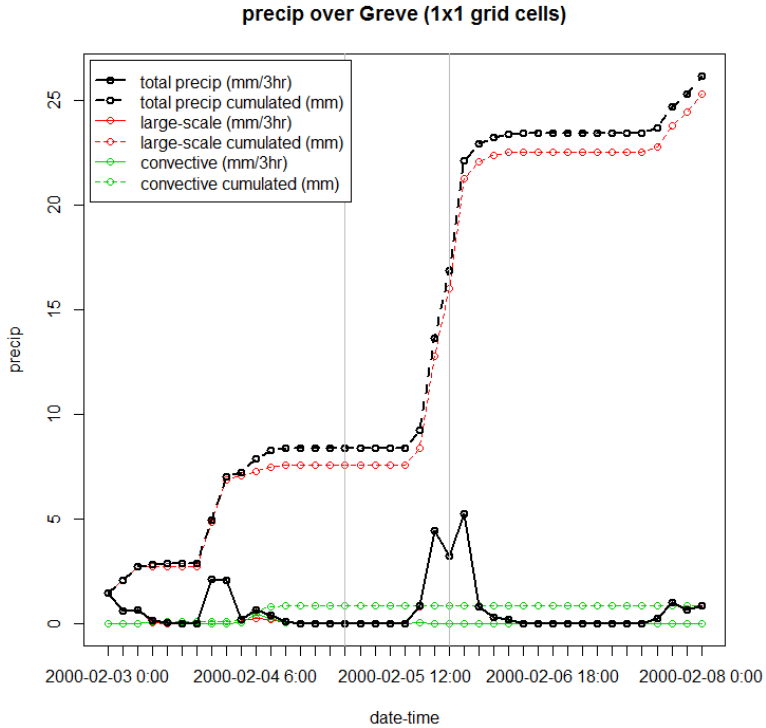


***Figure** 2-5 - Precipitation time series over the 5-day period centred on the day of the extreme (indicated by vertical grey lines)*

**Figure** 2-6 again shows the synoptic situation (through large-scale precipitation and near-surface wind fields) over the two days prior to, and the day of, the selected sea level extreme (in increments of 9hrs). The location of Greve is again shown by a red dot. It can be seen that the strong Westerly and then North-Westerly winds over Greve the day before the extreme are associated with a cyclonic low pressure system centred over the Baltic Sea, which then passes away to the East, leaving weaker Westerly winds behind it, which later veer to a more Southerly wind as a second weaker low pressure system forms and passes Northward just to the West of Greve.

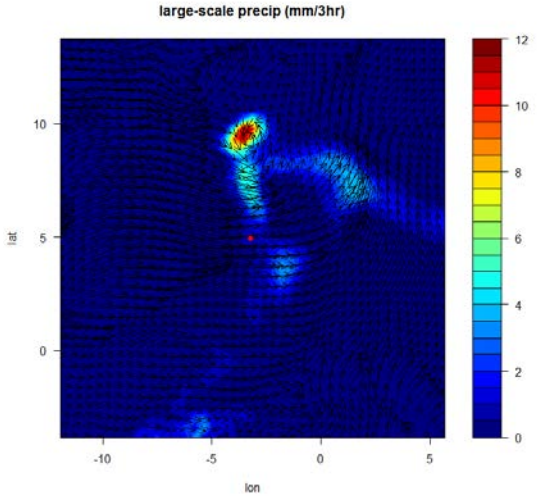


03/02/2000, 06:00

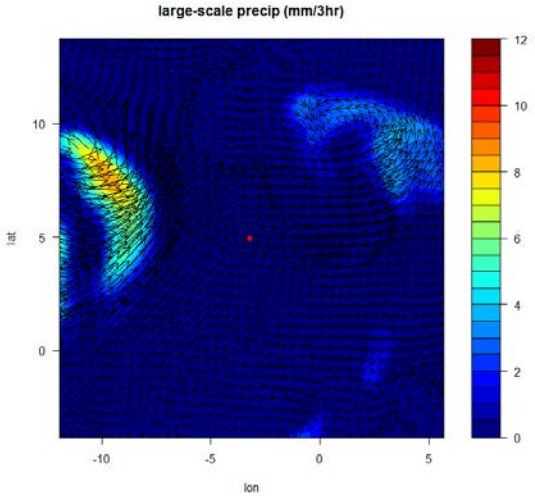


03/02/2000, 15:00

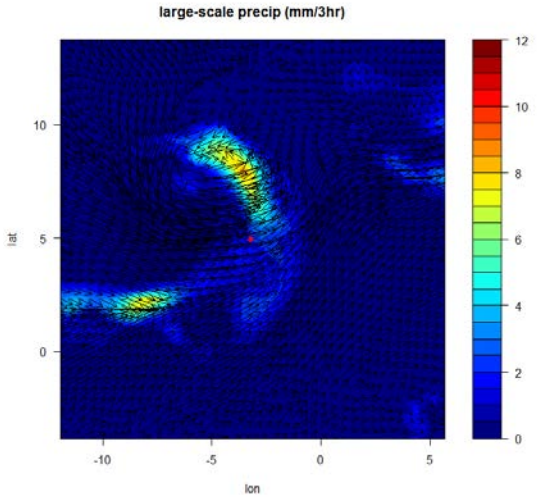


04/02/2000, 00:00

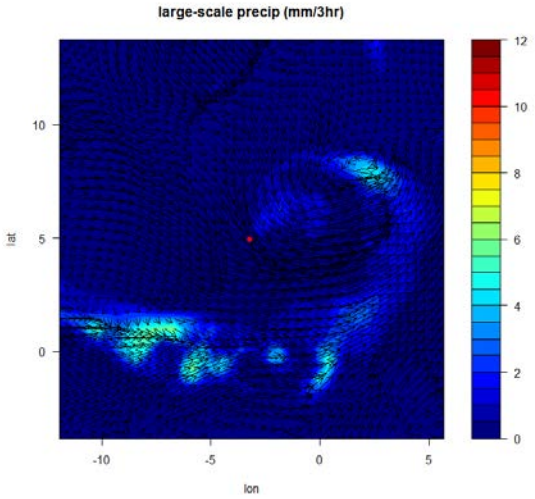


04/02/2000, 09:00

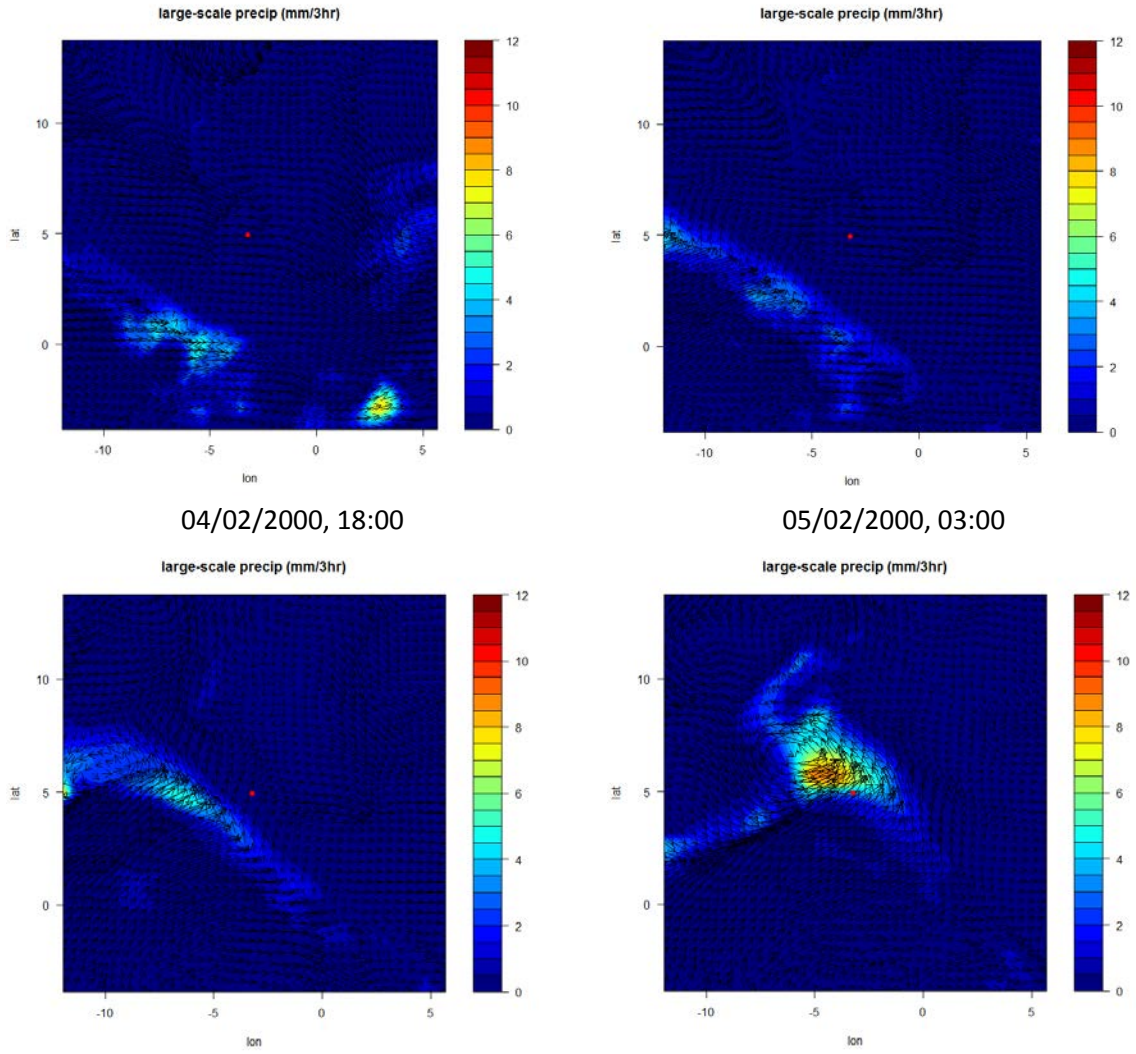


04/02/2000, 18:00 05/02/2000, 03:00

05/02/2000, 12:00 05/02/2000, 21:00

***Figure** 2-6 - Evolution of synoptic conditions during the two days prior to, and the day of, the sea-level extreme. Contours: convective precipitation fields. Vectors: Near-surface velocity fields. Red dot: location of Greve.*

## 2.3 Coupling to Waves

### 2.3.1 The SWAN wave model

TU Delft (Booij et al. 1999) has developed the third generation, phase averaged spectral wave model "Simulating Waves Nearshore" (SWAN). SWAN computes wind generated waves and is particular useful for the modeling of waves in larger model domains and in shallow water regions. The model accounts for the following main physics of the generation, propagation, interaction and dissipation of waves: (i) wave generation by wind (ii) wave propagation in time and space (iii) shallow water processes like shoaling, refraction due to current and depth (iv) tree- and four-frequency wave-wave interactions (v) frequency shifting due to currents and non-stationary depth and (vi) wave energy dissipation due to white-capping, depth-limited breaking, bottom friction, vegetation etc. A finite difference method is used for the discretization of the governing equations (e.g. spectral description of wind waves and the propagation of wave energy). The model is able to operate on regular and curvilinear grids or triangular meshes in Cartesian or spherical coordinate systems. Non-stationary resp. stationary runs can be carried out and both linear and non-linear deep- and shallow-water influenced processes are included in the computations.

For practical calculations, the model can be operated in serial mode or in a parallelized version on single- or multi-processor machines with shared or distributed memory.

SWAN is an open Source Model and the model itself as well as the model documentation is available from the SWAN website: http://swanmodel.sourceforge.net.

For the calculation and the assessment of the wave conditions in the Greve case study area SWAN was applied in the version 41.10 that was available at the start of the model set-up. At the time of this report the version 41.10A become available which has some minor changes that are not relevant for the calculation of the waves. An overview about the changes of the program is given on the SWAN homepage[1].

### 2.3.2 Climate to Waves

For the demonstration of the implementation of SWAN into the integrated modelling framework, a SWAN wave model chain was set up for the Baltic Sea and the Koge ares. Since results from ATHAM-Fluidity have not been readily available during the model set-up phase, the wind fields of the regional climate model 'REMO' are used in a first step for the forcing of the SWAN wave model (offline coupling). The near surface horizontal wind vector components (u and v) at 10 meters height above the surface that are needed by SWAN were directly output in the REMO simulations from MPI-M and not processed afterwards. The wind data are available on a rotated spherical grid with a timestep of 3 hours.

The wave model chain consists of three sub-models (domains): i) a coarse model covering the complete Baltic Sea, ii) a finer model for the south-western Baltic Sea area and iii) a high-resolution wave model for the Koge Bay.

As just mentioned, the wave model on the basis of SWAN has been set up and split up into 3 domains. The coarse model (model name: **B**altic **S**ea **S**tate Model in **C**limate Mode=**BSSC**) covers the whole Baltic Sea area and provides the wave boundary conditions for a nested fine model (cp. red box in **Figure** ). The domain of the BSSC model and the initial water depths at the start of the simulations 2000-02-03 00:00:00 UTC are shown in **Figure** 2-6.

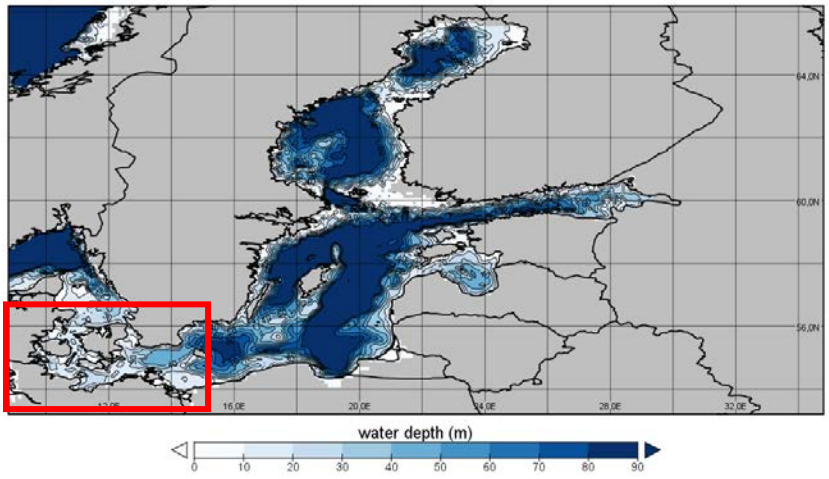


***Figure 2-6** – BSSC model domain and water depths on 2000-02-03 00:00:00 UTC and WBSSC model domain indicated with a red box*

[1] http://swanmodel.sourceforge.net/modifications/modifications.htm

The bathymetry of the model is based on the ETOPO1 grid data set (Amante, C. and B. W. Eakins 2009) that was also used within the MPI-OM simulations of MPI-M. The ETOPO1 grid data provides information about the topography of the Baltic Sea on a regular geographical grid with a horizontal resolution of one arc-minute (approx. Δx~1.0km, Δy~1.9km at 55.5292°N).

Moreover, information about the local sea level from the historical run of the MPI-OM are used as input for the wave model. The sea level data are available on a rotated spherical grid (compare **Figure** 2-7) and the horizontal resolution ranges between 5 km in the North Sea and 220 km in the Antartic (Sein et al. 2015).

The sea level data during the period of the extreme event on 2000-02-05 have been provided by CAM. Due to the fact that the sea level data from MPI-OM only contain the dynamic component of the sea level, the non-dynamic component (e.g. from global thermal expansion, glacial isostatic adjustment etc.) are added under the assumption that the non-dynamic component do not vary significantly within the study area and over the time of the extreme event. The difference between the extreme sea level of w=0.989m above MSL and the sea level from the historical MPI-OM run on the date of the extreme event was calculated (Δw=0.265m) and added as a constant value to the sea level data from the historical MPI-OM run.

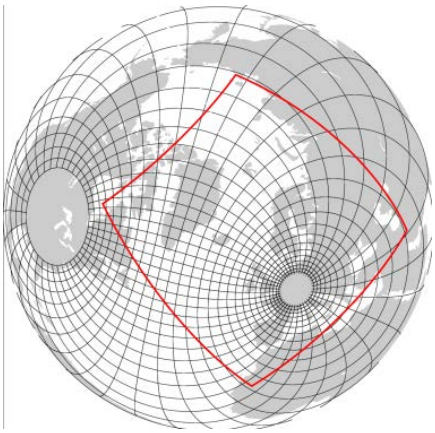

***Figure 2-7** – MPI-OM model grid (every 15$^{th}$ line is shown), the red box indicates the coupled domain REMO/MPI-OM (from Fig. 2 in Sein et al. 2015)*

The coarse wave model is run on an hourly basis and with a high horizontal (Δx~6.3km, Δy~11.1km at 55.5292°N) and directional resolution (ΔΘ=2.5°) with 42 frequencies ($f_{low}$=0.05 Hz, $f_{high}$=1 Hz).

The bathymetric and sea level data have been remapped onto the corresponding computational grids of the wave model using distance-weighted average remapping (CDO utilities of MPI-M).

The wind data have been remapped (bilinear interpolation) onto a grid with a coarse horizontal resolution (Δx~12.6km, Δy~22.2km at 55.5292°N) and are finally remapped by SWAN onto the corresponding computational grids of the wave model using bilinear interpolation.

The second, fine wave model (model name: **W**estern **B**altic **S**ea **S**tate Model in **C**limate Mode=**WBSSC**), with a horizontal resolution of one arc-minute (in correspondence to the resolution of the ETOPO1 data set) that covers the area of the Western Baltic Sea is nested into the coarse model and provides the wave boundary conditions for a fine local model that covers the Køge bay (cp. red box in **Figure** 2-8). The domain of the WBSSC model and the initial water depths at the start of the simulations 2000-02-03 00:00:00 UTC are shown in **Figure** 2-8.

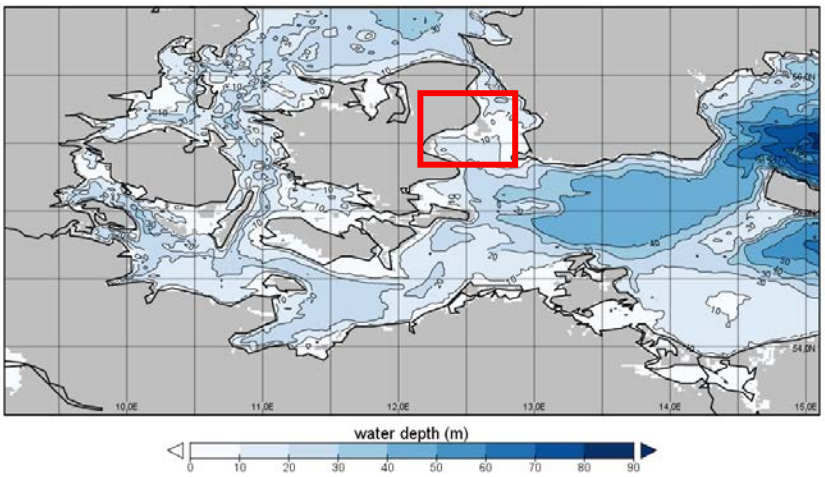


***Figure 2-8** – WBSSC model domain and water depths on 2000-02-03 00:00:00 UTC and GSSC model domain indicated with a red box*

The third sub-model, a high-resolution local wave model (model name: **G**reve **S**ea **S**tate Model in **C**limate Mode=**GSSC**) has been set-up with a high horizontal resolution of approx. Δx~100m, Δy~100m at 55.5292°N and is nested into the fine model WBSSC. The location of the computational grid as well as the horizontal resolution have been chosen in accordance with the test data of the ATHAM-Fluidity model on a regular geographical grid. The domain of the GSSC model and the initial water depths at the start of the simulations 2000-02-03 00:00:00 UTC are shown in **Figure** 2-9. The approximate location of Greve (55.583° N; 12.3°E) is indicated in **Figure** 2-9 by a black dot.

Some parts of the coastline exemplarily southwest near Greve are missing in the wave model (as indicated in **Figure** 2-9 with grey colour). This is a result of the remapping from the relatively coarse horizontal resolution of the MPI-OM grid to the high horizontal resolution of the GSSC grid.

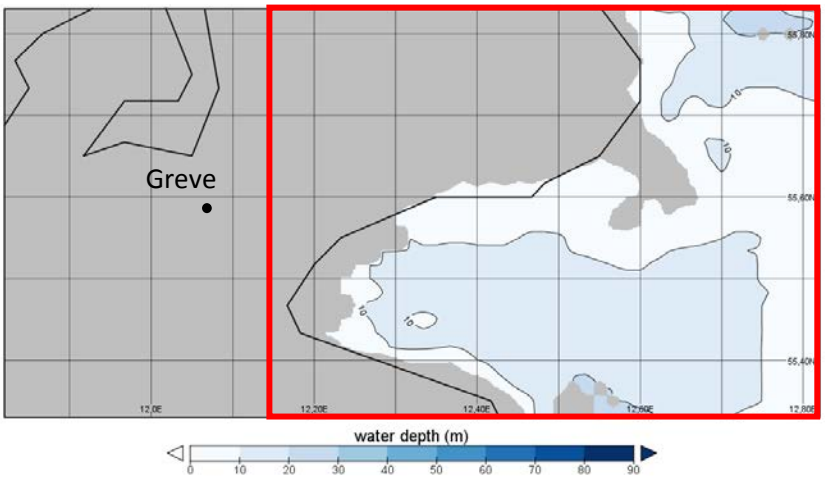


***Figure 2-9** – GSSC model domain (red box) and water depths on 2000-02-03 00:00:00 UTC*

In the wave simulations the significant wave height ($H_s$), mean wave periods ($T_{m01}$, $T_{m02}$), spectral period ($T_{m-1.0}$), peak period ($T_p$) and mean wave direction ($\theta_m$) and the directional spreading of the wave direction (dspr) are output together with the water depth, sea level and wind information at every grid point in the corresponding wave model domain (BSSC, WBSSC or GSSC). The output was written into a system independent binary NetCDF format. Moreover, time series of the wave parameter, water depth, sea level and wind have been output in a ASCII-(text) format at selected

locations near the 10m water depth isoline (compare **Figure** 2-10) which are located approx. 4km ('Koege_08'), 8km ('Koege_13') and 12km ('Koege_18') in front of the coastline of Greve.

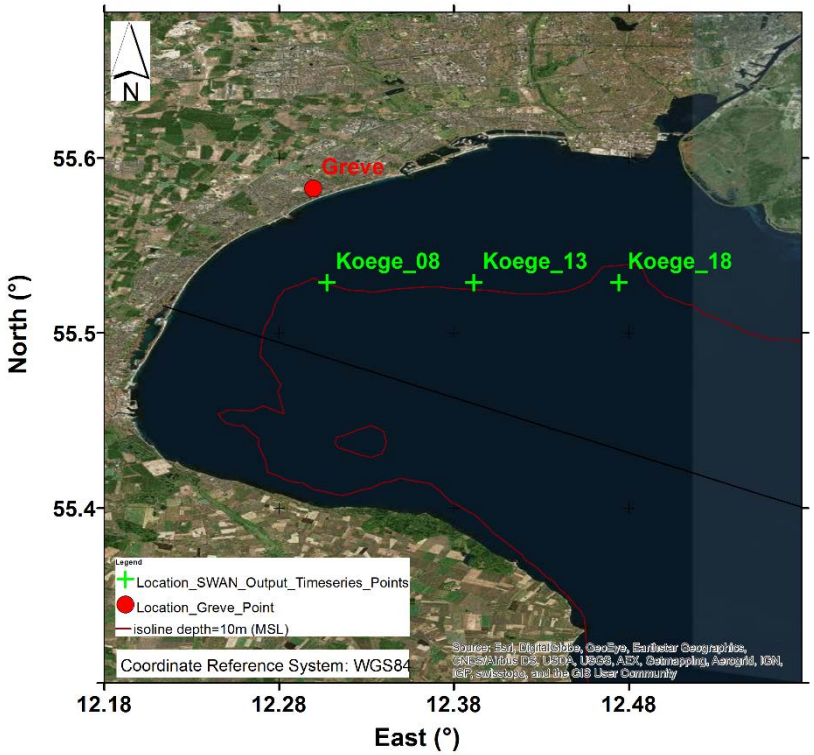


***Figure 2-10** – Køge Bay and locations of Greve (red point) and selected points for wave model output (green crosses) near the 10m water depth isoline (red line)*

## 2.4 Coupling to ATHAM-Fluidity

### 2.4.1 Climate to ATHAM-Fluidity

ATHAM-Fluidity has been developed to allow a simulation to be driven by output from Max Planck's regional climate model 'REMO'. The horizontal resolution of the REMO model simulations performed for PEARL is around 50 km, which is comparable to the extent of the entire ATHAM-Fluidity model domain. It is therefore appropriate to drive ATHAM-Fluidity using vertical profiles extracted from the single REMO grid column over Greve. This methodology is typical of LES models driven by larger (meso)scale models. The first step in the coupling procedure is therefore to identify and extract the REMO data within this column. The REMO model is run on a staggered rotated grid system, as shown in Figure 2-11 (left). The right panel shows the same region with the rotated coordinates converted back to actual latitude and longitude. In both panels, the red dot shows the approximate location of Greve (latitude, longitude = 55.57N, 12.29 E) as well as the staggered grid points closest to this location that the relevant atmospheric vertical profiles should be extracted from.

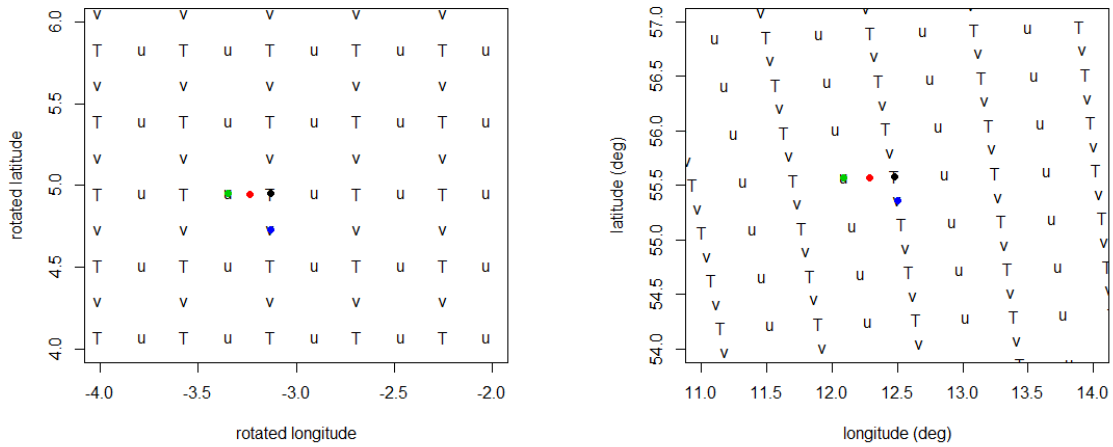


***Figure** 2-**11** - Rotated (left) and unrotated (right) staggered REMO model grid close to Greve. Symbols T, u and v indicate where the scalars, West-East and South-North components of the velocity vector are solved on the staggered grid, respectively. The red dot indicates the approximate location of Greve, and the black, green and blue dots indicate which grid points the relevant atmospheric vertical profiles should be extracted from.*

The REMO data are in netCDF format, and so a CDO (climate data operator; https://code.zmaw.de/projects/cdo) can be used to extract the appropriate vertical profiles, namely:

```
$ cdo sellonlatbox,-3.36,-3.12,4.72,4.96 ifile ofile
```

where the numbers after the keyword 'sellonlatbox' define a rectangle (in rotated coordinates) that encloses the three staggered grid points from which the vertical data is to be extracted, 'ifile' would be the name of the original netCDF file and 'ofile' the name of the netCDF file containing only the selected vertical profile data.

The next step in the coupling procedure is to convert the netCDF vertical profile data into the format expected by ATHAM-Fluidity. This format comprises a tab-delimited ASCII file with the following structure:

- The first line should contain the following five values: Surface pressure (hPa), sea-surface potential temperature (K), specific water (vapour + liquid) content at the lowest grid point (g/kg), two dummy variables currently set to zero.
- The remaining lines should contain the following five columns that define the vertical profiles: Height above ground (m), modified potential temperature (K), specific water (vapour + liquid) content (g/kg), wind velocity magnitude (m $s^{-1}$), a dummy variable currently set to zero.

This conversion step is currently performed by a script written in the R programming language. It is planned to create an equivalent python script so that it can be included with the open-source release of ATHAM-Fluidity (Deliverable 2.5, due month 48), allowing all model users can make use of this conversion tool.

The surface pressure is extracted directly from the REMO netCDF file (variable PS). The sea-surface potential temperature is calculated from the REMO variable TSW (sea surface temperature) using the standard conversion:

$$\theta = T\left(\frac{p_0}{p}\right)^{R_d/c_p},$$

where the reference pressure $p_0 = 1000$ hPa, $p$ is taken to be the surface pressure $p_S$ in this case, and the dry gas constant $R_d$ and specific heat at constant pressure $c_p$ are taken to be 287.04 and 1004.64 respectively. Note that the REMO data are specified on hybrid sigma pressure levels rather than actual heights. To convert from one to the other, the sigma pressure levels are first converted to pressure using:

$$p = a_m + b_m p_S,$$

where $a_m$ and $b_m$ are the two hybrid coefficients at layer midpoints. These pressures are then converted to heights by assuming an exponential vertical profile of pressure of the form:

$$p = p_S e^{-z/H},$$

where the scale height $H$ is taken to be 7000 m.

The specific water (vapour + liquid) content is calculated as the sum of the REMO variables QD (specific vapour content) and QW (liquid water content). The reason that they are combined is that the REMO model and ATHAM-Fluidity will have slightly differing internal thermodynamics calculations, and so the point of saturation at any given height will also be slightly different. The safest procedure is thus to pass the total water content to ATHAM-Fluidity as assumed water vapour and then allow the model's internal thermodynamics algorithm to decide the point of saturation and subsequently how much of this vapour should condensed out to liquid water. However, any condensation within the thermodynamics algorithm will also lead to an increase in internal energy (due to the release of latent heat) and thus an increase in the potential temperature. It is therefore important to pass a modified potential temperature to ATHAM-Fluidity, i.e. the potential temperature that would be obtained if all the liquid water in the air were to be evaporated. Thus, for saturated air, the modified potential temperature will be lower than the actual potential temperature by an amount that is equal to the increase in potential temperature expected to occur as a result of condensation in the internal thermodynamics calculations. The algorithm to perform this modification is as follows:

- Estimate the surface air density using the ideal gas law for moist air, i.e. $p_S = \rho_S R_d T_v$, where $T_v = (1 + 0.61w)$ is the virtual temperature at the lowest grid point and $w$ is the specific vapour content at the lowest grid point.
- For each height $i$ above the surface:
  - Initialise the pressure at this height to be the pressure at the height below, $p_{iter} = p_{i-1}$.
  - Use the ideal gas law for moist air, $p = \rho R_d T_v$, and the hydrostatic equation, $\partial p/\partial z = -g\acute{\rho}$, to iteratively calculate the actual density and pressure at this height, i.e.

    Iterate 9 times:
    - $\rho_{iter} = p_{iter}/R_d\, T(1 + 0.61w)$
    - $p_{iter} = p_{i-1} - g(z_i - z_{i-1})\,(\rho_{iter} + \rho_{i-1})/2$

    Set $p_i = p_{iter}$ and $\rho_i = \rho_{iter}$ ready for the next $i$ loop
  - Calculate potential temperature at this height using the equation:

$$\theta_i = T_i \left(\frac{p_0}{p_i}\right)^{R_d/c_p} - \frac{LWC \times L_v}{c_p \Pi},$$

    where $LWC$ is the liquid water content of the air (kg/kg) and $L_v$ is the specific latent heat of vaporisation (i.e. the heat $q$ required to evaporate 1kg of water). Thus, $LWC \times L_v$ is the specific heat required to evaporate all the liquid water in the air. Dividing this by $c_p$ converts this to a temperature loss (since $c_p = (dq/dT)_{pconst}$),

and finally dividing through by the Exner function $\Pi = (p_0/p)^{R_d/c_p}$ converts this to a potential temperature loss, which is the required value.

Finally, it is noted that at present the horizontal wind components from the REMO model are used to calculate the wind velocity magnitude, which is then assumed by ATHAM-Fluidity to be the $x$-component of the wind velocity, with the $y$-component set to zero. In other words, the LES model assumes a non-veering perpendicular wind at the inlet. This was found necessary to avoid spurious behaviour near the inlet during the simulation. Future developments are planned to allow the use of full veering wind vectors at the inlet.

### 2.4.2 ATHAM-Fluidity to Waves

The SWAN wave model requires 10 m wind fields (horizontal components) as input. These fields can either be taken directly from a REMO climate model simulation, or from a downscaled ATHAM-Fluidity simulation. The REMO model simulations performed for PEARL have a spatial resolution of around 50 km and are provided at 3-hourly intervals. The ATHAM-Fluidity simulations have a much finer spatial resolution and can be provided at time intervals down to the model time-step, which is typically on the order of 1-10 seconds. However, this temporal resolution is excessively fine for the SWAN model and so it is first necessary to temporally average the ATHAM-Fluidity velocity fields onto an appropriate time interval, e.g. hourly. This may seem counter-productive given that the initial simulation is run with a much smaller timestep, however the premise is that by simulating down to scales that can explicitly resolve the most energetic 3-D turbulent motions within the lower atmosphere, the time-averaged (2-D) fields will be more accurate than the fields from a coarser regional model, and may also be able to capture any important spatial variations that the regional model cannot.

Additionally, the SWAN model requires the 10 m wind fields in netCDF format on a regular grid. However, ATHAM-Fluidity fields are written out in *.vtu (unstructured vtk) format on an irregular grid (in fact, the vtu data correspond to values at the nodes of the unstructured, and potentially adaptive, finite element mesh). It is therefore also necessary to interpolate the ATHAM-Fluidity output data onto a regular grid and then write these fields to files in netCDF format.

A python script has been written to perform the post-processing steps described above, namely:

- Read a sequence of vtu files from an ATHAM-Fluidity run
- Interpolate the velocity data onto a structured two-dimensional grid at 10 m (with resolution prescribed by the user).
- Calculate the time-averaged velocity fields (with the averaging time interval prescribed by the user)
- Write out time-averaged velocity fields to a netCDF file, along with the latitude and longitude of each grid point so that the fields are georeferenced. The latitude and longitude are calculated from the gridded $x, y$ coordinates using:

$$lat = lat_{mid} + \frac{sin\left(\frac{\theta\pi}{180}\right)x - cos\left(\frac{\theta\pi}{180}\right)y}{lat_{1^o}}$$

$$lon = lon_{mid} + \frac{cos\left(\frac{\theta\pi}{180}\right)x - sin\left(\frac{\theta\pi}{180}\right)y}{lon_{1^o}}$$

where $lat_{mid}$, $lon_{mid}$ and $\theta$ are, respectively, the latitude and longitude of the ATHAM-Fluidity modelling domain midpoint (in decimal degrees) and the angle through which the domain is rotated (in degrees; anticlockwise is positive), which are all parameters that are specified by the model user during simulation setup (e.g. see section 3.4.3). $lat_{1^o}$ and $lon_{1^o}$ are the distances (in metres) of one degree latitude and longitude, respectively, taken to be:

$$lat_{1^o} = \pi R_E/180$$

$$lon_{1^o} = lat_{1^o} cos(lat_{mid}\, \pi/180)$$

where $R_E = 6371000$ m is the assumed radius of the Earth.

An alternative python script has also been written that interpolates the velocity data onto a regular lat-lon grid, as required by the wave model (again, the resolution is prescribed by the user). The extent of this grid will typically be smaller than the extent of the ATHAM-Fluidity domain since the regular lat-lon grid must fall entirely within the ATHAM-Fluidity domain, which is typically not aligned with the compass points.

### 2.4.3 Waves to ATHAM-Fluidity

The COARE 3.0 surface flux scheme (Fairall *et al*., 2003) has been implemented in ATHAM-Fluidity to calculate fluxes of momentum, temperature and moisture at the lower boundary. This algorithm includes an option to calculate a surface roughness over water that is dependent on wave spectrum parameters, namely the significant wave height and the dominant wave period. Both parameters are available from the wave model output, and so a two-way interaction between ATHAM-Fluidity and the wave model is possible. This coupling can be performed in an offline iterative manner, i.e. the 10 m wind fields from an ATHAM-Fluidity simulation without the wave-dependent surface roughness option is first supplied to the wave model, which is then run and the resulting wave parameters supplied to ATHAM-Fluidity, which is run again with the wave-dependent surface roughness option. This exchange can be repeated if necessary. The wave parameters are supplied to ATHAM-Fluidity via the model options (flml) file.

### 2.4.4 General ATHAM-Fluidity setup

This section describes model setup options common to both extreme events.

#### *2.4.4.1 Grid mesh*

The ATHAM-Fluidity model grid is defined such that the $x$ direction is aligned with the horizontal wind direction at the lowest grid point above the surface from the REMO vertical profiles. An R script has been created that converts topography fields from NASA's Shuttle Radar Topography Mission (SRTM) dataset, which has a resolution of 1 arc-second (approximately 30 metres), to a mesh geometry file appropriate for ATHAM-Fluidity. Specifically, ATHAM-Fluidity uses the open-source software GMSH to generate its 3D unstructured tetrahedral grid mesh from an appropriate GMSH geometry file. Again, it is intended to convert this R script to an equivalent python script so that it can be included with the open-source release of ATHAM-Fluidity to allow for use by general model users. The current script required the following as input:

- Path(s) to the downloaded STRM tile(s) that cover the region of interest to be meshed
- The latitude and longitude of the domain midpoint (decimal degrees)
- The domain extent in $x$ and $y$ and the domain height above sea-level (m)
- The angle through which the domain should be rotated (degrees; anticlockwise is positive)

- ❖ The mesh 'resolution' (more specifically, the mean tetrahedral edge length) at the surface midpoint of the domain (m)
- ❖ Optionally, the mesh 'resolution' (m) at the surface edges of the domain and a radius from the surface midpoint within which the surface mesh resolution is gradually stretched towards this value. (If not provided, the same mesh resolution is assumed everywhere at the surface)
- ❖ Optionally, the mesh 'resolution' (m) at the top of the domain. (If not provided, the same mesh resolution as at the at the surface edges of the domain is assumed)

The last two options allow the region of greatest interest (i.e. near the ground-level centre of the domain) to be well resolved whilst reducing computational costs by coarsening the mesh nearer the lateral and top domain boundaries. However, the standard GMSH algorithms assume that unstructured meshes are comprised of (quasi-)isotropic tetrahedra. Thus, the mesh resolution specified at a particular point in the domain is used to set the tetrahedral edge lengths in all three spatial dimensions. This is problematic for atmospheric-type large-eddy simulations, which typically employ anisotropic meshes with finer vertical than horizontal resolution to capture important sharp vertical gradients (particularly close to the surface) whilst allowing for domains with a large horizontal extent. This currently severely limits the amount of coarsening that can be performed and consequently produces meshes with an large number of elements for the horizontal extents that are hoped to be employed for the PEARL simulations (on the order of 100 km x 100 km). It is possible to generate structured isotropic meshes with GMSH, however this doesn't allow for the inclusion of a (smooth) topographical lower boundary or distinct land/sea surfaces. Work is therefore ongoing to find a solution that allows for the generation of unstructured anisotropic meshes. In the meantime, a structured grid with no topography or distinct land/sea surfaces is used. Nevertheless, a description of the R program that allows for the generation of unstructured isotropic meshes with surface topography and distinct land/sea surfaces is given below.

The program first defines a regular surface grid with a resolution equal to twice that of the coarsest surface resolution (i.e. the resolution at the surface edges if grid stretching is employed). This is done so that GMSH can later fit the individual elements of the actual surface mesh within this coarser grid. A local projection is used to convert from $x,y$ to latitude, longitude and vice-versa. Namely, it is assumed that 1° latitude is equal to $lat_{1^o} = \pi R_E/180$ metres, where the radius of the Earth is taken to be $R_E = 6371000$ metres, and 1° longitude is equal to $lon_{1^o} = lat_{1^o} cos(lat_{mid}\, \pi/180)$ metres, where $lat_{mid}$ is the latitude of the domain midpoint. **Figure** 2-12 shows an example surface grid centred on Greve, overlain on a contour plot of the original SRTM data. This grid has a horizontal extent of 70 x 70 km, is rotated anticlockwise through an angle of -20° so that the $x$ axis aligns with a fictitious surface wind direction of 290. 7°, and has a resolution of 1000 m (twice that of the surface mesh resolution at the edge of the domain, which was set to 500 m; note that this is vertically far too coarse to be used in the actual PEARL simulations).

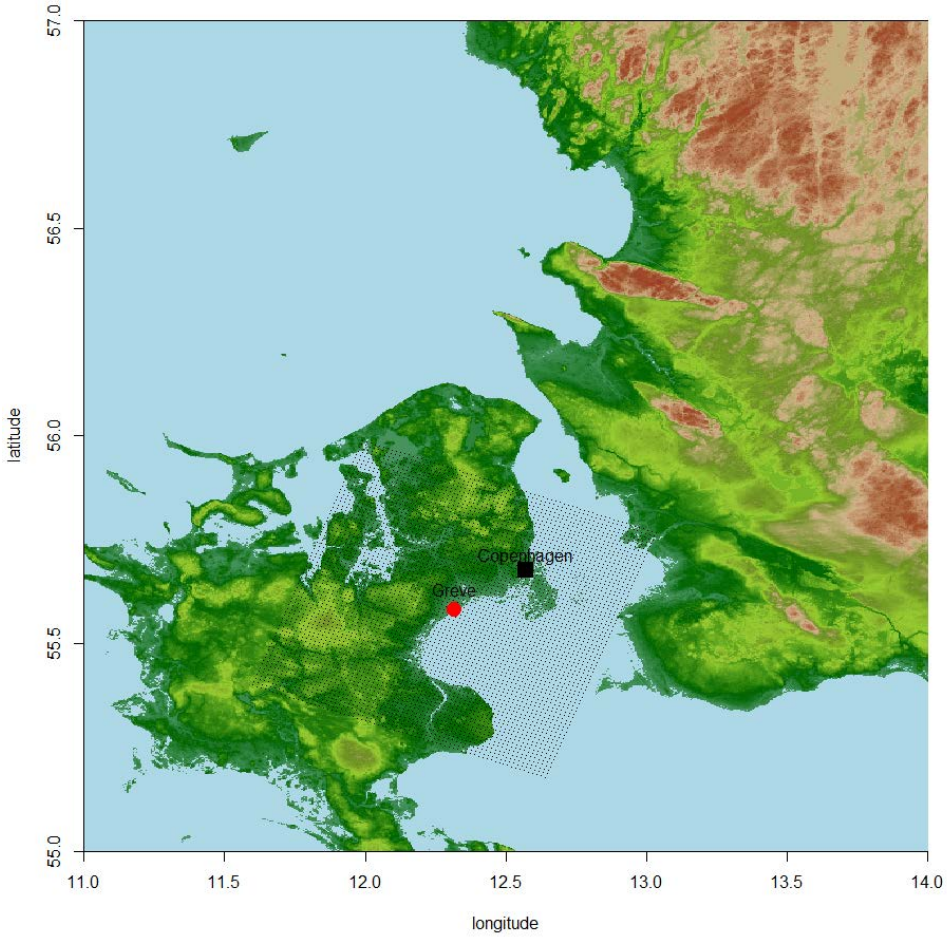


***Figure** 2-12 - Vertices of the regular surface grid used to generate an example mesh centred on Greve, overlain on a contour plot of the original SRTM data.*

The SRTM data is then spatially filtered using a conservative 2D top-hat filter kernel with a filter width equal to the resolution of the surface mesh. This is done so that the topography data varies on the same spatial scale as surface grid resolution, allowing the heights at each grid vertex to then be simply interpolated from the grid of SRTM heights using a nearest-neighbour approach. This naturally smoothes out the surface topography (thus reducing the maximum height), but maintains the same integral height across the filtered region. **Figure** 2-13 shows the effect of filtering the SRTM data for the example grid discussed above. Note that a slightly larger region of SRTM data (outer rectangle in the top panel) is needed to filter the region enclosing the surface grid (inner rectangle) due to the finite extend of the filter kernel.

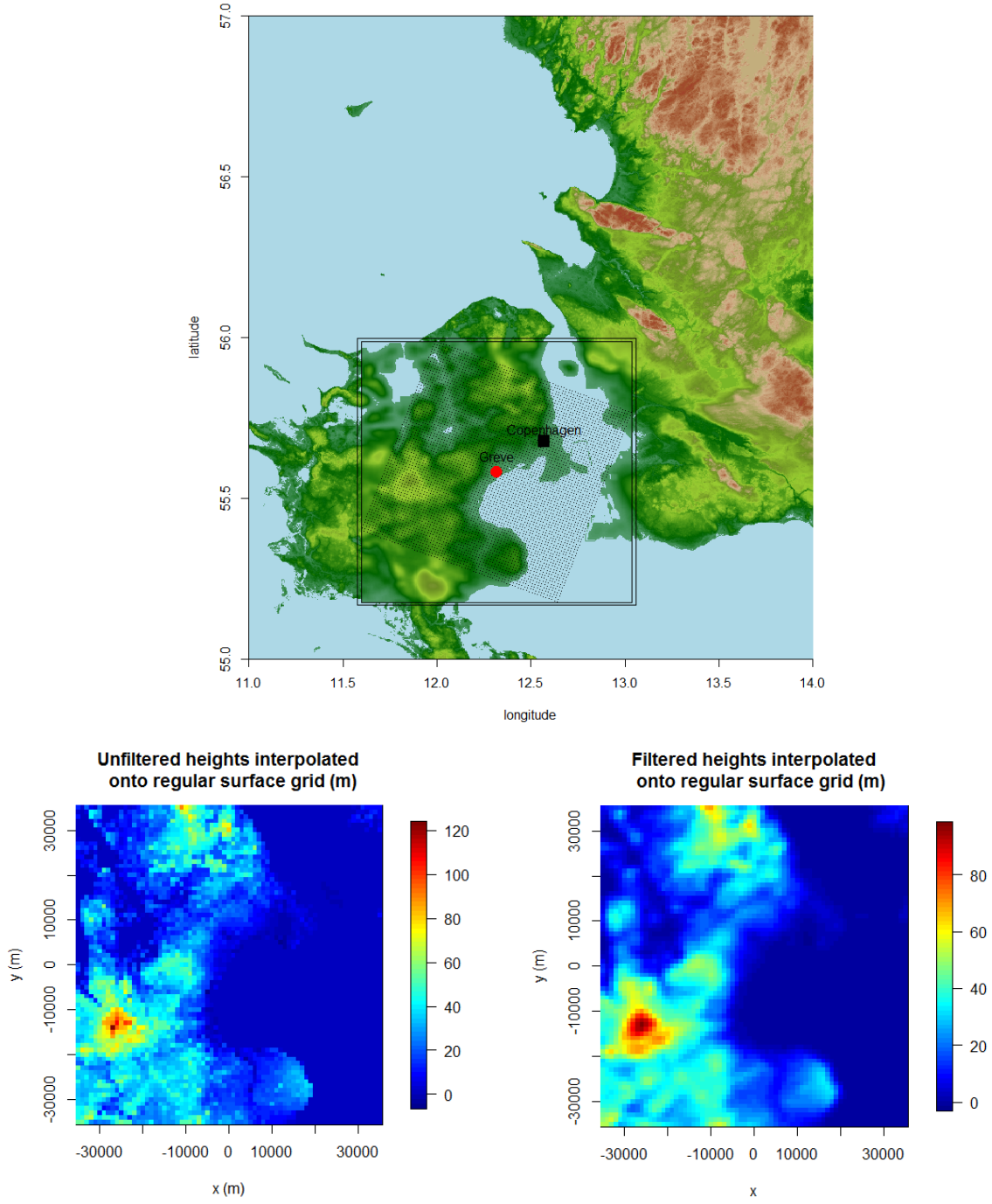


***Figure** 2-**13** – Top: Filtered SRTM data with the regular surface grid overlain. Bottom Left: Unfiltered SRTM data interpolated onto the regular surface grid (height variation does not match the grid resolution). Bottom Right: Filtered SRTM data interpolated onto the regular surface grid (height variation does match the grid resolution).*

Once the heights have been interpolated onto the surface grid, a wireframe surface is created by dividing each square of four surface heights into two triangles. In this way, the entire surface can be recreated using smaller plane surface elements, thus avoiding any curved elements which are not compatible with a tetrahedral finite element mesh. There are two ways that each square can be divided into two plane triangular surfaces (see **Figure** 2-14). The option shown on the left of this figure is arbitrarily chosen in all cases, apart from those rare situations in which coastal alignment is better represented using the option on the right.

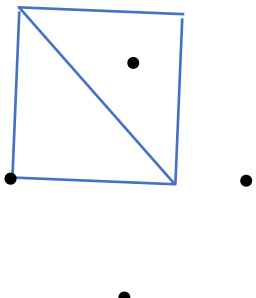

***Figure** 2-**14** - Method for dividing each grid square into two plane triangular surfaces. Left: default option. Right: Option used in rare cases to give better representation of coastal alignment.*

Finally, the mesh geometry file is written out in the appropriate GMSH format. The wireframe surface is divided into two 'physical surfaces'; one for water regions and the other for land regions. This will allow for different surface boundary conditions to be applied to each physical surface separately in ATHAM-Fluidity (see Figure 2-15).

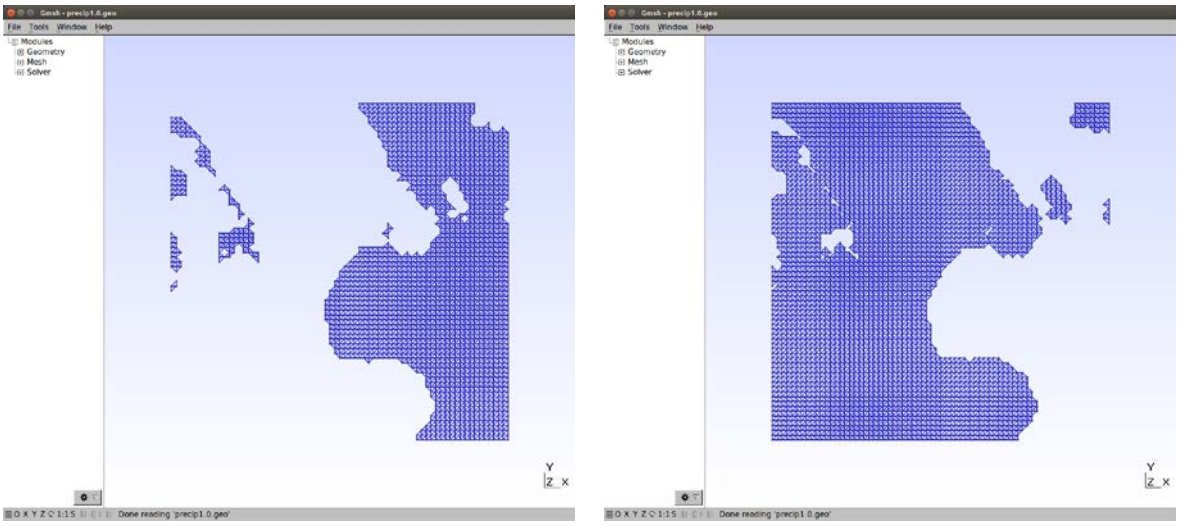

***Figure** 2-**15** - The separate physical surfaces for water (left) and land (right) as viewed in GMSH.*

Figure 2-16 shows all the physical surfaces in the GMSH geometry file (including the domain sides and lid), at an angle that allows the surface topography to be visualised. Note that even the largest topographical features around Greve are very low relative to the LES domain heights that will be employed for the PEARL simulations (on the order of 10 km) and so all the heights have been scaled by 50 in the plot for the benefit of viewing.

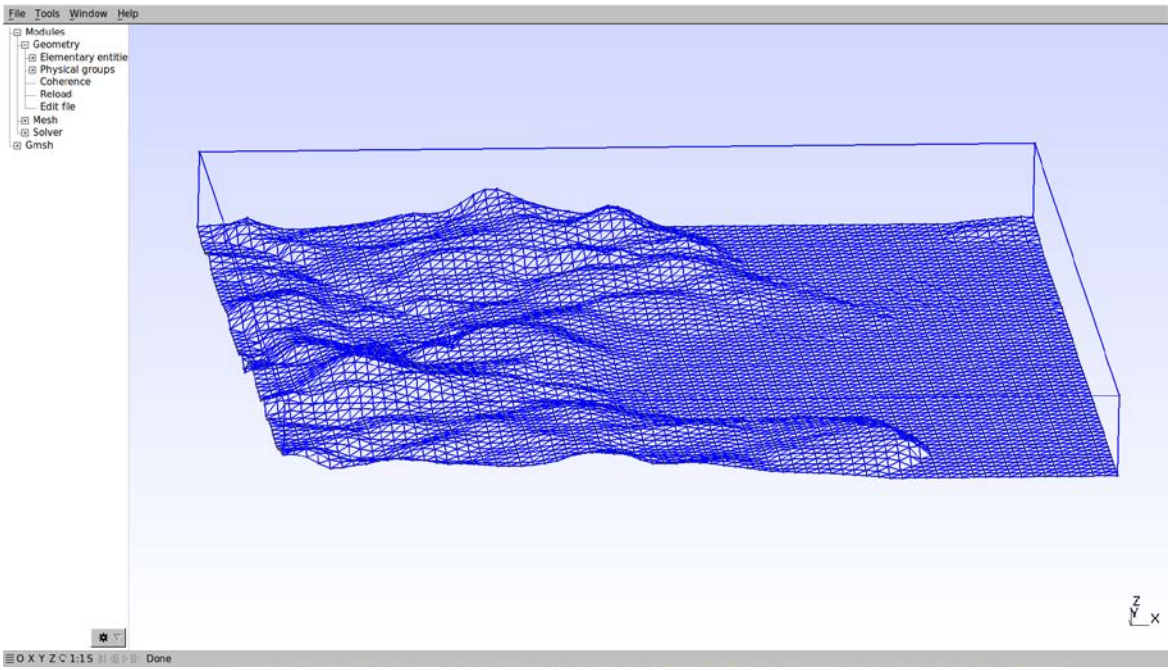


***Figure** 2-**16** - All physical surfaces of the GMSH geometry file (surface heights scaled by 50 times for the benefit of viewing topography)*

Each vertex of the wireframe surface (and the four vertices defining the top of the domain) also has an associated resolution written to the GMSH geometry file. These values are based on the resolutions given by the user in the R script. For example, Figure 2-17 shows parts of the actual 2D mesh created by GMSH for the following options, which are only example values and are not appropriate for the actual PEARL simulations:

- 100 m surface resolution at the domain centre (Greve)
- 500 m surface resolution at the domain edges
- 10 km radius within which the surface resolution at the centre is gradually stretched towards the resolution at the edges
- 1000 m resolution at the top of the domain

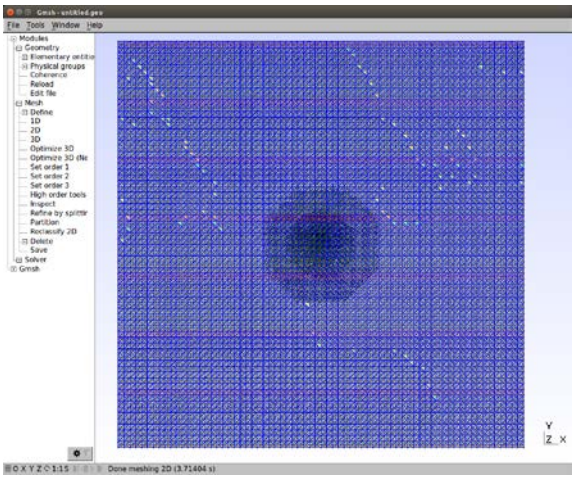

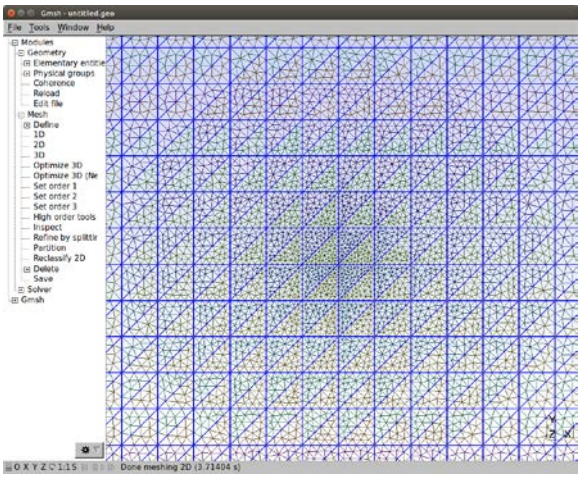

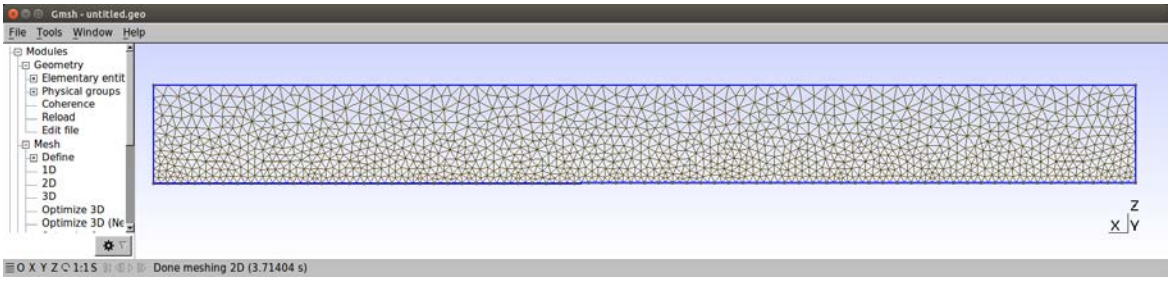


***Figure 2-17*** *– Actual 2D mesh created by GMSH from the geometry file. Top panel: Entire surface mesh (left); zoomed in surface mesh near the centre of the domain showing radial element stretching (right). Bottom: 2D mesh on one of the sides of the domain, showing vertical element stretching.*

### *2.4.4.2 Inlet turbulence generator*

As detailed in Section 2.4.1, ATHAM-Fluidity is driven by vertical profiles extracted from the REMO model simulation. These profiles vary on the time-scales associated with the REMO simulations, i.e. 3-hourly. Averaging the wind field over these time-scales removes all the turbulence length-scales, thus leaving only the 'mean' wind component which contains no vertical motions. Conversely, ATHAM-Fluidity runs at spatial and temporal resolutions that are able to explicitly resolve much of the turbulence spectrum. In order to exploit this capability, it is therefore necessary to 'generate' turbulence from the mean wind profiles. This is typically achieved in one of two ways in LES modelling studies:

- ***Periodic boundary conditions***: Turbulence will start to develop naturally within the LES domain if the mean flow is perturbed (for example, by uneven surface elements). Although this turbulence takes a while to 'spin up', employing periodic boundary conditions ensures that the generated turbulence is recycled back to the inlet once it has left the downwind edge of the domain. However, periodic boundary conditions are not always appropriate if, for example, there are differences in surface-type between the upwind and downwind regions of the domain. In this case, the turbulence recycling plane can alternatively be positioned part-way down the domain, with an open boundary condition employed at the far downwind edge. This method has been shown to work well in previous LES studies, e.g. Maronga *et al*. (2015). However, there is a substantial computational cost associated with the requirement for a larger upwind domain fetch (as well as the associated spin-up time).
- ***Inlet turbulence generator***: To overcome the additional computational costs associated with turbulence recycling methods, another method has also been proposed in the LES literature in which artificial turbulence is generated at the inlet and superimposed on top of the mean velocity profiles (e.g., Xie and Castro, 2008). Although this method is more efficient, care must be taken to ensure that the artificial turbulence statistics accurately reproduce the statistics that would be observed if the turbulence developed naturally.

For PEARL, the second option has been employed, namely the synthetic-eddy method which was developed by Pavlidis *et al*. (2010) for the Fluidity model but also available in ATHAM-Fluidity. This method is able to reproduce prescribed statistics up to second-order, prescribed turbulence length-scales, and the expected -5/3 power law scaling in the turbulence spectrum. The method requires the following inputs for each velocity component in $x, y, z$:

- *Mean wind profile*: i.e. the vertical profiles from the REMO model in our case.
- *Number of eddies*: The more turbulence 'spots' that are superimposed on top of the mean wind profile at the inlet, the closer the prescribed statistics will be achieved. A value of 1000 for each component has been found to give adequate results whilst keeping computational costs down.

- ***Reynolds stresses**:* Only the vertical components of the Reynolds stresses are prescribed, i.e. $u_i' u_i'$ where $i = 1{,}2 \vee 3$. The other components (shear stresses) are assumed zero but dynamically recover their true value very close to the inlet (Pavlidis *et al.*, 2010).
- ***Turbulence length-scale**:* This typically takes the form of a vertically varying profile, used to account for the fact that the integral length-scale varies with altitude and stability.

For the current PEARL simulations, Reynolds stress and turbulence length-scale profiles based on numerical simulations performed by Aspley and Castro (1997) of a perfectly neutral atmosphere (using a $k - \varepsilon$ model) have been employed. Neutral stability is associated with overcast and windy conditions and so this assumption is well founded.

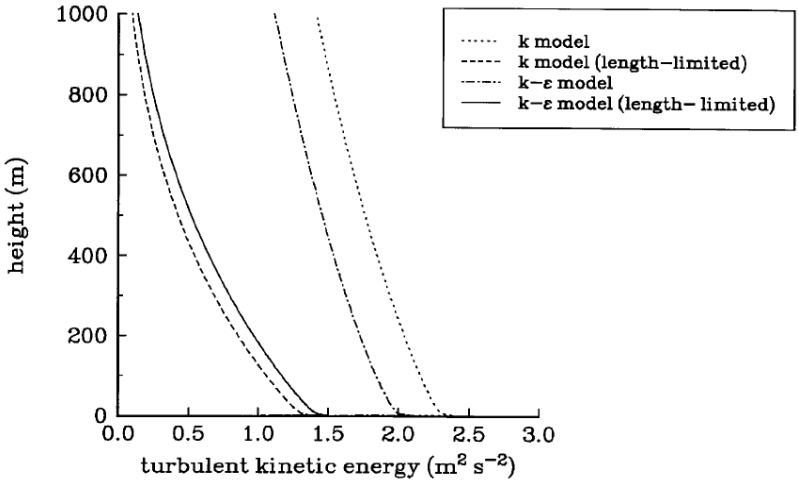


*Figure 3.* Simulation of Leipzig data – turbulent kinetic energy profile.

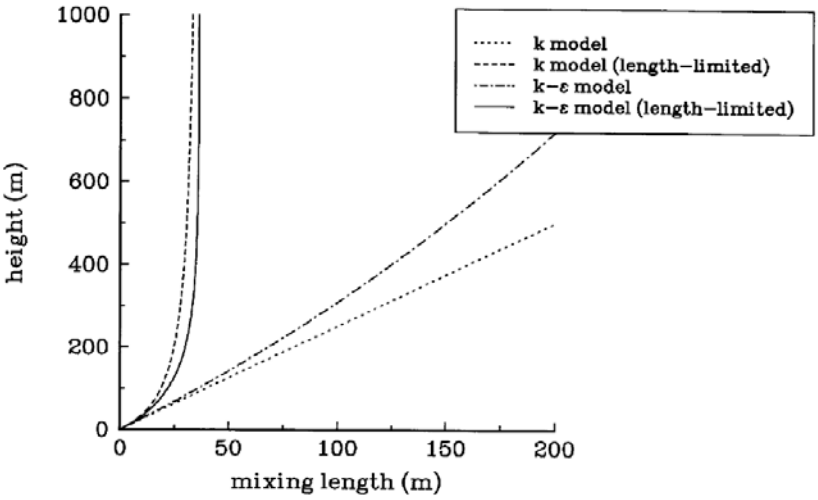


*Figure 4.* Simulation of Leipzig data – mixing length profile.

***Figure** 2-**18** - Figures 3 and 4 from Aspley and Castro (1997), used to prescribe the Reynolds stresses and turbulence length-scales in the synthetic-eddy method*

The relevant figures from this paper are shown in **Figure** 2-18. The top panel shows the profiles of turbulent kinetic energy (TKE) up to 1000 m. The following function closely matches the $k - \varepsilon$ model profile, and is also used to extrapolate the values of TKE above 1000 m:

$$TKE_{AC96} = 2e^{-z/1666}$$

where $z$ is altitude (m). It is further assumed that all neutral TKE profiles are self-similar when nondimensionalised by the square of the geostrophic wind speed $U_g$ (equal to 17.5 m/s in Aspley and Castro's simulations, and taken to be the maximum wind speed from the REMO profiles in the current simulation), i.e.:

$$TKE = \frac{2U_g^2 e^{-z/1666}}{17.5^2}$$

Finally, isotropic turbulence is assumed. Since $TKE = \frac{1}{2}\left(u_1'u_1' + u_2'u_2' + u_3'u_3'\right)$, it follows that the individual components of the diagonal Reynolds stresses used for input into the synthetic-eddy method are equal to:

$$u_i'u_i' = \frac{2}{3}TKE = \frac{4U_g^2 e^{-z/1666}}{3 \times 17.5^2} for i = 1,2 \vee 3$$

The bottom panel of **Figure** 2-2-19 shows the profiles of mixing length, $L_m$, up to 1000 m. Again, the following function closely matches the $k - \varepsilon$ model profile, and is used to extrapolate the values of mixing length above 1000 m:

$$L_m = 1.25z^{0.77}$$

Since isotropic turbulence is assumed, this function is used to set all three components of the turbulence length-scale for input into the synthetic eddy method.

#### *2.4.4.3 Velocity absorption layer*

It has been found necessary to include a velocity absorption layer close to the outflow boundary of the ATHAM-Fluidity modelling domain in order to avoid spurious flow behaviour that has been observed to emanate from the outlet when no sponge layer is employed. An algorithm has been implemented that allows the user to specify (a) a velocity profile at the outflow boundary, (b) a distance over which the flow in the domain interior is nudged towards that profile, and (c) a coefficient that defines the magnitude of this nudging (a value of zero implies no nudging, while a value of 1 ensures that the flow exactly equals the prescribed outflow profile at the outlet). Empirical testing has shown that prescribing an outlet velocity profile equal to that prescribed at the inlet boundary (with a coefficient of 1) and a nudging distance equal to 10% of the streamwise domain length produces stable simulations.

#### *2.4.4.4 Cloud microphysics*

A two-moment cloud microphysics scheme based on Seifert and Beheng (2006) has been implemented in ATHAM-Fluidity in order to capture cloud and precipitation formation within a simulation. This scheme treats both, number and mass concentrations of each hydrometeor type prognostically. Currently only warm-phase processes have been included. Water is therefore assumed to be in one of three states: water vapour, liquid cloud droplets (taken to be drops with radii smaller than 40 µm) or raindrops (drops with radii larger than 40 µm). The following conversion processes are explicitly accounted for:

- Water vapour → cloud droplets (nucleation)
- Cloud droplets → cloud droplets (selfcollection)
- Cloud droplets → raindrops (autoconversion, accretion)
- Raindrops → raindrops (selfcollection, collisional breakup, evaporation)
- Cloud/raindrop removal (sedimentation)

#### 2.4.4.5 *Surface fluxes*

The COARE 3.0 surface flux scheme (Fairall *et al*., 2003) has been implemented in ATHAM-Fluidity to calculate fluxes of momentum, temperature and moisture at the lower boundary. However, this scheme has not yet been fully tested and so ATHAM-Fluidity is currently run without a surface flux scheme. Surface fluxes of temperature can provide a source of convective instability, leading to the generation of convectively driven clouds and precipitation within the modelling domain, and is therefore of importance in the context of PEARL in the long term. However, the generation of clouds within the ATHAM-Fluidity domain will still occur without a surface flux scheme: stratified clouds within initially saturated layers of the atmosphere should be accurately captured by the model, and convective clouds will be formed in cases where a convectively unstable atmospheric profile is advected into the domain and the inlet turbulence generator provides the vertical perturbations required to release this convective instability.

#### 2.4.4.6 *Subgrid-scale model*

A Smagorinsky-type subgrid-scale model (Smagorinsky, 1963) has been implemented in ATHAM-Fluidity to account for the dissipative effects of the unresolved turbulent motions on the flow-field. Like the surface flux scheme, however, this subgrid-scale model has not been fully tested, and so ATHAM-Fluidity is currently run without a subgrid-scale model. ATHAM-Fluidity has been shown to remain both stable and accurate in the absence of an eddy viscosity term, relying simply on numerical diffusion to dissipate energy at the smallest resolved scales. For example, the idealised and benchmark tests presented in Savre *et al*. (2016) were all performed without any subgrid-scale model or additional viscosity term.

#### 2.4.4.7 *Other settings*

ATHAM-Fluidity is set up to solve the fully compressible non-hydrostatic set of governing equations, using a $P1_{DG}$-P2 finite element discretisation that has been shown to be well suited to atmospheric flows (Cotter and Shipton, 2012). With this discretisation, the pressure and density fields are solved using second-order (i.e. quadratic) continuous element functions, whereas the velocity and remaining scalar fields are solved using first-order (i.e. linear) discontinuous element functions. An adaptive timestep is employed that ensures a maximum Courant-Friedrichs-Lewy (CFL) number of less than 0.5 everywhere within the domain. Empirical testing has shown this to be close to the upper limit of the CFL number before the pressure and/or velocity solvers fail to converge below a reasonable tolerance after a large number of iterations.

## 2.5 Extreme Event I (Precipitation)

### 2.5.1 Specific ATHAM-Fluidity setup

#### 2.5.1.1 *Grid Mesh*

The model domain has a horizontal extent of 100 km x 100 km and a vertical extent of 12 km, which the REMO profiles show to be around 2 km above the tropopause. The associated stratospheric temperature inversion in this upper 2 km provides a 'natural sponge layer' at the top of the domain, which should act to realistically absorb or reflect any vertically propagating atmospheric waves rather than artificially reflecting them upper model boundary. A structured anisotropic grid mesh with a flat lower boundary is specified due to the ongoing issues with generating an unstructured anisotropic mesh that includes topography and distinct land-sea surfaces (see Section 2.4.4.1 for details). The employed grid has a horizontal 'resolution' (i.e. tetrahedral edge length) of 200 m in both $x$ and $y$ (thus there are 500 tetrahedral 'columns' in each of these dimensions), and a vertical resolution of 30 m within the first 1000 m above the ground, above which the resolution is stretched smoothly such that there are 100 vertical layers overall. This results in a stretch factor of 1.043 and a vertical

resolution of around 480 m at the top of the domain. Figure 2-19 shows the vertical structure of this structured isotropic grid.

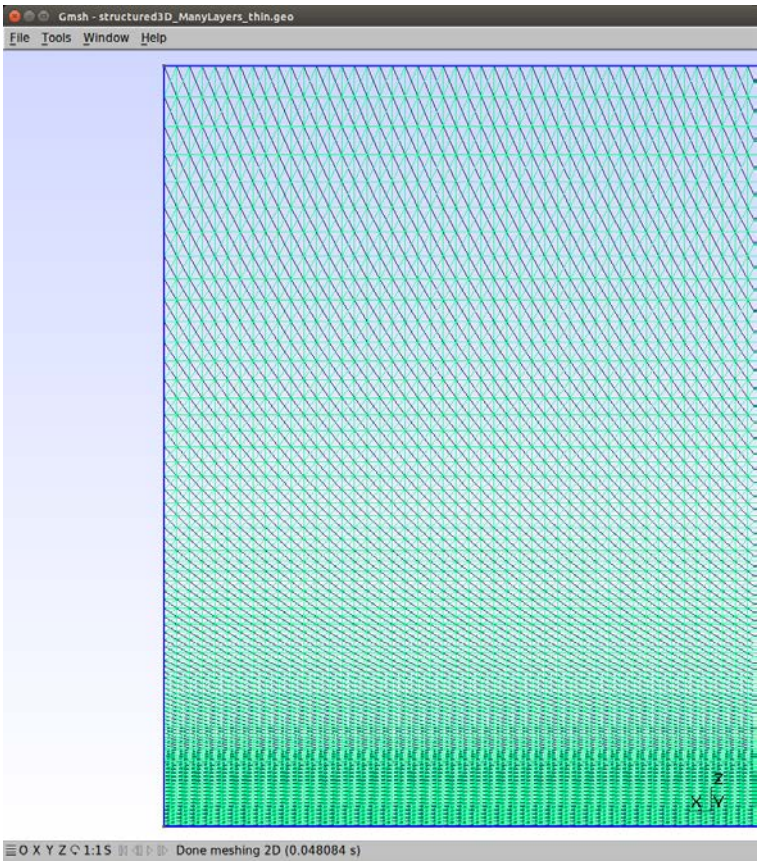


***Figure** 2-19 – Vertical structure of structured anisotropic grid*

Each cuboid of the grid mesh contains six tetrahedra, and so this grid mesh contains 500 x 500 x 100 x 6 = 150 million tetrahedral elements. The computational memory requirements for storing the prognostic and diagnostic fields that are solved by ATHAM-Fluidity on this grid far exceed the resource limits of an individual processing unit and so the grid mesh must be decomposed into a number of smaller partitions in preparation for running the model in parallel on a larger number of processes. This grid decomposition carried out using the 'fldecomp' executable, which is compiled with the ATHAM-Fluidity source.

The domain is oriented such that the streamwise dimension ($x$) is aligned with the near-surface wind direction from the REMO profiles used for the initial and boundary conditions, which in this case is 278°.

### *2.5.1.2 Initial and boundary conditions*

The initial and inlet boundary conditions for pressure, potential temperature, velocity and moisture are based on vertical profile data extracted from the REMO model simulation over Greve, as detailed in Section 2.4.1. The profiles from the REMO output time 1966-08-18 09:00:00 have been used to initialise the model. This is the output time for which REMO predicts the heaviest precipitation rates (5.8 mm/hr). In addition, a no-slip boundary condition is applied at the surface, and a free-slip (no-normal-flow) boundary condition is applied at the side and top boundaries of the domain.

### *2.5.1.3 Inlet turbulence generator*

The profiles for the turbulence length-scale and Reynolds stress components, required as inputs to the 'synthetic-eddy method' inlet turbulence generator, are based on numerical simulations

performed by Aspley and Castro (1997) (see Section 2.4.4.2 for details) with the geostrophic wind speed $U_g$ taken to be the maximum wind speed from the REMO velocity profiles, which in this case is $U_g = 23.8$ m s$^{-1}$.

#### *2.5.1.4 Other settings*

Other model settings are as described in Section 2.4.4 (General ATHAM-Fluidity setup).

### 2.5.2 CPU resources

A very large number of parallel computing cores are required in order to run the above simulation setup so that (a) any one individual core does not run into memory limit issues, and (b) the wall-clock time required to complete a meaningful simulation time period is not too large. An application for resources on the Tianhe-2/MilkyWay-2 supercomputer in China (the second largest supercomputer in the world) has been made for this reason. Unfortunately, however, no response to this application has yet been received after many months of waiting. Access to the University of Cambridge's 'Darwin' HPC facility has been granted, on which it is possible to run on up to 256 cores simultaneously for up to 12 wall-clock hours at a time. However, technical difficulties in getting the model to run on this machine exist due to the fact that ATHAM-Fluidity was compiled using the Intel Fortran/C compilers, which are not supported by the Fluidity development team due to known issues with this compiler set. Until these issues are fixed or access is granted on another HPC facility, it is therefore necessary to make do with the computational resources currently available. ATHAM-Fluidity has been successfully installed (using the supported GNU compiler collection) on a relatively small server that contains 28 cores. Unfortunately, this is not enough cores to run the above simulation without running into memory issues. The following two additional simulations have therefore been set up in order to make use of this 28-core machine:

- ***Shallow model domain***: The above simulation is able to run on 28 cores if the height of the modelling domain is dramatically reduced to include just a few vertical layers (whilst keeping the horizontal extent of the domain fixed at 100 km x 100 km). Although the resulting surface precipitation fields will not contain useful data, these output fields will at least cover the appropriate horizontal extent and have the correct (vtu) file format. These data files can therefore be passed to the flood modellers at ICL to test whether they can drive the flood model with these input data files as 'proof of concept' of the integrated modelling framework. With some post-processing, the values in these output vtu files can also be modified towards the REMO-predicted precipitation rates so that the flood modeller can drive their model with more sensible data.
- ***Narrow model domain***: The above simulation is also able to run on 28 cores if the horizontal extent of the domain is dramatically reduced, whilst the vertical extent and grid structure are kept unchanged. For example, by reducing the streamwise ($x$) domain length from 100 km to 10 km, and the spanwise ($y$) domain length from 100 km to just 1 km (i.e. a 'channel flow' type setup), the model is able to run one hour of simulation time in around 10 wall-clock hours. This simulation will produce far more realistic output data than the 'shallow model domain' case due to the full representation of the vertical atmospheric state throughout the troposphere, albeit within a much smaller horizontal domain, and is therefore useful to analyse model performance.

### 2.5.3 Results: Shallow model domain

The 'shallow model domain' simulation was run for just one timestep in order to produce a vtu file containing surface precipitation data. A python script was then run to modify the values in this vtu file so that the precipitation rate at each surface node was equal the precipitation rate as predicted by

REMO (5.8 mm/hr) plus a random perturbation (taken from the normal distribution with a mean of zero and standard deviation of 0.5). The resulting vtu surface precipitation field is shown in **Figure** 2-20, as visualised in ParaView. The python script also adds two new fields to the vtu file that store the latitude and longitude of each node, so that the flood modellers can locate the output grid geographically. This precipitation data has been made available to drive the flood model for Greve.

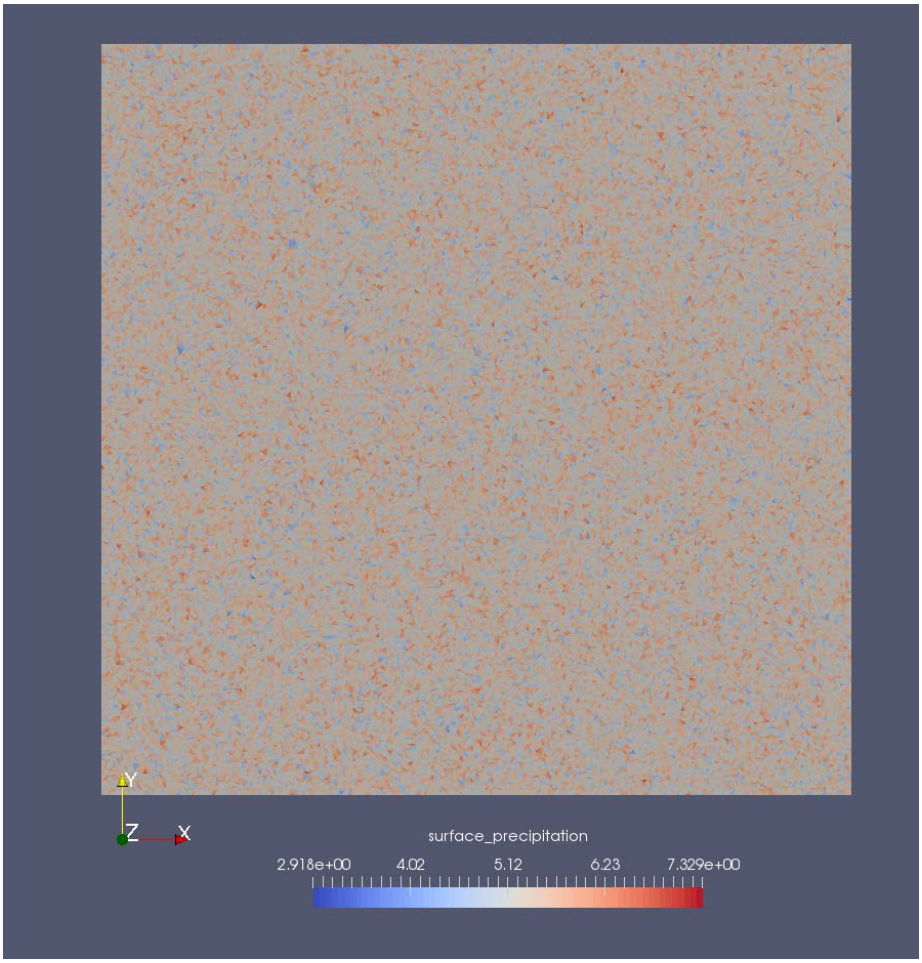


***Figure** 2-**20** – 'REMO + white noise' surface precipitation field in vtu format (visualised in ParaView)*

### 2.5.4 Results: Narrow model domain

The 'narrow model domain' simulation was run for one hour simulation time. Figure 2-21 shows x-z contour slices of the velocity field at both t = 0 hrs (i.e. the initial field) and at t = 1 hr. The snapshots at t = 1 hr verify that, below around 10km, the inlet turbulence generator advects turbulence into the domain with the eddy size increasing with altitude and TKE decreasing with altitude. There appears to be a slight issue at the top of the modelling domain, where smaller energetic are again present. This is a fairly common occurrence in LES, where wave reflections at the domain top can degrade the flow-field in the absence of a strong enough damping layer.

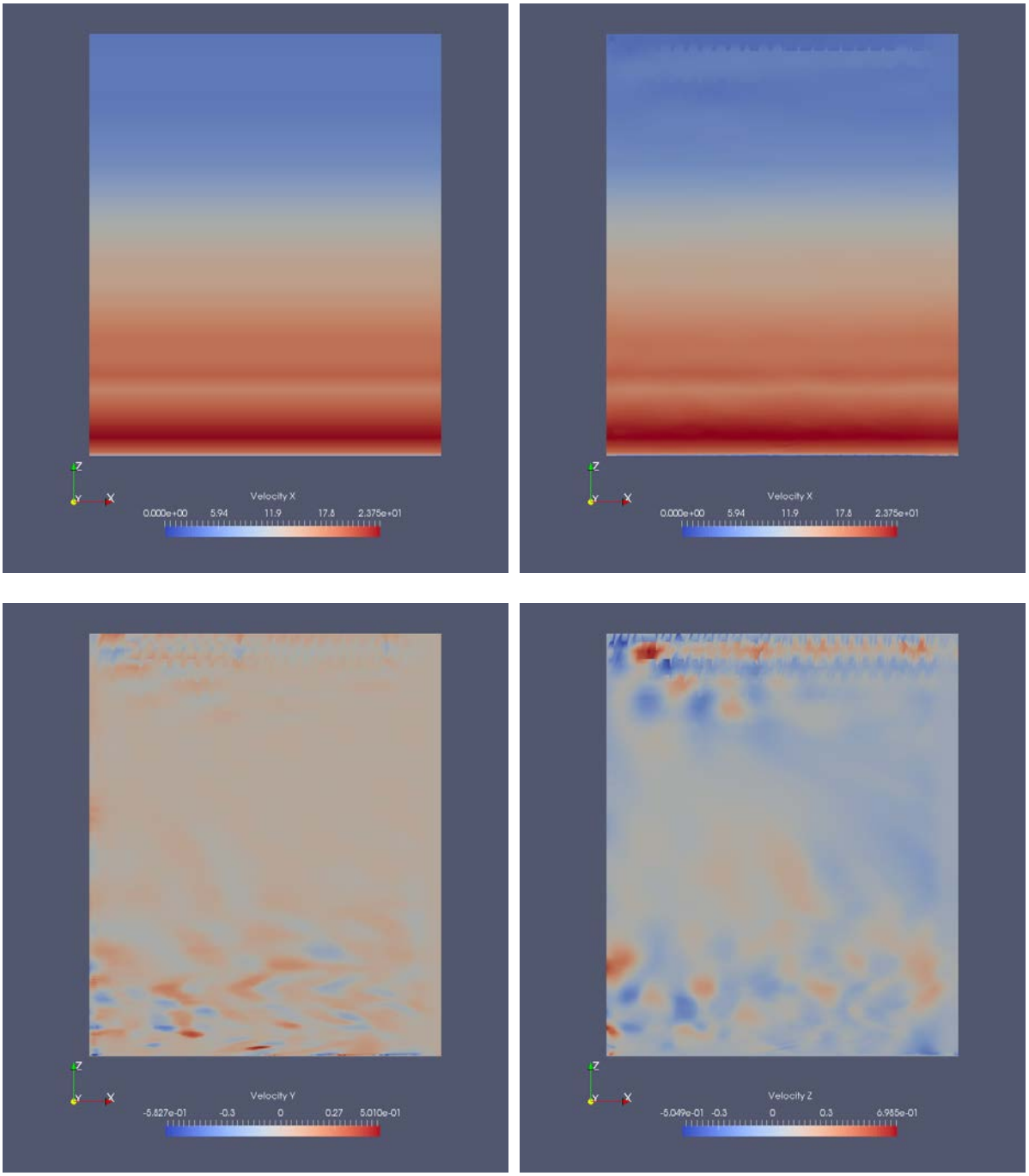


***Figure** 2-21– x-z contour slices of the velocity field. Top left: x-component of velocity at t = 0 hrs. Top right: x-component of velocity at t = 1 hr. Bottom left: y-component of velocity at t =1 hr. Bottom right: z-component of velocity at t = 1 hr.*

**Figure** 2-22 shows x-z contour slices of the cloud droplet mass concentration field at both t = 0 hrs and t = 1 hr. A stratified layer of cloud in the initial REMO soundings is observed at around 2-3km. At t = 1 hr, it appears that the vertical perturbations provided by the inlet turbulence generator have also instigated the formation of convective clouds, however the modelling domain is too short to observe the full growth of these clouds before they are advected past the outlet boundary. With more computational resources, the full 100 km spanwise grid could be adopted and the precipitation from these convective clouds would have time to reach the surface.

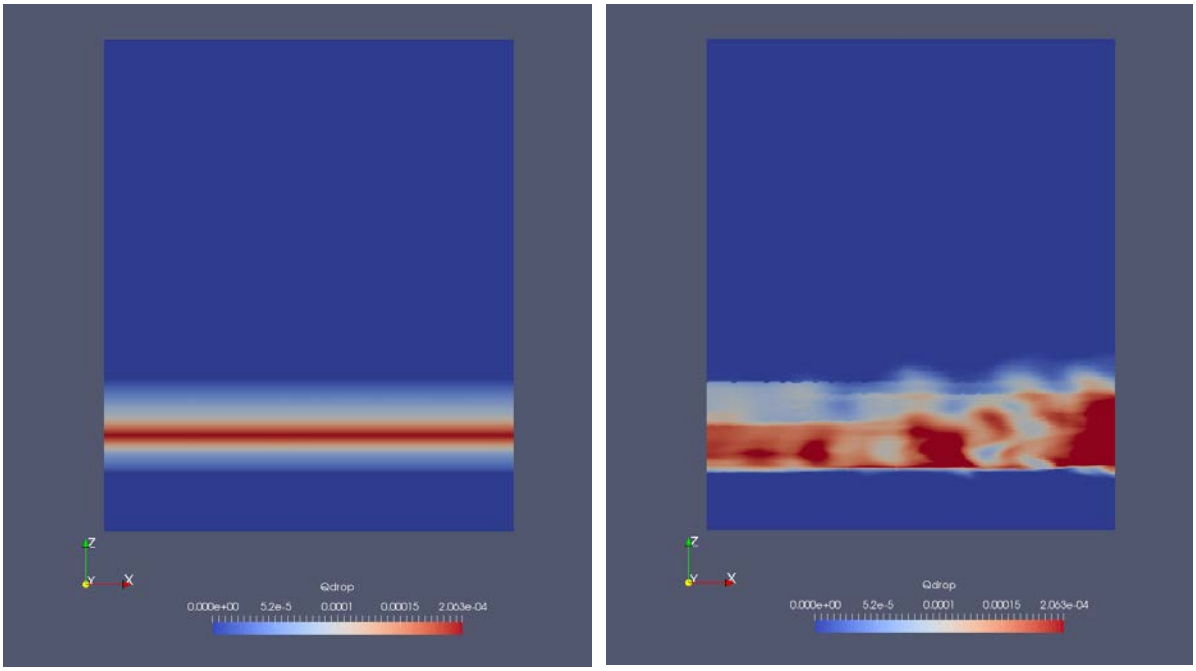


***Figure** 2-**22** - x-z contour slices of the cloud droplet mass concentration at t = 0 hr (left panel) and t = 1 hr (right panel)*

**Figure** 2-23 shows an example of the precipitation that can occur from convectively driven clouds when the modelling domain has a large enough horizontal extent (note that this simulation uses idealised inlet profiles rather than ones taken from REMO). In this case, convection has also been strengthened by the prescription of a heated surface temperature boundary condition in the last ¾ of the modelling domain, which results in the generation of thermals that carry moist air past the lifting condensation level.

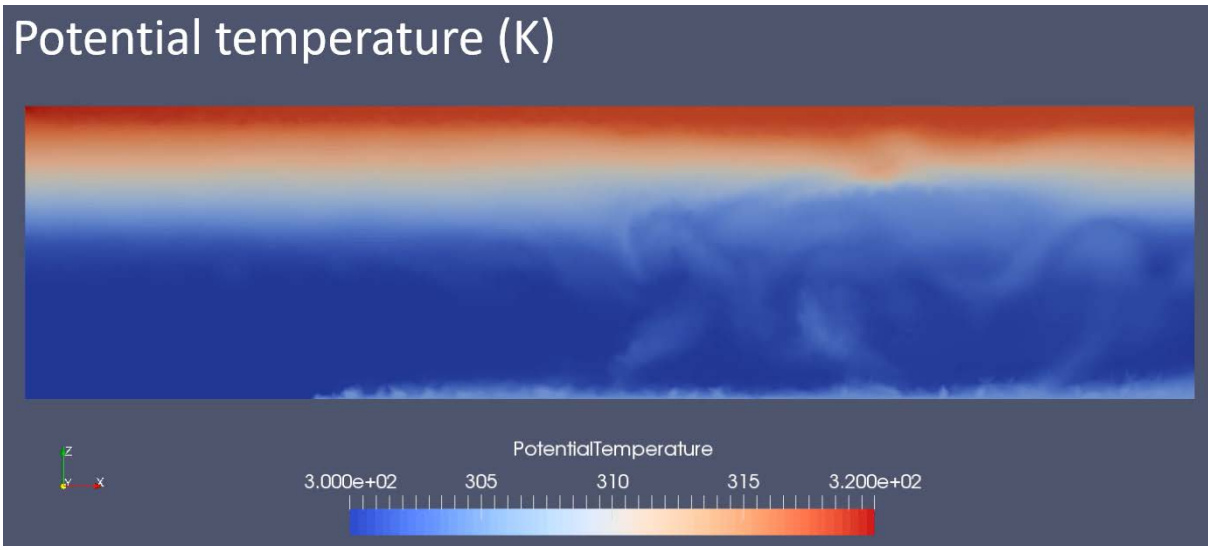

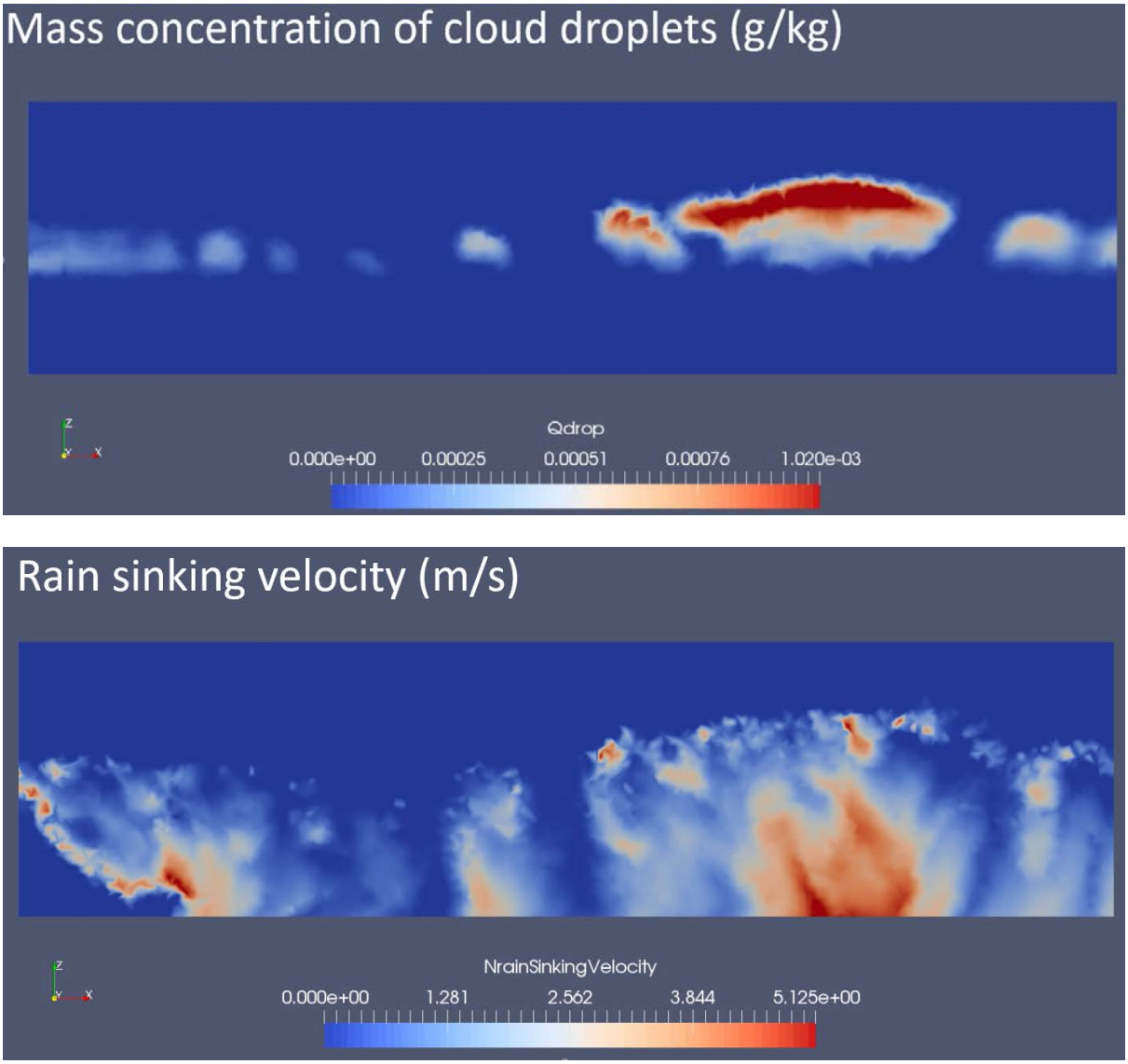


***Figure** 2-**23** – instantaneous x-z slices through a simulation at a time when significant convective rain is occurring. Top panel: Potential temperature. Middle panel: cloud droplet mass concentration. Bottom panel: Rain sinking velocity.*

Attempts are currently being made to run the narrow model domain simulation (i.e. forced by the real REMO profiles) on a grid with the full streamwise extent (100 km) in order to better capture the growth of the convective clouds and resulting surface precipitation rates within the modelling domain.

## 2.6 Extreme Event II (Sea-level)

### 2.6.1 Specific ATHAM-Fluidity setup

#### *2.6.1.1 Grid Mesh*

The same grid mesh as used for the precipitation extreme event will be employed for the sea-level extreme, i.e. a model domain with a horizontal extent of 100 km x 100 km and a vertical extent of 12 km, a structured anisotropic grid mesh with a flat lower boundary, a horizontal resolution of 200 m in both $x$ and $y$, and a vertical resolution of 30 m within the first 1000 m and a smoothly stretched resolution above this with 100 vertical layers overall. The domain is oriented such that the streamwise dimension ($x$) is aligned with the near-surface wind direction from the REMO profiles used for the initial and boundary conditions, which in this case is 291°.

#### 2.6.1.2 Initial and boundary conditions

The initial and inlet boundary conditions for pressure, potential temperature, velocity and moisture are extracted from the REMO model output time 2000-02-04 18:00:00 and have been used to initialise the model. This is half a day before the sea-level extreme at Greve occurred in the REMO model simulation (at 2000-02-05 06:00:00). To simulate the entire 5-day period centred on the day of the extreme (as done by REMO) is computationally unfeasible with ATHAM-Fluidity, and so we initially aim to simulate 12 hours either side of the time of the sea-level extreme. In addition, a no-slip boundary condition is applied at the surface, and a free-slip (no-normal-flow) boundary condition is applied at the side and top boundaries of the domain.

#### 2.6.1.3 Inlet turbulence generator

The profiles for the turbulence length-scale and Reynolds stress components for the synthetic-eddy method are again based on the Aspley and Castro (1997) simulations (see Section 2.4.4.2 for details) with the geostrophic wind speed $U_g$ taken to be the maximum wind speed from the REMO velocity profiles, which in this case is $U_g = 64$ m s$^{-1}$.

#### 2.6.1.4 Other settings

Other model settings are as described in Section 2.4.4 (General ATHAM-Fluidity setup).

### 2.6.2 CPU resources

As with the precipitation extreme event, it is not currently possible to run the above simulation with the computational resources available. An additional '***shallow model domain***' simulation has therefore been set up in order to make use of the available 28-core machine. This simulation uses a model grid with the same horizontal extent (100 km x 100 km) as the full simulation but a greatly reduced vertical extent. Again, the resulting 10 m wind fields from the ATHAM-Fluidity run, as required by the wave model, will not contain particularly useful data but will at least cover the appropriate horizontal extent. This simulation can therefore be tested whether the 10 m wind fields can be converted to netCDF format to see if these fields can drive the wave model SWAN.

### 2.6.3 Results: Shallow model domain

The 'shallow model domain' simulation was run for just one timestep in order to produce a vtu file containing the ATHAM-Fluidity velocity field. The python script described in Section 2.4.2 was then run to extract the 10 m wind velocity components onto a regular grid and write the values to a netCDF file along with the longitude and latitude information. In addition, a random number generator was used to add some white noise on top of the 10 m wind field before being written to the netCDF file. Without this step, all the values in would be essentially equal to the initial condition, i.e. the REMO 10 m wind speed, due to the very short simulation time. **Figure** 2-24 shows the resulting netCDF file as visualised with the Panoply software. The upper panel shows the shows the East-West component of the 10 m wind field on a regular cartesian grid that is oriented with the ATHAM-Fluidity domain. The lower panel shows the same field on a regular latitude-longitude grid. This data has been made available to drive the SAN model.

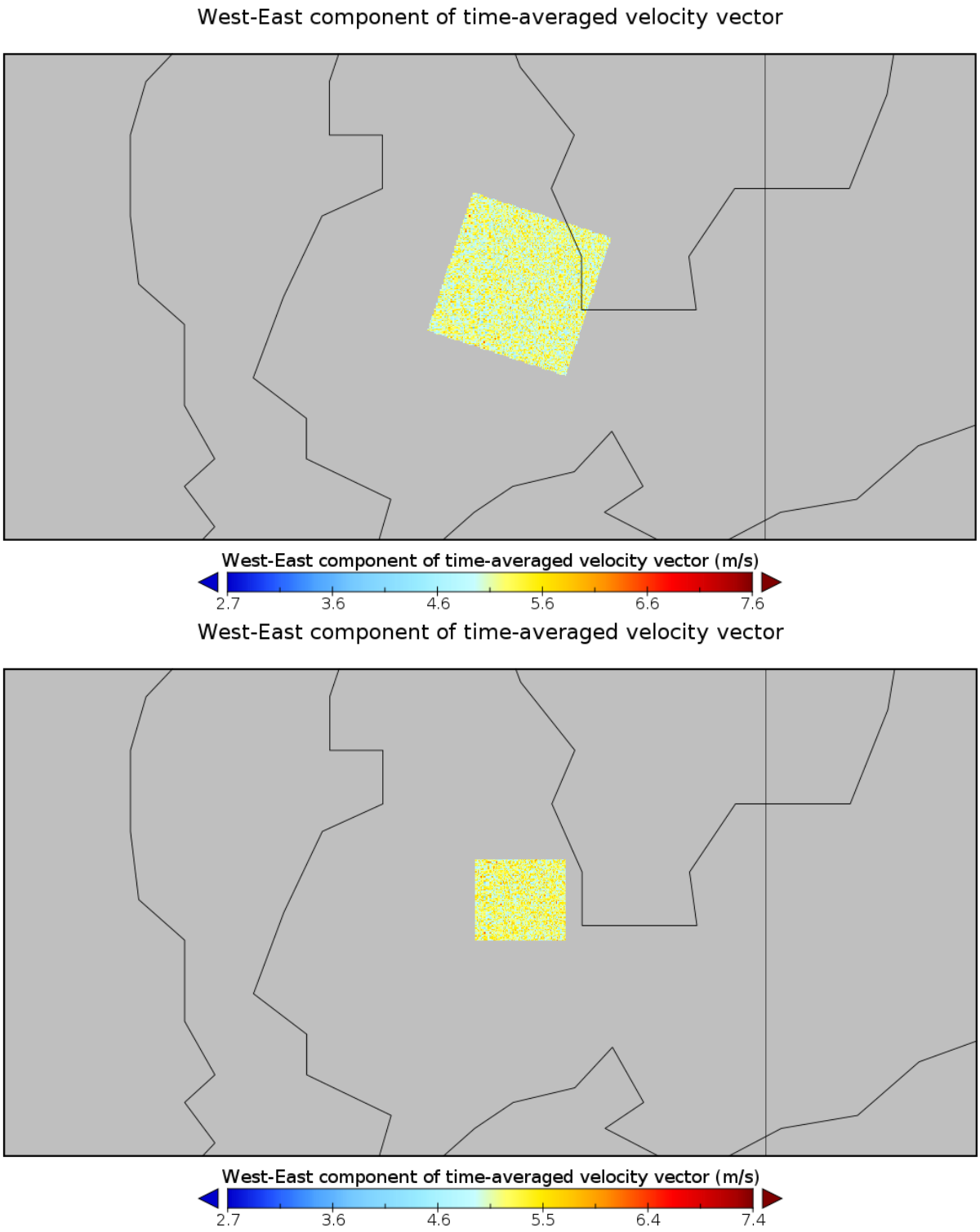


***Figure** 2-**24** – 'REMO + white noise' 10 m wind field (W-E component) in netCDF format (visualised in Panoply). Top panel: regular cartesian ATHAM-Fluidity grid. Bottom panel: regular lat-lon grid.*

## 2.7 Discussion

The role of ATHAM-Fluidity within the new PEARL integrated modelling framework has been demonstrated in this report. Although there is more code development needed before the model is fully functional, much progress has been made and the work presented here serves as a proof of concept. A strategy for coupling the REMO climate model to ATHAM-Fluidity has been presented, in

which the vertical atmospheric profiles over Greve from the REMO model output are extracted and processed into a format that can be used to drive the inflow conditions at the ATHAM-Fluidity inlet boundary. Similarly, procedures for converting the ATHAM-Fluidity output of 10 m wind fields to a format that can be read in by the wave model, and the output of surface precipitation fields to a format that can be read in by the wave model, have been outlined. Full-scale simulations have also been set up in preparation for adequate computing resources becoming available. Smaller-scale simulations have been conducted in order to test the transfer of data from ATHAM-Fluidity to the wave models, and to verify the capability of the microphysics scheme to simulate cloud and precipitation formation.

The developments that are necessary before ATHAM-Fluidity can be considered fully functional include a method for generating fully unstructured anisotropic finite-element meshes in order for surface topography and distinct land-sea surfaces to be included whilst also maintaining an aspect ratio that allows for finer resolution than horizontal resolution, and the capability to handle veering wind profiles at the inlet boundaries.

# 3 A new integrated 2D/3D adaptive unstructured mesh model for urban flooding and applications to Glasgow and Greve (Contribution from Imperial College London)[2]

## 3.1 Introduction

The combined effect of population growth and industrialisation in the EU countries means that coastal land areas are increasingly occupied by multiple user groups with diverse and competing needs (e.g. environmental, tourism, industrial). An important aspect of climate change is the increased likelihood of storms, and hence storm-surges, heave rainfall and flooding, and this will have obvious impact upon low lying areas susceptible to diverse risks. There is thus an increased need to improve predictions (especially over a wide range of spatial scales - metres to many kilometres) and assess their impact, thereby helping policy makers, rescue services and scientists involved with ocean, climate change and risk reduction strategies. It is now generally recognised that the next generation of atmospheric/ocean models will be based on unstructured mesh technology as they are currently the only feasible way of resolving the important range of scales in coastal and urban regions. As increasing demands are made on models there will be an increasing need for flexibility in mesh resolution including in the vertical dimension.

Using current technologies, events such as coastal and urban floods, storm-surges, pluvial (rain-induced) and fluvial (river) flooding are tackled independently in a piecemeal fashion. Experience from the recent seismic and subsequent tsunami events in Japan indicates that planning for these hazards as separate events leaves huge gaps in resilience with settlements and structures along coastal areas remaining highly vulnerable. There is great potential for innovations that would reshape the whole procedure for managing the coincidence of two or three types of natural hazards that happen either simultaneously or are causally-linked and happen unexpectedly over a short time scale. Many EU cities need a response plan for management of these types of disasters and, where possible, a predictive capability before, during and after a flooding disaster. Planning for future water and geo-induced disasters in urban, industrial or even rural areas requires the next generation of integrated models. This has drawn more attention in urban flooding research, hence increasing the effort in flood modelling (Schmitt et al., 2004; Van Dijk et al., 2014; Borsche and Klar, 2014; Son, 2016). Urban flood modelling plays a key role in assessment of flood risk in urban areas by providing detailed information of the flooding process (e.g. location, depth and velocity of flooding). Accurate modelling results are the basis of reliable flood risk evaluation.

### 3.1.1 3D urban flooding modelling (From Zhang et al, 2016)

Most of the extensive literature on urban flooding uses either 2D models (Liang et al., 2008; Bellos and Tsakiris, 2015) or 1D/2D coupled models (Schubert et al., 2008) in order to obtain high speed modelling. However, urban flood flows have three-dimensional (3D) characteristics. This is because,

[2] This is the work from Rong Hu and Ting Zhang's PhD study and part of their thesis/papers.

in urban areas, buildings behave as obstacles, leading to hydrodynamic forces like stagnation pressure, lateral shear and flow separation (LaRocque et al., 2013). Lane et al. (1999) found that 3D computational fluid dynamics (CFD) models provide more reliable estimates of bed shear stress. They provide more information of the 3D flow structures, and better representation of the flow process than 2D models. Therefore， three-dimensional models， in combination with higher-quality of datasets are required in order to improve our understanding of urban flooding.

### 3.1.2 Adaptive unstructured mesh flooding modelling (Hu et al., 2017a and 2017b)

To provide reliable flooding predictions in urban areas, high-resolution simulation is essential in order to resolve the complex urban topographic features, for example, buildings, streets and embankments. However, the high computational burden associated with fully hydrodynamic models has restricted their wider application to real-time urban flooding.

To improve modelling efficiency and accuracy for flood inundation, numerous methods including grid coarsening methods (Hartnack et al., 2009), cellular automata approach (Dottori and Todini, 2011), and speeding-up strategies focusing on parallel processing and hardware advances have been recently developed. Chen et al. (2012) used a Building Coverage Ratio (BCR) and a Conveyance Reduction Factor (CRF) parameters to simplify the key features of building within a coarse grid. Leandro et al. (2014) developed a parallelized two-dimensional diffusive wave model (P-DWave) with an adaptive time step using the Matlab parallel computing toolbox and Fortran OpenMP Application Programming. Smith et al. (2015) presented a new hydrodynamic modelling framework and described how a robust finite-volume Godunov-type scheme was implemented and applied it to simulate urban flooding with a high-resolution grid. Parallel computation was achieved with either central processing units (CPU) or graphics processing units (GPU) devices.

Another effective means to reduce the high computational burden in the full dynamic inundation models is to use a refined mesh only within those areas of interest. The use of coarse resolution meshes may cause unrealistic results such as ponds not being drained or the influence of buildings not being represented accurately, whereas the use of high-resolution meshes in the whole computational domain may make the simulation unacceptably slow (Chen et al., 2007). It is desirable to apply finer meshes only in specific regions where the gradients of the flow variables are relatively steep, rather than in areas where inundation has not yet occurred (Zhou et al., 2013). Given that, the adaptive mesh refinement (AMR) (a fine structured mesh nested within a coarse mesh) technique has been developed by Berger and Oliger (1984) and Berger and Colella (1989). George (2011) improved this approach and applied it to dam break flow modelling. The key feature of AMR is generating the sub-meshes by moving and adding grid points or cells. This mesh refinement can be achieved based on structured or unstructured meshes. Compared with structured meshes, unstructured meshes are able to represent better complex domain geometries and boundaries. However, unstructured grid-based AMR is more computationally demanding than structured grid-based AMR. George (2011) concluded that the shallow water model with AMR is efficient and suitable for flood simulation. Another extension of AMR is adaptive quadtree grids approach (Liang et al., 2004). It uses a quadtree and hierarchical data structure to carry out AMR. Liang (2012) recently simplified this data structure and tested the new adaptive structured mesh system by implementing in different numerical schemes (Wang and Liang, 2011). Their adaptive structured mesh model is found to be more efficient, compared with its uniform mesh counterpart. The wetting and drying (WD) algorithm has also been widely applied to overland flooding and inundation. It enables the models to capture the physics of an advancing or receding wetting front with mass conservation. Numeric schemes such as finite difference (FD), finite element (FE), and finite volume (FV) methods are generally used to address WD in flooding models. As reviewed in Medeiros and Hagen (2013), simulating WD over a real domain is

still nontrivial, due to the fact that accurate solutions requiring high spatial and temporal resolutions are unstable and computationally expensive.

In the PEARL project we have developed an adaptive unstructured mesh modelling framework for flood modelling. The main novelty of our work is the first use of a new anisotropic hr-adaptive mesh technique for flooding modelling. This adaptive unstructured mesh technique can modify and adapt unstructured meshes to better capture the features of flooding flow and reduce computational cost without sacrificing accuracy. Using the hr-adaptive technique, the mesh nodes can either be increased or decreased locally in time and space (h-adaptive technique) with a good solution accuracy (Piggott et al., 2005), or optimally relocated (r-adaptive technique) to resolve the small-scale flow features in a domain of interest (e.g. features of flow around buildings). This adaptive unstructured mesh technique has been applied to ocean, air pollution, multiphase flows and reservoir modelling (Du et al., 2016; Zheng et al., 2015; Su et al., 2015; Xie et al., 2017; Jackson et al., 2015). In this work, this 2D (two-dimensional) control-volume and finite-element method with the adaptive unstructured mesh technique is first developed for urban flooding modelling and validated using Glasgow's urban flooding in 2002 as a benchmark case (not one case study in PEARL) and successfully applied to Greve case in Denmark (one case study in PEARL).

## 3.2 A new integrated 2D/3D adaptive/fixed unstructured mesh model for individual and coinciding urban flooding

### 3.2.1 Introduction of a 2D/3D unstructured mesh urban flooding model

**In the PEARL project, a new 2D/3D adaptive/fixed unstructured urban flooding model (Floodity) has been developed** which can be used to model urban flooding in a wide range of flooding scale, including resolving down to building-scale.

1. ***3D flooding models*** can resolve the vertical (e.g. non-hydrostatic effects - vertical inertia) but possibly maintain efficiency at the cost of limiting the vertical resolution. For instance, a single P0 element (constant across an element) may be used in the vertical, while maintaining the higher order polynomial representation in the horizontal. This results in something similar to the shallow water equations, but there is the possibility of adapting the vertical resolution, which is non-uniform in space, to maintain the speed of the shallow water equations and the accuracy of the vertical resolution approach. If a specified vertical resolution is used, for example, one linear of quadratic element in the vertical, then the speed of the simulations (assuming non-hydrostatic effects are not large) will be the same order as the speed of a 2D shallow water model, but with the constant of proportionality being potentially large e.g. 10-100. Effort is needed to quantify the need for 3D in both idealized (e.g. supercritical and hydraulic jump flows) and flows with steep slopes or fast flow interactions with obstacles like buildings, as well as, realistic problems, see Glasgow benchmark problem in Chapter 3.3. These 3D methods enable the forces on buildings to be more accurately predicted, for example.
2. ***2D flooding modelswith advanced adaptive mesh techniques*** are efficient and often adequate in urban areas. Here we have developed new methods for this, including the exploration of new elements for flooding e.g. the use of balance elements P1DG-P2 (discontinuous linear triangles for velocity and continuous six node quadratic triangles for free/surface) and simpler elements P1DG-P1 or P0DG-P1 (discontinuous constant variation across each triangle for velocity and continuous linear triangular elements for resolving water depth). For simplicity and rapid simulation, we have adopted modification of the P1DG-P1 element in our simulations. That is, we are using the new double control volume formulation of pressure (P1DG-P1CV) method (Salinas et al. 2017) This formulation has the major advantage that it can enable elements with large angles to be used, when highly anisotropic elements are used. We also use flux limiting of the free surface height based on the Normalized Variable Diagram approach of Leonard 1988. In

addition, we use a non-linear two-time level theta method for the time stepping method in which the value of theta is adjusted (in space and time) so that it is second-order accurate as much as possible theta=0.5 (Crank Nicolson time stepping) but resorts to using theta=1 (backward Euler) if an oscillation is detected because of the time stepping. This is achieved based on a Total Variational Diminishing in time condition, see Pavlidis et. al. 2015. The non-linear iteration is based on the fixed-point iteration method described in Salinas et al. 2017. This is important as wetting and drying (due to the non-linear drag and inertia) is highly non-linear. The Discontinuous Galerkin (DG) method applied to momentum/velocity is very powerful as it has a natural dissipation associated with it, which is highly scale selective - it has a $4^{th}$ order truncation term based on Taylor series analysis.

### 3.2.2 Adaptive mesh techniques

The dynamically adaptive unstructured mesh technique developed by Pain et al. (2001) is utilized here. This method has the advantage of capturing details of surface and local flows (wetting-drying front) during the process of flooding modelling. It can efficiently provide a high mesh resolution where and when it is needed. That is, finer meshes are placed only in specific regions where the variations of flow variable solutions are relatively large (e.g. flow around buildings and along the flooding paths), while coarser meshes are used in areas far from these regions, where inundation has not yet occurred for example.

The optimization-based adaptive mesh technique used here relies on the derivation of appropriate error measures, which dictate how the mesh is to be modified (Pain et al., 2001). The error measure employed is based on the curvature of variable solutions and provides a directional measure. By using a Riemannian metric to calculate the element size and shape, the mesh is adapted to have a uniform interpolation error in any direction. In this metric space, a functional which is used to gauge the shape and size quality of elements is defined. A series of the mesh connectivity and node position searches are performed to optimize this functional. The mesh modification thus fits the solution field(s) in an optimal manner.

In addition, it is only fairly recently that conservation can be achieved when interpolating from mesh to mesh during a dynamic mesh adaptive simulation or when exchanging information between models e.g. at boundaries where forcing occurs. This mesh to mesh interpolation was first achieved for finite elements methods by Farrell et al. (2009) and very recently, within this project, by Adam et al. (2016) for the control-volume class of methods. The latter is particularly important, due to the dominance of the use of control-volume methods in natural hazard models e.g. flooding and atmospheric flows.

### 3.2.3 2D and 3D parallel computing

Our new 2D and 3D flooding models have excellent parallel modelling capabilities, which is based on domain decomposition methods (DDMs) in which the domain is divided into a number of sub-domains. In the ideal circumstances, e.g. large problems, the stable version of fluidity has been shown to scale to O(100K) cores. However, this scaling depends on the physics as well. The 2D and 3D DDMs only scale well with more than 20K elements per core and a similar restriction applies when mesh adaptivity is used. The former restriction is due to the efficiency of the solver technology, which is based on PETSc or, for high aspect ratio environmental problems, a specially designed solver which scales independent of aspect ratio of the problem, see Kramer et al. (2009). These are amongst the best performing multi-grid solvers in parallel, but still have this restriction in terms of the minimum number of elements needed to have good scaling in parallel. When mesh adaptivity is used, then the sub-domains need to be re-balanced, after every adapt of the mesh, in order to balance the computational CPU load on each core, as well as minimize communication. The load balancing is achieved using PARMETIS. Few models have this unstructured mesh parallel mesh adaptivity/optimization capability, worldwide, but the technological barrier is very high. However, it

may be important for large scale natural hazards problems of the future. Parallel computing will give the scaling required, and the mesh adaptivity will only put the resolution where required.

## 3.3 Case study one: 3D fixed and 2D adaptive unstructured mesh flooding modelling and application to benchmark case study area in Glasgow (Hu et al., 2017. Zhang et al., 2016)

A flooding event in 2002 in Glasgow, Scotland, United Kingdom has been simulated to demonstrate the capability of the 3D fixed and 2D adaptive unstructured mesh flooding models. The simulations have been performed using both the fixed and adaptive unstructured meshes, and then validated by comparing the results with published 2D and 3D model results. The presented method shows that the 2D adaptive mesh model provides accurate results while having a low computational cost. This new adaptive unstructured mesh flooding model can provide reliable information and solutions for urban flooding. The simulations have been performed using both the fixed and adaptive unstructured meshes, and then validated by comparing the results with published 2D and 3D model results. Our results show that the 2D adaptive mesh model provides accurate results while having a low computational cost. This new adaptive unstructured mesh flooding model is capable of providing reliable information and solutions for urban flooding.

### 3.3.1 Descriptions of study site and data

The models were applied to an urban area located within the city of Glasgow, Scotland, UK, in which a flood occurred in July 2002. The whole computational domain is 1.0 km by 0.4 km (Figure 3-1). Flooding is caused by a stream from a culvert located at the northeast corner of the domain (see location Q in Figure 3-1). This flood is observed as a result of flow exceeding the capacity of the culvert during the period of prolonged or heavy rainfall. Once the capacity of the culvert is exceeded, water spills onto the road network and flow diverges, with water moving along the main street and several branches. This scenario forms the basis for flood modelling performed in this study. Details about the hydrograph can be found in literatures (Hunter et al., 2008; Liang et al., 2007). Figure 3-2 shows the unstructured meshes created as 2D (triangle elements) by Gmsh (Geuzaine and Remacle, 2009), a free finite element grid generator with a build-in CAD engine and post-processor. The surrounding mesh of the main street and several branches is refined.

The raw LiDAR data was originally collected by Infoterra Ltd., Leicester, UK, for Glasgow City Council. For hydraulic modelling, Infoterra aggregated the LiDAR data and reinserted buildings, kerbs and roads to obtain a 2m DEM with realistic representation of urban morphologic characteristics (Hunter et al., 2008). Flood depth time series at four detector locations (Figure 3-1) obtained by Hunter et al. (2008) are utilized for model validation in this study.

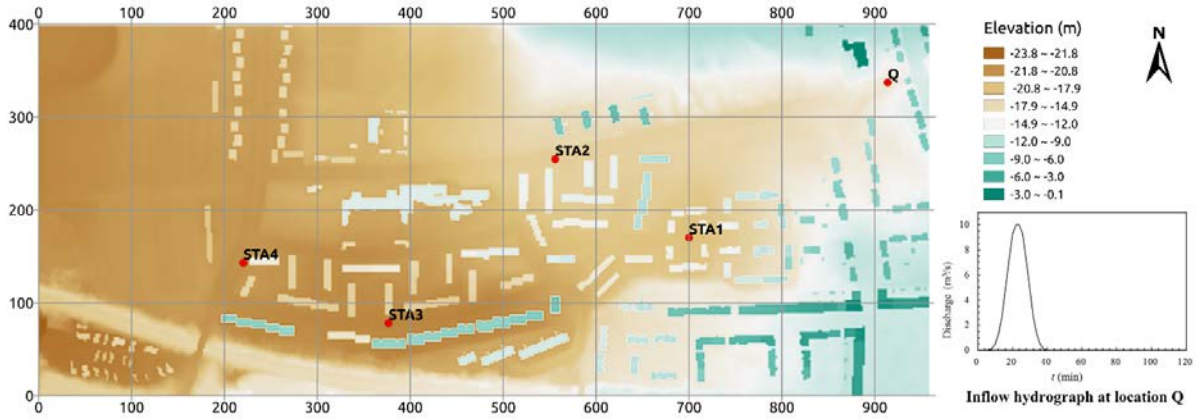


***Figure 3-1*** *LiDAR DTM with buildings of modelling domain and locations of monitoring stations.*

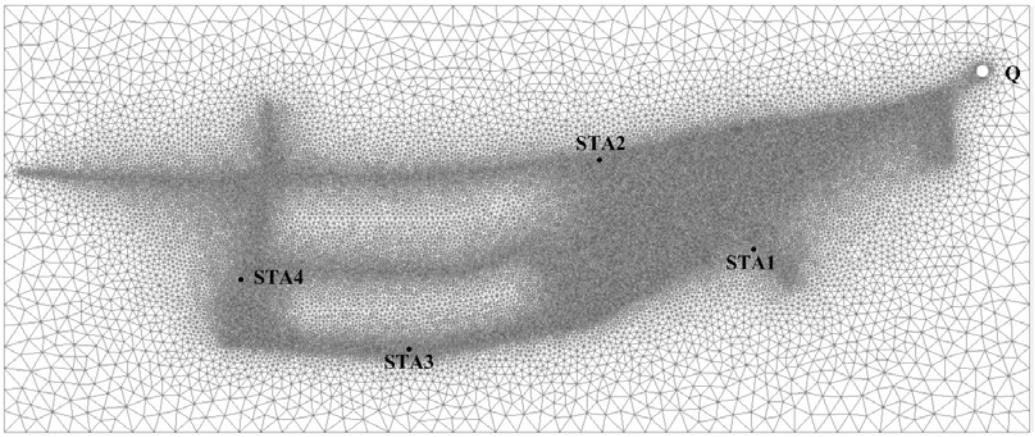


***Figure 3-2*** *Multi-scale unstructured mesh with 2m/5m/20m resolution generated by Gmsh.*

### 3.3.2 Results and Discussion

Figure 3-3 shows the water depth and velocity simulated by 3D modelling (Zhang et al., 2016), and 2D fixed and adaptive unstructured mesh modelling at time levels *t*=20, 30, 40, 60 *min*. They demonstrate the flood propagation process over the whole flooding area. Compared with the results of 3D modelling, it can be observed that in most of the inundation area, the solutions of water depth and velocity obtained from both 2D fixed and adaptive mesh modelling are in agreement with those of 3D modelling. The flood propagation process is accelerating during [22 - 24] *min* when the inflow discharge at location Q peaks. The water spreads along the main street and several branches when *t*= 30 *min*. After *t*= 40 *min,* water accumulates in the low-lying areas, especially in the southern street area marked with a rectangle in Figure 3-3.

The flood extent simulated by 2D fixed and 2D adaptive unstructured mesh models is mostly in agreement with that by 3D modelling (Zhang et al., 2016). 3D results have been proved to be consistent with results of the four 2D models from (Hunter et al., 2008) in the region where the impact of 3D flow structures can be ignored. Consequently, these 3D results can be used to validate 2D models. It can be found, that with fixed or adaptive unstructured mesh technology, these 2D models perform well and are able to predict similar results as 3D models. Furthermore, providing accurate results, the 2D adaptive mesh model (Hu et al., 2017a) uses mesh with much less nodes and elements than that of 2D fixed mesh model, which lowers the computational cost considerably.

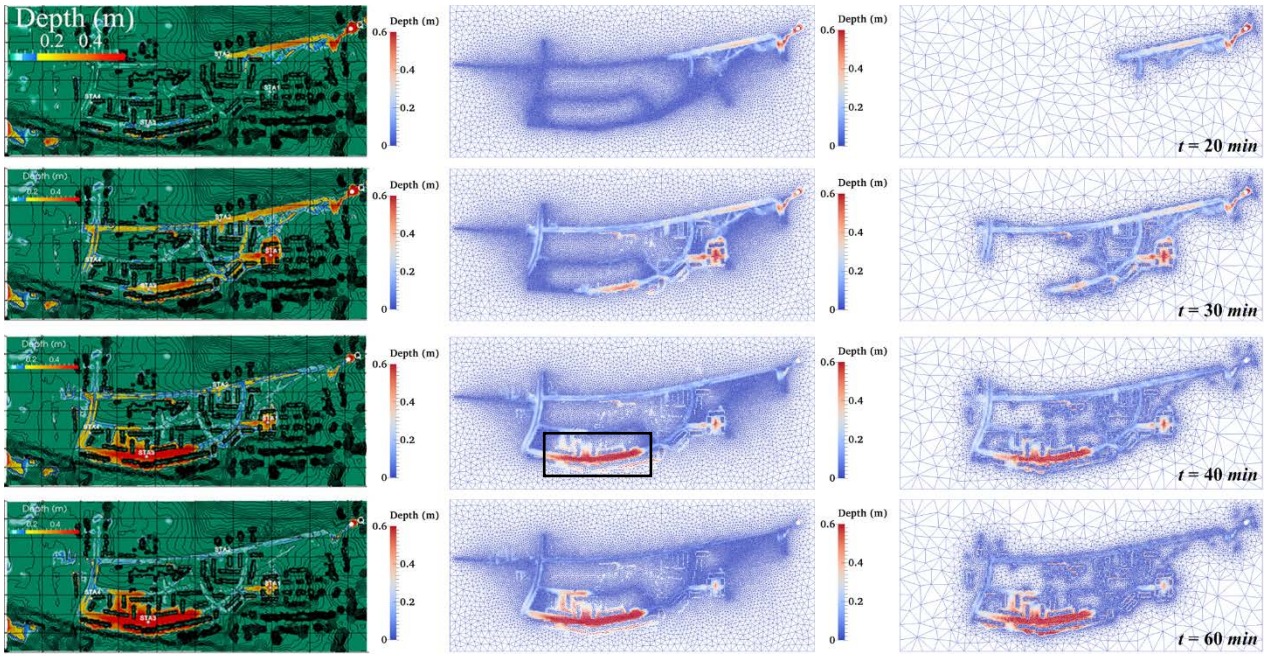


***Figure 3-3*** *Depth obtained from 3D modelling (left column, see (Zhang et al., 2016)), 2D fixed unstructured mesh modelling (middle column) and 2D adaptive unstructured mesh modelling (right column, see (Hu et al., 2017)) at time level t=20 min (first row), 30 min (second row), 40 min (third row) and 60 min (bottom row).*

To further validate the results of our 2D fixed and adaptive unstructured mesh models (Hu et al., 2017a), the time series of water depth at detector location STA3 are compared with those of six 2D hydraulic models (DIVAST, DIVAST-TVD, JFLOW, LISFLOOD-FP, TRENT, and TUFLOW) from (Hunter et al., 2008) and the 3D model (Zhang et al., 2016). STA3 is located in the low-lying area in the southern part of the domain as marked with a rectangle in Figure 3-3. In Figure 3-4, the black and red lines represent the time series of water depth predicted by 2D fixed and adaptive unstructured mesh models respectively. It can be seen that a good agreement is achieved between the results from 2D fixed (adaptive) unstructured mesh models and those from other 2D models at one detector location.

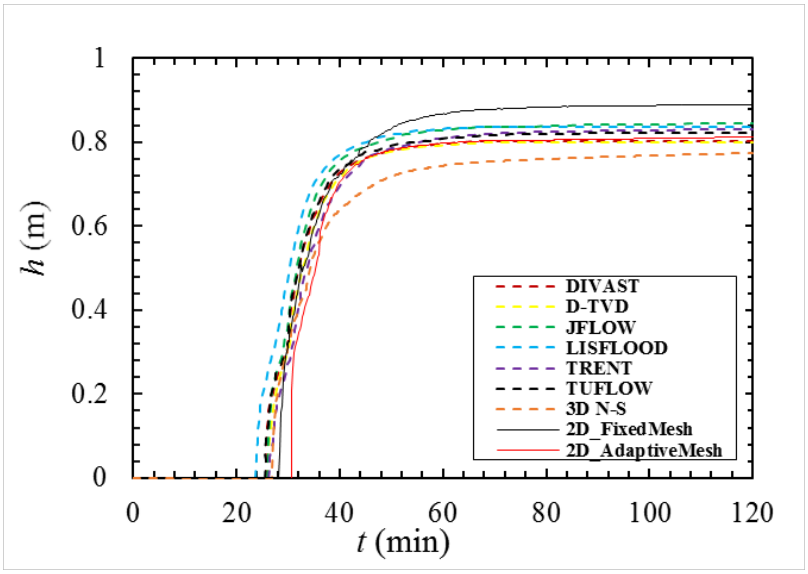


***Figure 3-4*** *Flood depth time series at detector location STA3 simulated by 2D fixed and 2D adaptive unstructured mesh models and various published models.*

## 3.4 Case study two: 2D adaptive mesh Modelling of extreme events individually and in coincidence in Greve (Hu et al., 2017b)

### 3.4.1 Description of Study Area

The study area covers part of the coastal area of Greve in eastern Denmark (see Figure 3-5). The area has a flood history including flooding from extreme rain events and flood from the sea. Much has been done to reduce the flood risk due to extreme rain events, but it can never be eliminated. Coupled rain events are a serious concern for the city especially due to climate change in future. In July 2007, a series of rain events, with a joint probability of occurrence of 500 years caused severe flooding in Greve. In addition to extreme rainfall, Greve is also vulnerable to flooding from extreme sea levels along its coast. In the more distant past the area has been flooded due to very serious storm surges, e.g. the 13th October 1760 with a water level of 3,7m. If any of these to floods are repeated today they would cause very serious damage.

In the Greve case study, the data used includes, DTM data with buildings and with resolution of 1.6m (Figure 3-6), extreme water levels (Figure 3-7) as boundary conditions, rainfall data (Figure 3-8). The DTM used was detailed enough to describe relevant surface features. It had a resolution of 1.6m x 1.6 m to describe the flow along the main streets of Greve without a high computational effort although buildings were included in the models.

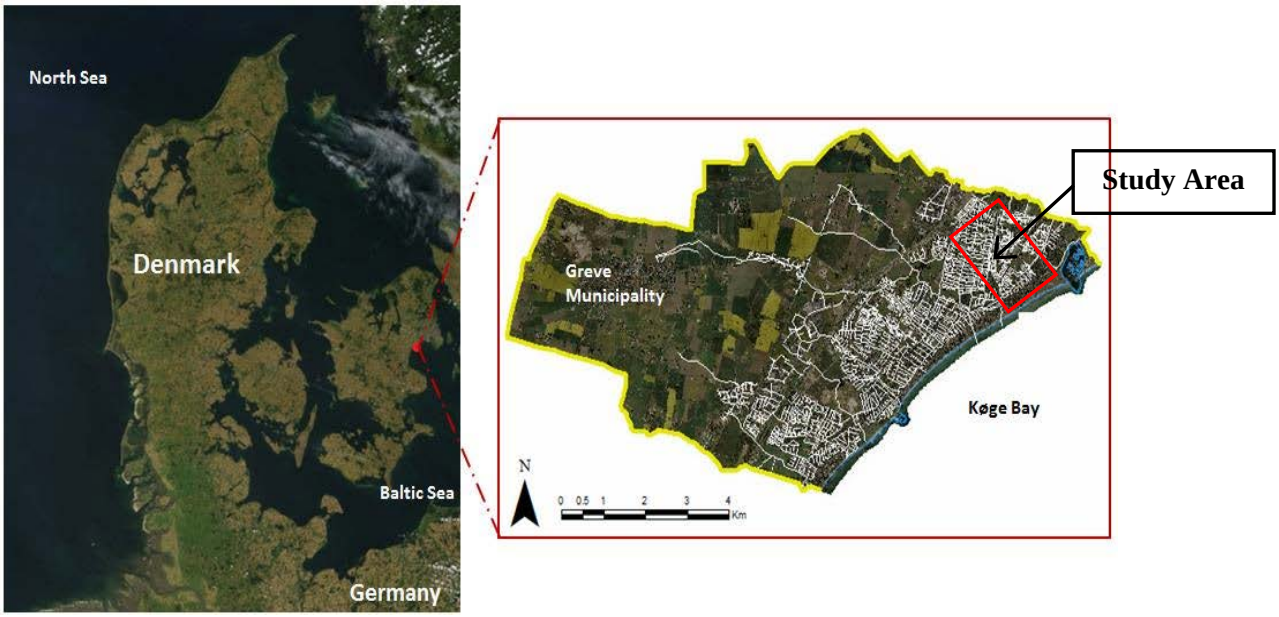


***Figure 3-5*** *Situation of Study Area in Greve Municipality of Denmark, see Soledad (2014).*

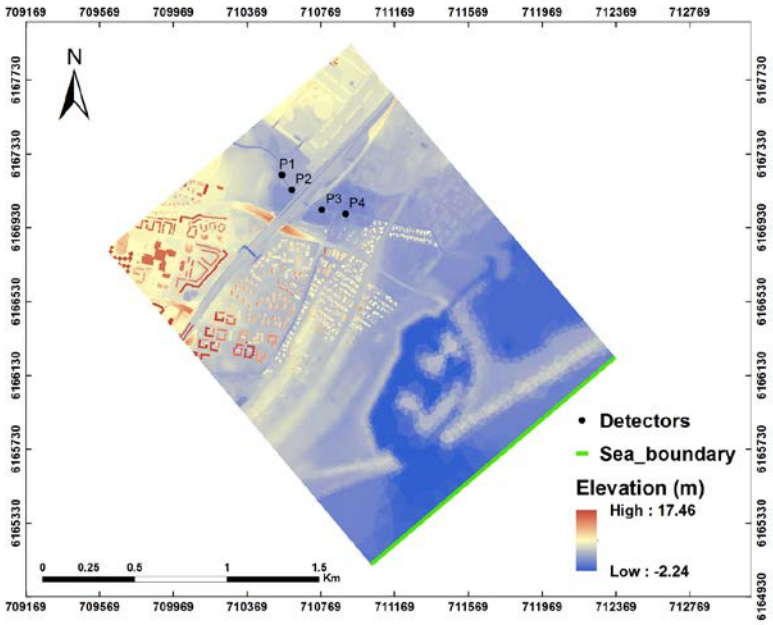


***Figure 3-6*** *DTM with Buildings of Study Area (resolution of 1.6mx1.6m) - generated by the GIS (Geographical Information System) software, see ArcGIS(2010).*

### 3.4.2 Data collection and customisation

#### *3.4.2.1 Extreme Sea-Level Event*

The future extreme events used in this research as input boundary conditions along the coastal line (Figure 3-7) were derived from these previous studies while the future climate change conditions were taken into account. The Event lasted 24 h. In this picture, one can observe that for a return period of 100

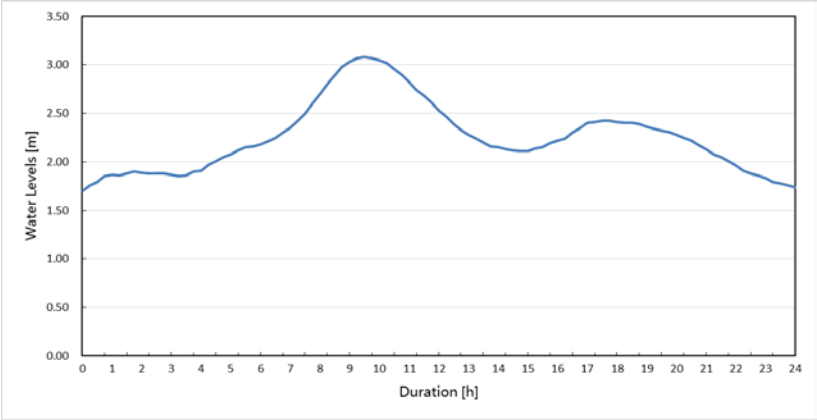


***Figure 3-7*** *Projections by 2100 of upper extreme water levels (considering the worst climate change scenario for 100-yr projection), see Soledad (2014).*

years, the maximum value for upper extreme water level is 3.08 m (Soledad, 2014).

#### *3.4.2.2 Extreme Precipitation Event (Soledad, 2014)*

For the design of urban flooding is necessary to consider current extreme rainfall events as well as the impact of climate change on future rainfall. For a place where rainfall measurements are available, a

frequency analysis can be developed to obtain the IDF (Intensity-Duration-Frequency) relationship. According to the Intergovernmental Panel on Climates Change (IPCC), more intense and frequent extreme rainfall is expected in the future in Denmark, especially during summer periods. Therefore, it was concluded that the design of extreme rainfall in Denmark should include the effects of a changing climate. In northern Europe it was studied by Arnbjerg-Nielsen who pointed out that the increase in design intensities depends on the duration and the return period being studied (Soledad, 2014). To consider the effects of climate change it is necessary to apply the climate factors into the design rainfall. These values indicate that design intensities in Denmark are likely to be increased by 10-50% within the next 100 years. For the present research, rainfall data from 83 stations at arbitrary location in Denmark that had more than 10 years of data were included in the analysis. To obtain the IDF curves a regional statistical extreme model was applied (Soledad, 2014). Figure 3-8 shows the extreme 24h design rainfall for 2-yr, 10-yr, 100-yr return period (considering the effects of climate change).

### 3.4.3 Setup of Model simulations

A series of model simulations using adaptive unstructured meshes have been carried out to assess the performance of the new flooding model developed here. The extreme water level event (Figure 3-7) which lasts 24 hours is used as an input along the coastal boundary (Figure 3-6) and the lateral boundaries are set up as closed (no flow). In these simulations, sea water enters the densely urbanized area from the sea boundary (Figure 3-6). Figure 3-9 shows the initial water depth within the domain in all simulations. For mesh adaptivity, when setting the maximum element size to be 200 and the minimum element size 10, a fixed time step Δt=5s is used. The anisotropic gradation algorithm is used and the aspect ratio in the adapted mesh is set to 5. The mesh is adapted considering the solutions of water depth, with the absolute interpolation errors set to be 0.025.

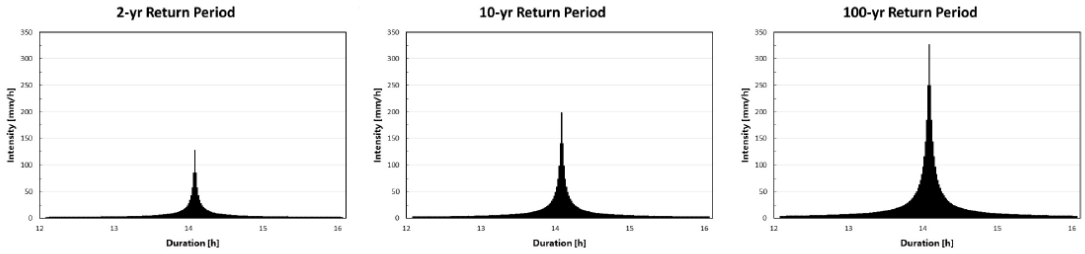


***Figure 3-8*** *Extreme 24h design rainfall for 2-yr, 10-yr, 100-yr return period (considering the effects of climate change), see Soledad (2014).*

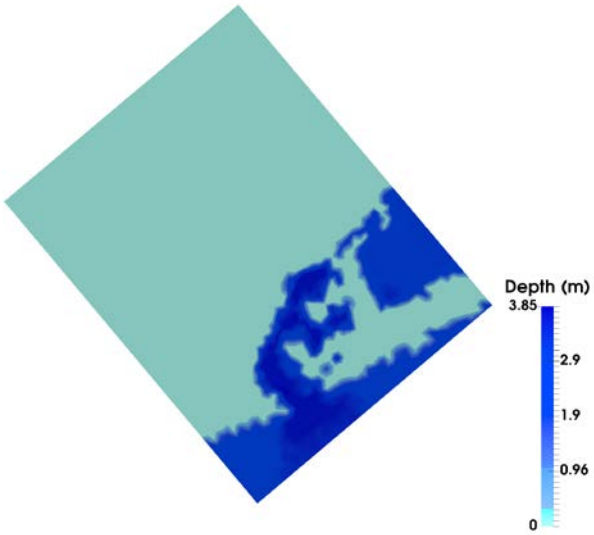


***Figure 3-9*** *Initial water depth in all simulations.*

### 3.4.4 Results and discussions: Individual flooding events (extreme sea-level event)

For comparison purposes, MIKE 21 results from Berbel Roman (2014) are used as a reference solution in this study. A uniform unstructured mesh with a resolution of 10m is used in the MIKE 21 simulations while the adaptive meshes with a minimum mesh size of 20m, 10m, and 5m in Floodity. A comparison of water depth results using the adaptive (Floodity) and fixed (MIKE 21) unstructured mesh has been carried out.

Figure 3-10 shows the flood propagation process over the urban area in a scenario of an individual extreme sea-level event. It can be observed that in most of the inundation area, the solutions of water depths obtained from Floodity are in good agreement with those from MIKE 21. The mesh is optimally adapted according to the evolving ow features in time and space, thus providing sufficient mesh resolution where and when it is required (right panel in Figure 3-10 and Figure 3-11). For example, the fine mesh is located along the flood propagation path while the coarser mesh is used in the areas where inundation has not occurred yet.

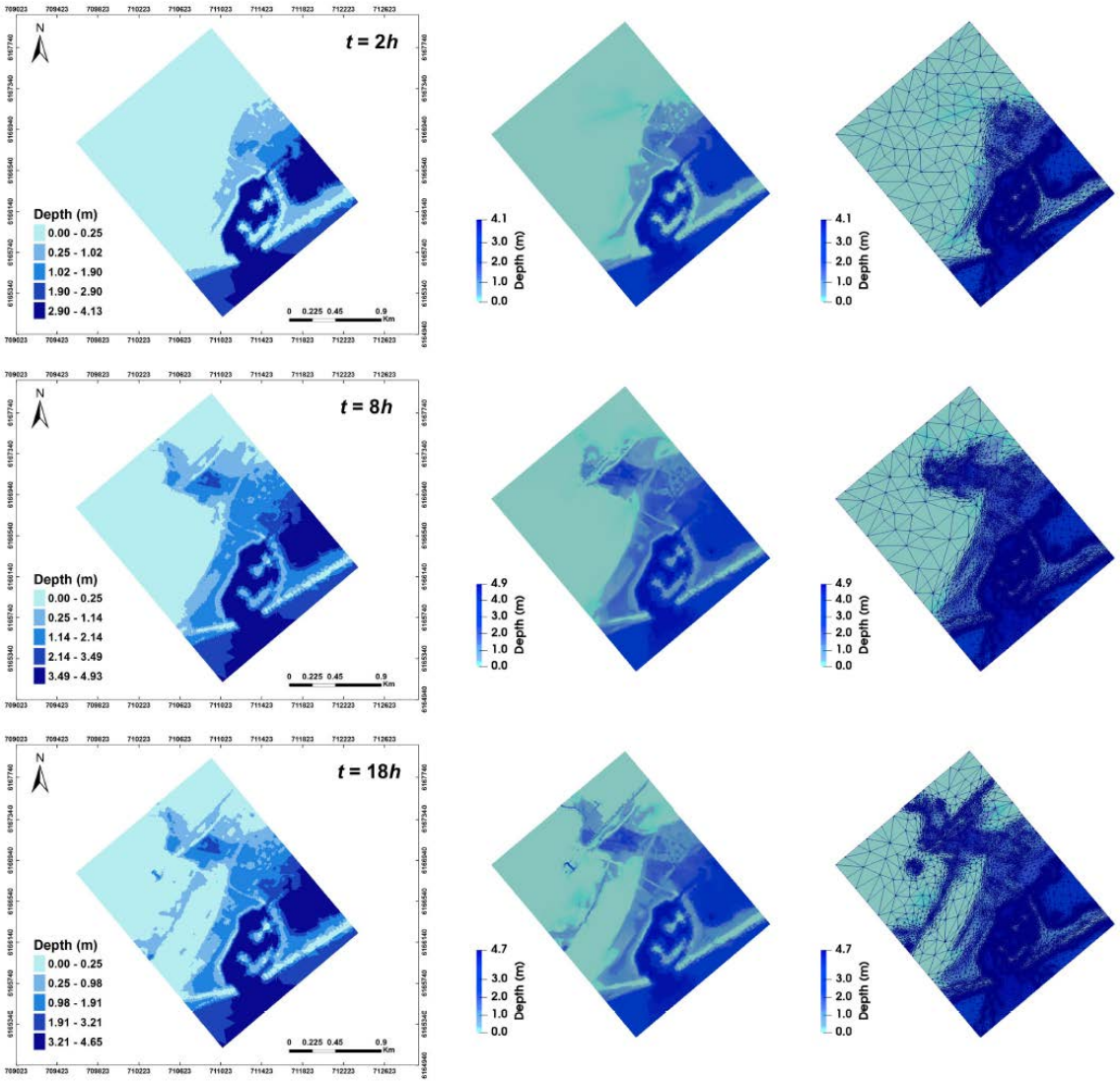


***Figure 3.10*** *Water depths obtained from a MIKE 21 model (left column, see Berbel Roman (2014)), a Floodity model with a mesh resolution 10m (middle column) and results showing the corresponding mesh (right column) based on bathymetric data without buildings in a scenario of extreme sea-level event at time level t = 2 h (first row), 8 h (middle row), and 18 h (bottom row).*

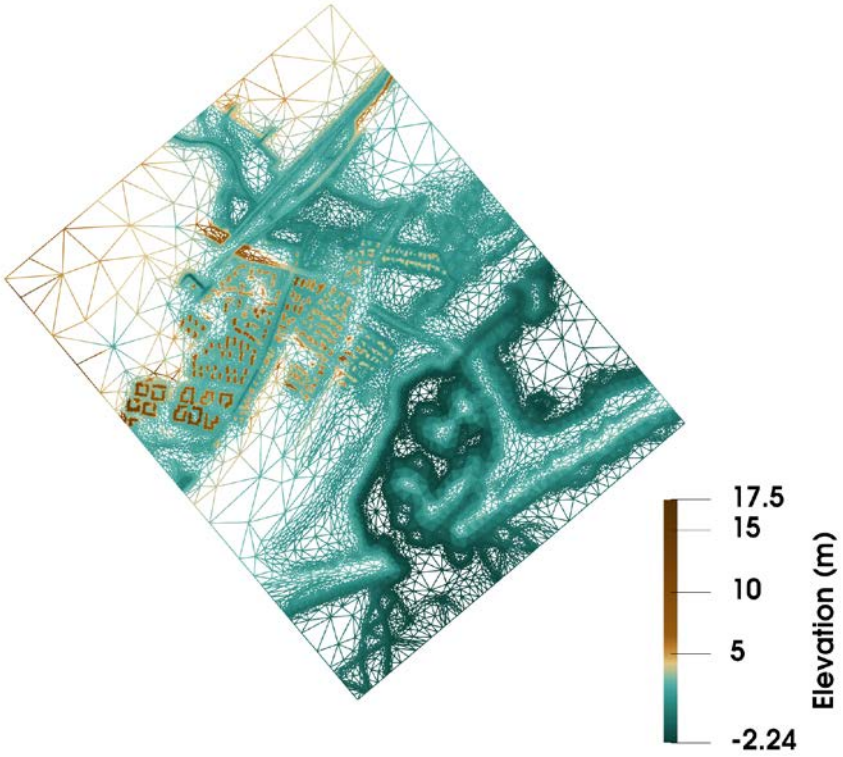


***Figure 3.11*** *Adaptive meshes at t =24 h overlapped with topography including buildings.*

### 3.4.5 Results and discussions: joint flooding events (Sea-Level and Precipitation Events)

#### *3.4.5.1 Flood map*

The newly developed adaptive mesh flooding model is further used for simulating floods under the combined impacts of the events (extreme rainfall and sea level). Figures 3-12, 3-13 and 3-14 show the results of water depth from MIKE 21 and Floodity with a minimum adaptive mesh size of 10m at time levels t = 24 h. It presents the flood propagation process over the urban area in scenarios of an extreme sea-level event and extreme rainfall events for the 2-yr,10-yr and 100-yr return periods respectively. It is seen that there is some difference (marked with rectangles in Figure 3-12) in flood extent of three extreme rainfall events from adaptive mesh flooding modelling. However, there is little difference among these areas from MIKE 21 results. It proves that more detailed results can be obtained in the local areas when using adaptive mesh instead of fixed mesh with the same mesh resolution.

The use of dynamic adaptive-mesh optimization technique (DMO) in flooding modelling can better capture the evolving flow features and topographic features (buildings, rivers and streets), thus providing improved accurate ooding prediction. To further demonstrate the capability of the flooding model, Floodity has been applied to the joint flooding events with the bathymetric data including buildings. Figures 3-12, 3-13, 3-14 present the flooding map over the urban area at time level t = 24 h in scenarios of three different joint flood events. It can be observed that Floodity results with a mesh resolution 5m have a larger inundation extent than MIKE 21 results and present more details of topographic features, including buildings and channels. The details of roads, buildings and channels can be observed clearly with an increased mesh resolution around them. Figure 3-15 provides the details of the areas marked with rectangles in Figure 3-12). It is noted that the information of roads and channels has been lost in the MIKE 21 simulations. However, with the use of anisotropic mesh

adaptivity, Floodity can capture the details of topographic features even with almost the same mesh resolution (10m) as that used in the MIKE simulation.
In these simulations, the topographical data (digital elevation data) is available with a high resolution of 1:6m. The availability of high-resolution topographical data is important for the accurate numerical simulation of urban food inundation. However, high-resolution topographical data requires a high computational burden, thus, resulting in a computationally demanding flood modelling. Using DMO. The topographical data over the domain is obtained by interpolating the high resolution (1:6m) data onto the adapted mesh at each time level. Therefore, the high-resolution topographical data is only used in the flooded region while the low-resolution data is used in the rest of the domain, thus reducing the computational cost. In addition, the details of buildings can be represented accurately as the flooding water spreads across the domain (see Figures 3-11, 3-12, 3-13, 3-14).

#### *3.4.5.2 Comparison with DHI MIKE results at detector locations*

To further validate our 2D adaptive unstructured mesh flooding models, the time series of water depth at detector locations P 1, P 2, P 3 and P 4 are compared with those of DHI MIKE model (Soledad, 2014). Figures. 3-16 - 18 shows the time series of water depth predicted by these models.

In Figures 3-16, 3-17 and 3-18, the green lines represent the time series of water depth predicted by the new 2D unstructured mesh flooding model with a mesh resolution 10m. It can be seen that a good agreement is achieved between the results from our 2D adaptive unstructured mesh models and those from the DHI MIKE model at all the detector locations. The results of our 2D unstructured mesh modelling results are very close to the DHI MIKE results (Soledad, 2014) except at detector P1 which is located within a small channel.

#### *3.4.5.3 Performance of 2D adaptive unstructured mesh flood modelling*

As seen in Table 3-1 and Figure 3-19, an unstructured mesh with 20m resolution generated by Gmsh (Geuzaine and Remacle, 2009) consists of 13033 nodes and 25666 unstructured triangle elements, while 10m resolution consists of 51367 nodes and 101939 elements, and 5m resolution mesh contains 204980 nodes and 408373 elements. These meshes are used during the whole simulation period for fixed unstructured mesh modelling, and used as the initial mesh for the adaptive mesh simulations. After first adapting the mesh, the numbers of nodes and elements used for adaptive mesh of 20m, 10m, and 5m resolution are reduced by 74%, 82% and 88% respectively, then gradually increased during t = 1 - 600 min and decreased during t = 600 - 1440 min as the flooding water retreats. Above all, Floodity is less computationally expensive than fixed unstructured mesh modelling. The use of adaptive unstructured meshes improves the computational efficiency. To further reduce the computational cost, various numerical techniques can be adopted in the flood model Floodity, for example, parallel computing using MPI.

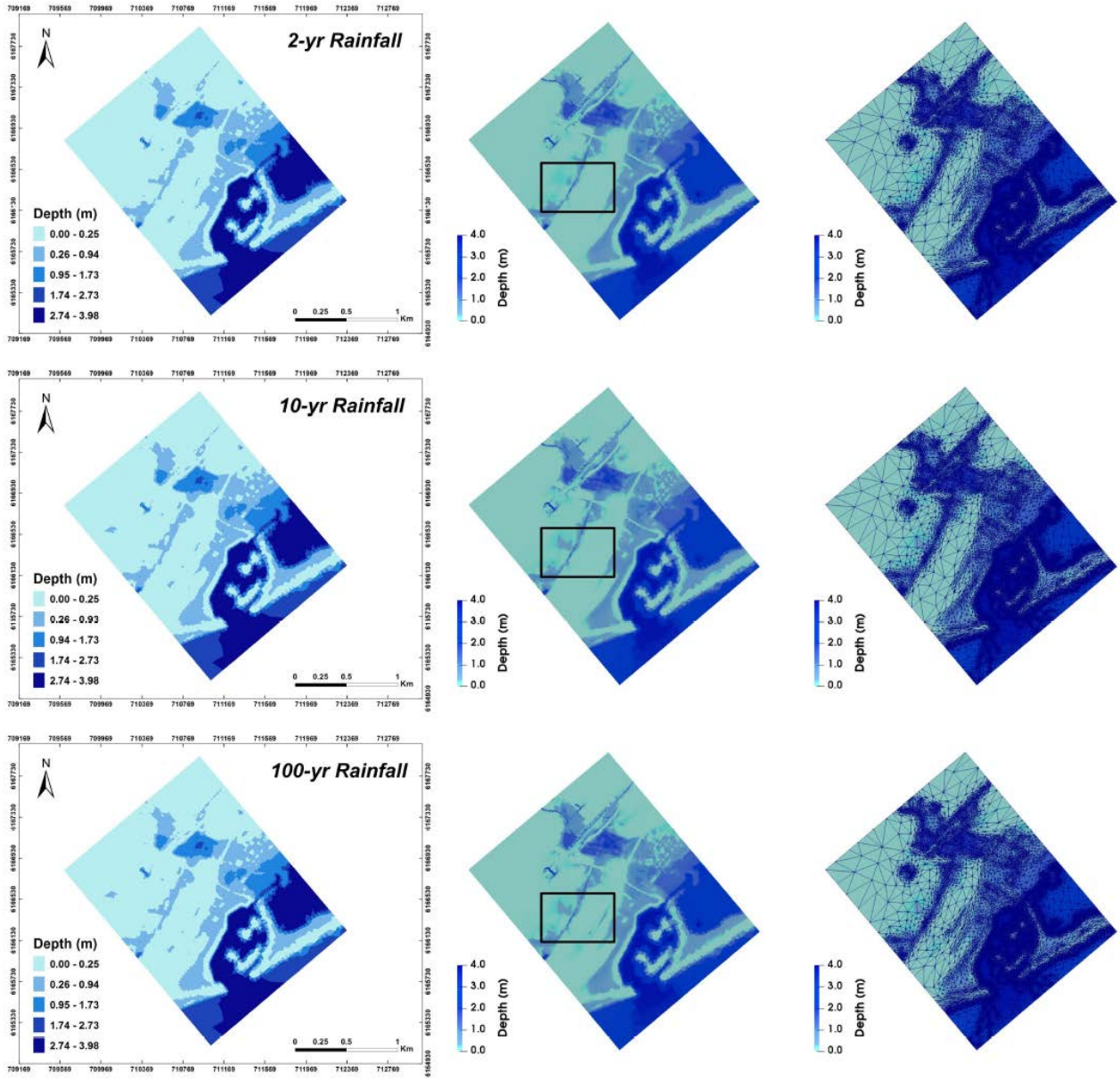


***Figure 3-12*** *Water depth obtained from DHI MIKE modelling (left column, see (Soledad, 2014)), 2D adaptive unstructured mesh modelling with a mesh resolution 10m (middle column) and the corresponding mesh on the surface (right column) in scenario of 2-yr return period rainfall and extreme sea-level event at time level t=12 h (first row), 15 h (second row), 18 h (third row) and 24 h (bottom row).*

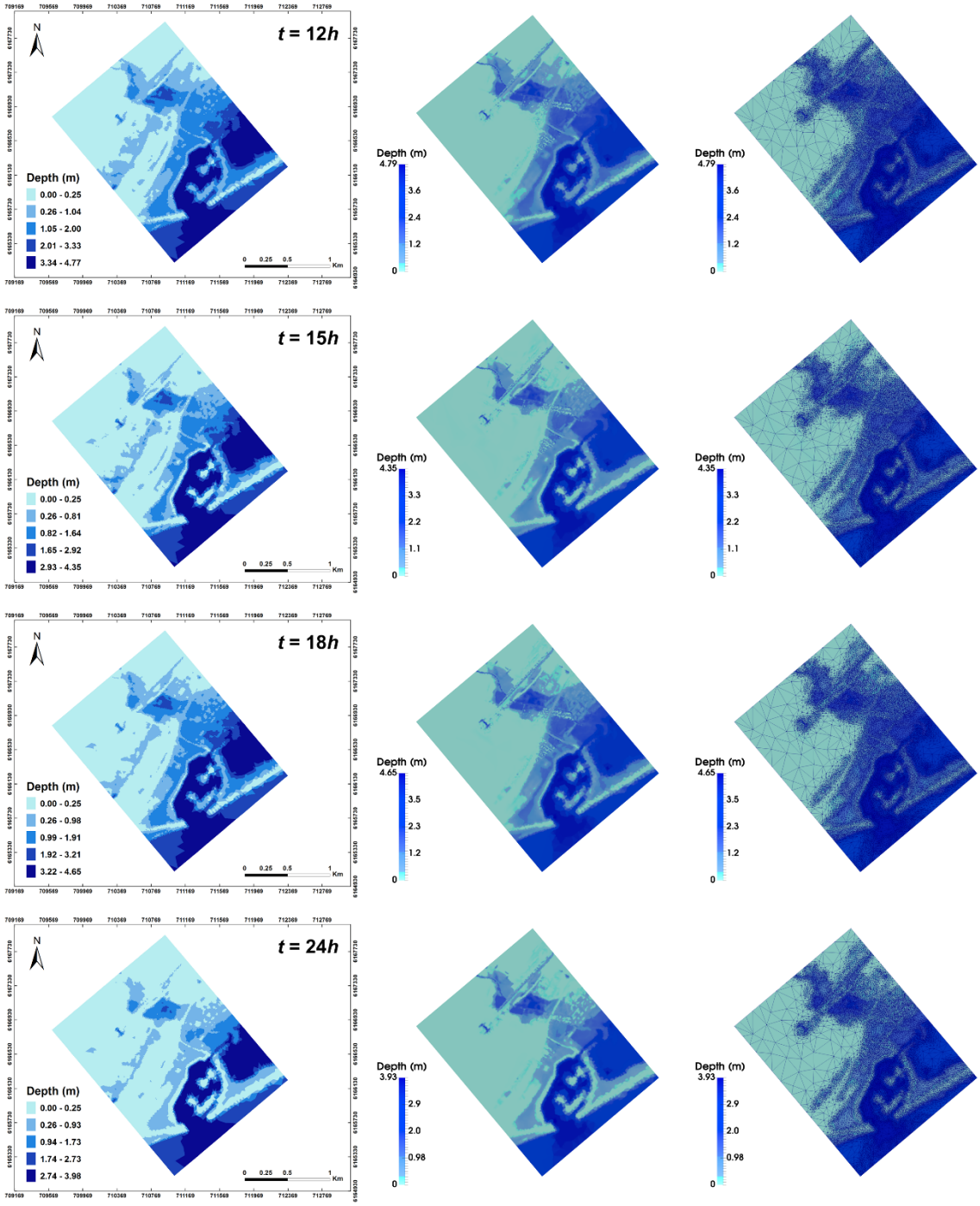


***Figure 3-13*** *As in Figure 3-11, except in scenario of 10-yr return period rainfall and extreme sea-level event at time level t=12 h (first row), 15 h (second row), 18 h (third row) and 24 h (bottom row).*

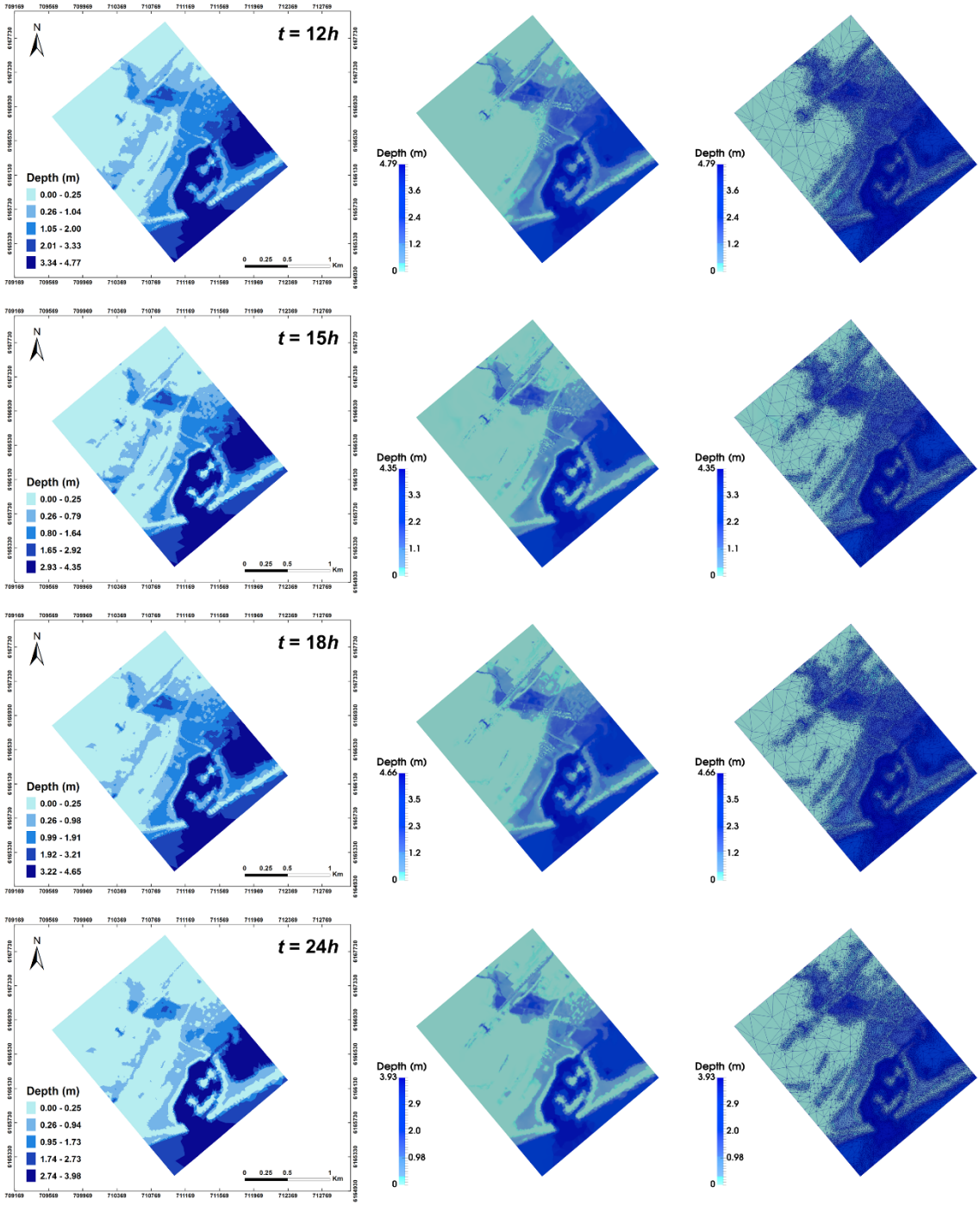


***Figure 3-14*** *As in Figure 3-12, except in scenario of 100-yr return period rainfall and extreme sea-level event at time level t=12 h (first row), 15 h (second row), 18 h (third row) and 24 h (bottom row).*

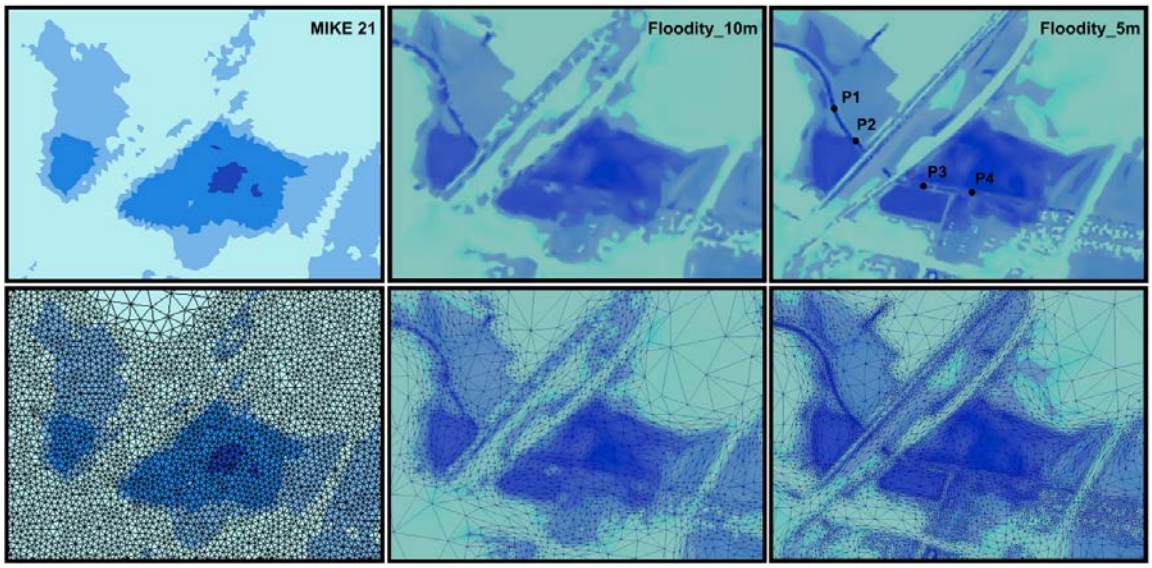


***Figure 3-15*** *Details of the areas marked with rectangles obtained from MIKE 21 modelling (left column), 2D adaptive unstructured mesh modelling with a mesh resolution 10m (middle column) and 5m (right column).*

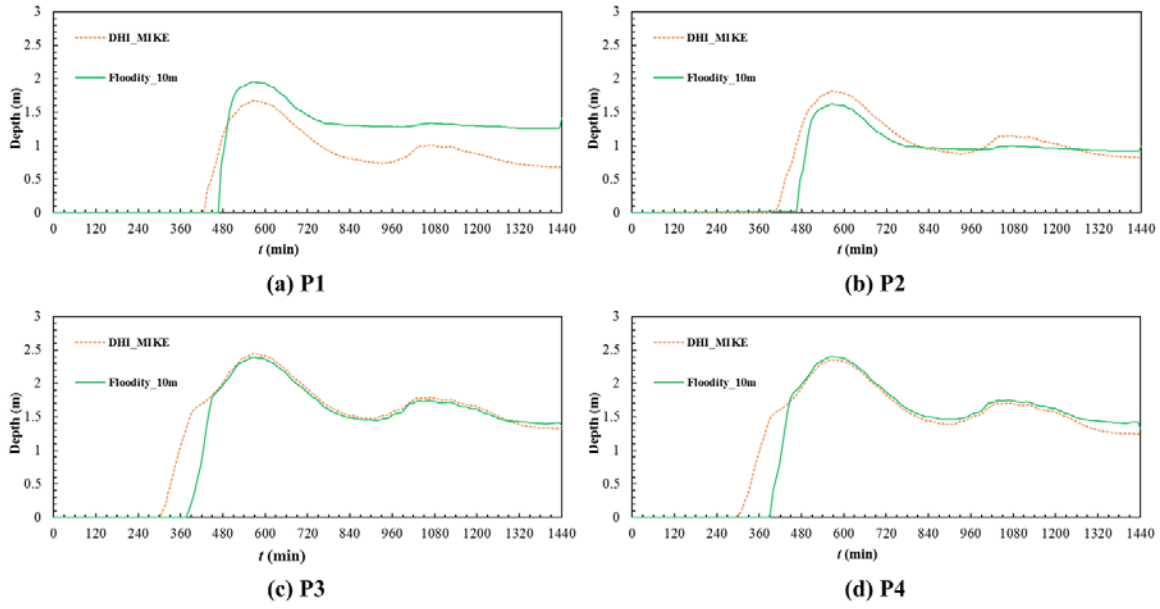


***Figure 3-16*** *Flood depth time series at detector locations P1, P2, P3 and P4 (see Fig. 5.2) simulated by DHI MIKE model and 2D adaptive unstructured mesh model with a mesh resolution 10m in scenario of 2-yr return period rainfall and extreme sea-level event.*

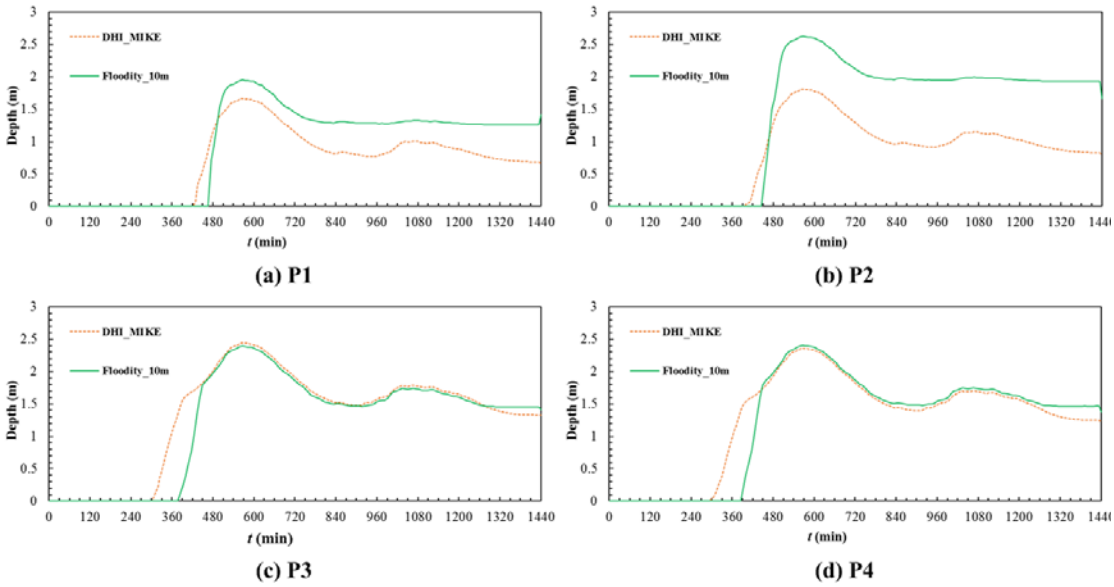


***Figure 3-17.*** *As in Figure 3-15 except in scenario of 10-yr return period rainfall and extreme sea-level event.*

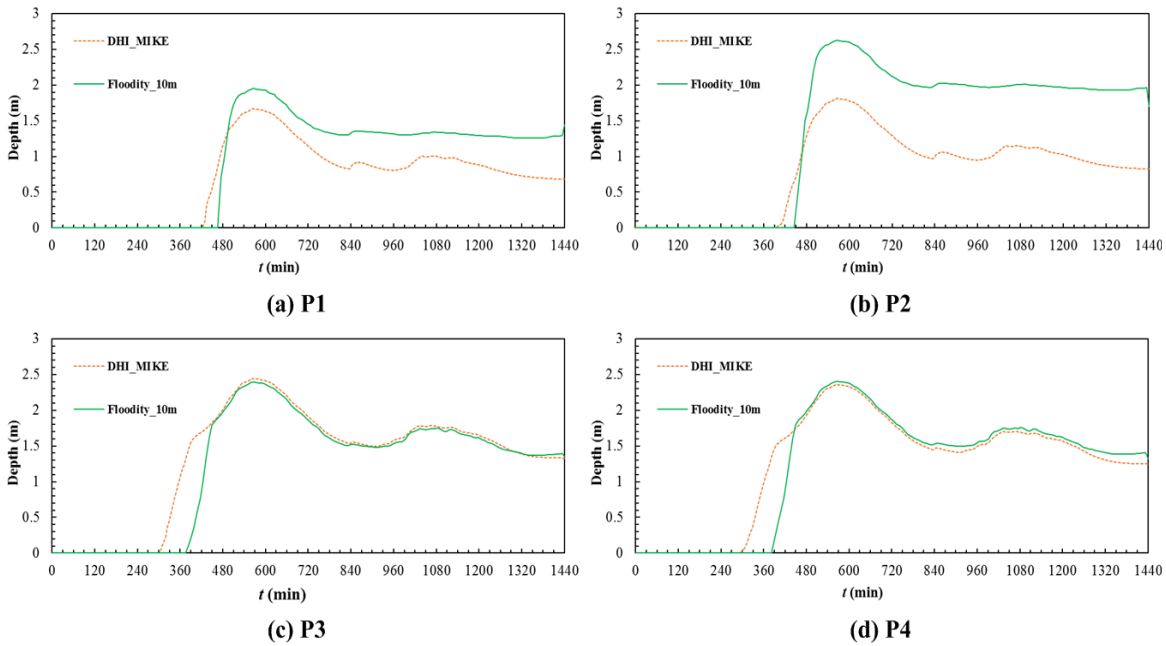


***Figure 3-18.*** *As in Figure 3-15 except in scenario of 100-yr return period rainfall and extreme sea-level event.*

*Table 3-1 Number of nodes and elements using dynamic adaptive-mesh optimization technique with the minimum mesh resolution of 20m, 10m and 5m for Flooding modelling*

| Meshing Type | Time Level $(min)$ | Node $\#(20\,m)$ | Element $\#(20\,m)$ | Node $\#(10\,m)$ | Element $\#(10\,m)$ |
|---|---|---|---|---|---|
| Fixed mesh | 0 - 120 | 13033 | 25666 | 51367 | 101939 |
| Adaptive mesh | 0 | 13033 | 25666 | 51367 | 101939 |
| | 5 | 3120 | 6095 | 8166 | 16157 |
| | 200 | 3395 | 6647 | 9064 | 17952 |
| | 600 | 4904 | 9620 | 12897 | 25548 |
| | 1200 | 4666 | 9156 | 12520 | 24806 |
| | 1440 | 4581 | 8990 | 12271 | 24315 |
| Meshing Type | Time Level $(min)$ | Node $\#(5\,m)$ | Element $\#(5\,m)$ | | |
| Fixed mesh | 0 - 120 | 204980 | 408373 | | |
| Adaptive mesh | 0 | 204980 | 408373 | | |
| | 5 | 19825 | 39446 | | |
| | 200 | 21797 | 43390 | | |
| | 600 | 29289 | 58275 | | |
| | 1200 | 28235 | 56176 | | |
| | 1440 | 27485 | 54686 | | |

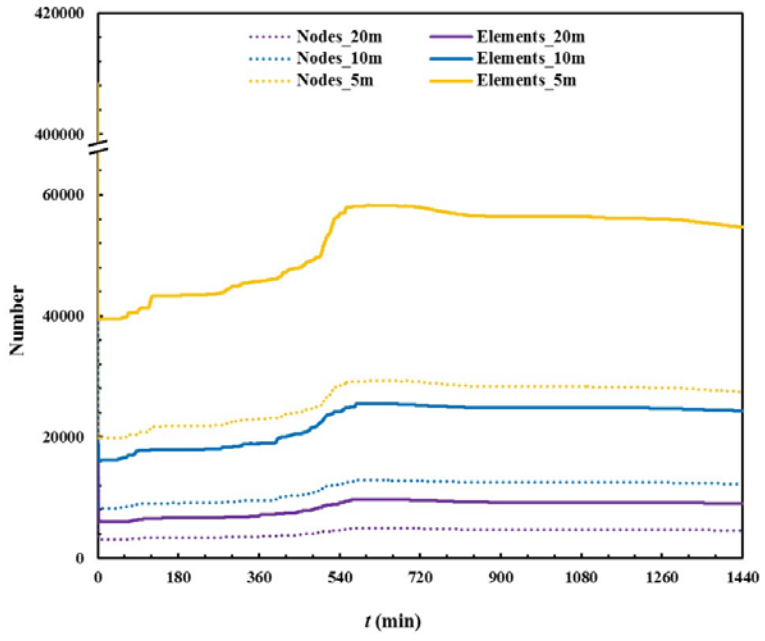


***Figure 3-19.*** *The numbers of nodes and elements used in 2D adaptive mesh modelling for mesh resolution 20m, 10m and 5m during the simulation period [0, 1440] min.*

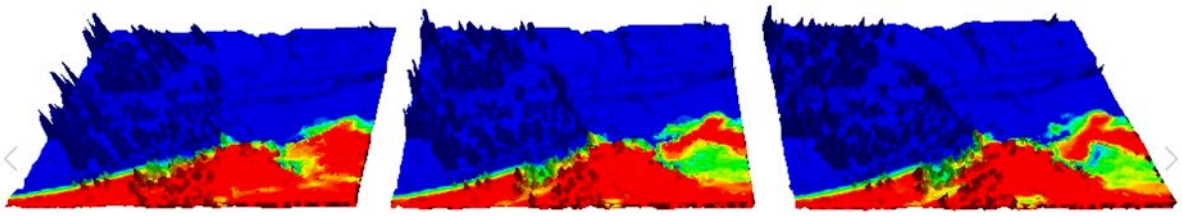

*Figure 3-20. Reduced order modelling application to Denmark case. Right: Full model, Middle: ROM with 12 POD bases, Left: 6 POD bases*

#### 3.4.5.4 Reduced Order Modelling (ROM)

The aim of Reduced Order Modelling is to replace the potentially computationally expensive forward model or chain of models with a single fast running model that is able to rapidly explore parameters (variables that effect hazards e.g. rain fall, wave height at coast) and this technology has been developed in parameterized NIROM to predict unseen case (see Xiao et al. 2017). See Figure 3-20 for its application to the Denmark test case.

However, using optimized basis functions (which is how ROM reduces the computational cost because there are relatively few of these basis functions e.g. 10-100) inserted into the forward model is an extremely long development task which has motivated the development of Non-Intrusive ROM (NIROM) which recovers the governing equations and forcing or a discrete representation of them from just a series of snapshots of the solution. Typically, a simulation involving NIROM may take seconds to minutes to run and hours to days to run or even weeks to run the full model. Another advantage of NIROM is that the accuracy can be truncated to any level of approximation as needed by the complexity of the problem. It is expected that NIROM will play a significant role in operational modelling as well in scoping out parameters for natural hazards in for example forming probability density functions of hazard effects from uncertainties (pdfs) in the forcing which can require very large numbers of simulations.

# 4 Conclusions

We have presented an initial approach to the treatment of natural hazards with a large number of innovations, such as:

1) The use of dynamically adaptive unstructured mesh adaptivity/optimization in space and time. This is demonstrated for flooding where it is shown that multi-scale capturing is possible, see Figure 3-15, in which the multi-scale nature varies in time. In this example, we show an ability to pick out the drainage ditches when the flooding even reaches them, and they influence the dynamics of the simulations. This level of resolution would not be possible without this technology.
2) Conservation mesh to mesh interpolation for dynamic mesh optimization/adaptivity and model forcing using control volume and finite element methods - exchange of forcing between different models. This is the first conservative mesh to mesh interpolation method for general control volume methods. Without it one can not have conservation of the forcing (e.g. heat momentum exchanges) between models. It is also the only way one can achieve conservation (of for example fluid volume) when using dynamic mesh optimization. It has been shown to be highly effective for mesh adaptivity and is used in all the mesh adaptive flooding results.

3) Adaptivity to buildings and topography during flooding processes - the building emerges when there is sufficient resolution as do complex topology features (see Figure 3-11). This is a limitation of existing models as they often require uniform resolution of the buildings.
4) Mesh optimization for atmospheric modelling, see Savre et al. 2015. It is suggested that future work develop large initiatives to develop next generation atmospheric flow models based on anisotropic mesh optimization/adaptivity. Our collaborators in China are already developing this technology. However, this is a grand challenge problem and will take many years to refine this technology.
5) For the spectral wave modelling space-angle adaptivity with harr wavelets, see Adam et al 2014. This deals with a possible limitation of existing spectral wave models that place resolution uniformly least angle (and often in space also). This uniformity has a large memory/storage and CPU overhead associated with it and the current approach attempts to fix this limitation of spectral wave modelling.
6) Similar to 5) but for radiation modelling used in coupling to fluids/atmospheric flows based on goals (akin to hazard assessment goals), see Soucasse et al 2017.
7) Goal based approaches to identify sensitivities of hazards based on ensembles. This pinpoints the most sensitive parameters and regions of the modelling domain in space and time that effect natural hazards. The resulting sensitivities (or importance maps) can be used in model chains to also help pinpoint issues with individual models and to help produce optimized meshes (Power et. al 2006), optimize the placement of sensors in the domain (see Che et al. 2014) or help assimilate data or optimize design/management measures of natural hazards.
8) New developments in Reduced Order Modelling (ROM): deep learning Non-Intrusive Reduced Order Modelling NIROM (see Xiao et al. 2017); parameterized NIROM to predict unseen cases (see Xiao 2017); sub-domain NIROM for large scale modelling (see Xiao submitted 2017) e.g. operation modelling needed for hazard mitigation; free surface flows with 3D modelling; ROM to scope parameters in natural hazards – uncertainty quantification. This is a major innovation and deals with the often computational speed issues involved in running large simulations and simulations needed for operational modelling (with data assimilation) or uncertainty quantification. For flooding we show that the simulations run several orders of magnitude faster than the full model. We hope to extend this approach to model atmospheric flows and are starting to develop major initiatives to model weather with partners across EU. We recommend this approach be applied to natural hazards through international collaboration.

This project has four main aspects: flooding; wave modelling; atmospheric modelling; and climate modelling. The uncertainty approach has included: Goal-based sensitivities to identify sensitivities of hazards based on ensembles; Response surface methods based on sparse grids; Reduced order models. Rather than using adjoint for the importance maps and sensitivities used in uncertainty quantification, for example, the perturbation approach is demonstrated that may be applied to model chains without changing the models within them. This also enable hazard sensitivity maps to be formed rigorously based on a functional representation of the hazard and the map becomes the importance of the different regions to the hazard. This complements hazard maps which simply show the maximum depth of water within flooding events, for example.

# 5 References


ArcGIS, 2010. Technical Reference and Documentation, Esri Software.

Aspley D.D. and Castro I.P., 1997. A limited-length-scale k-e model for the neutral and stably stratified atmospheric boundary layer. *Boundary-Layer Meteorology*, **83**, 75-98

Berger, M. J., & Oliger, J., 1984. Adaptive mesh refinement for hyperbolic partial differential equations. Journal of computational Physics. 53(3), 484-512.

Berger, M. J., & Colella, P., 1989. Local adaptive mesh refinement for shock hydrodynamics. Journal of computational Physics. 82(1), 64-84.

Borsche, R., & Klar, A., 2014. Flooding in urban drainage systems: coupling hyperbolic conservation laws for sewer systems and surface flow. International Journal for Numerical Methods in Fluids. 76(11), 789-810.

Chen, A. S., Djordjevic, S., Leandro, J., & Savic, D., 2007. The urban inundation model with bidirectional flow interaction between 2D overland surface and 1D sewer networks. In Proceedings of the 6th International Conference on Sustainable Techniques and Strategies in Urban Water Management (NOVATECH), Lyon, France, 465-472.

Chen, A. S., Evans, B., Djordjević, S., & Savić, D. A., 2012. A coarse-grid approach to representing building blockage effects in 2D urban flood modelling. Journal of hydrology. 426, 1-16.

Cotter C.J. and Shipton J., 2012: Mixed finite elements for numerical weather prediction. *Journal of Computational Physics*, **231**, 7076-7091

Dottori, F., & Todini, E., 2011. Developments of a flood inundation model based on the cellular automata approach: testing different methods to improve model performance. Physics and Chemistry of the Earth, Parts A/B/C. 36(7), 266-280.

Du, J., Zhu, J., Fang, F., Pain, C. C., & Navon, I. M., 2016. Ensemble data assimilation applied to an adaptive mesh ocean model. International Journal for Numerical Methods in Fluids. 82(12), 997-1009.

Fairall C.W., Bradley E.F., Hare J.E., Grachev A.A., Edson J.B., 2003. Bulk Parameterization of Air-Sea Fluxes: Updates and Verification for the COARE Algorithm. *Journal of Climate*, **16**, 571-591

Geiger, S., Roberts, S., Matthäi, S. K., Zoppou, C., & Burri, A., 2004. Combining finite element and finite volume methods for efficient multiphase flow simulations in highly heterogeneous and structurally complex geologic media. Geofluids. 4(4), 284-299.

George, D. L., 2011. Adaptive finite volume methods with well‐balanced Riemann solvers for modeling floods in rugged terrain: Application to the Malpasset dam‐break flood (France, 1959). International Journal for Numerical Methods in Fluids. 66(8), 1000-1018.

Geuzaine, C., & Remacle, J. F., 2009. Gmsh: A 3‐D finite element mesh generator with built‐in pre‐and post‐processing facilities. International Journal for Numerical Methods in Engineering. 79(11), 1309-1331.

Gomes, J. L. M. A., Pavlidis, D., Salinas, P., Xie, Z., Percival, J. R., Melnikova, Y., ... & Jackson, M. D., 2016. A force-balanced control volume finite element method for multiphase porous media flow modelling. International Journal for Numerical Methods Fluids. 1097-0363.

Hartnack, J. N., Enggrob, H. G., & Rungø, M., 2009. 2D overland flow modelling using fine scale DEM with manageable runtimes (p. 30). Taylor & Francis Group, London.

Hoteit I, Kohl A, 2006. Efficiency of reduced-order, time-dependent adjoint data assimilation approaches. Journal of Oceanography. 62(4), 539–550.

Hu, R., Fang, F., Salinas, P., & Pain, C.C., 2017a. Unstructured mesh adaptivity for urban flooding modelling. Ocean Modelling. Journal of Hydrology, accepted with moderate revision.

Hu, R., Fang, F., Salinas, P., Pain, C.C., Domingo, N.D. S., Mark, O. 2017b. Numerical simulation of floods from multiple sources using an adaptive unstructured mesh method applied to Greve in Denmark. Submitted to Water Resources Research.

Huang, W., Cao, Z., Pender, G., Liu, Q., & Carling, P., 2015. Coupled flood and sediment transport modelling with adaptive mesh refinement. Science China Technological Sciences. 58(8), 1425-1438.

Hunter, N. M., Bates, P. D., Néelz, S., Pender, G., Villanueva, I., Wright, N. G., Liang, D., Falconer, R. A., Lin, B., Waller, S., Crossley, A. J. & Mason, D. C., 2008. Benchmarking 2D hydraulic models for urban flooding. Proc. Inst. Civil Eng. Water Manage. 161 (1), 13–30.

Jackson, M., Percival, J., Mostaghimi, P., Tollit, B., Pavlidis, D., Pain, C., ... & Blunt, M., 2015. Reservoir modeling for flow simulation by use of surfaces, adaptive unstructured meshes, and an overlapping-control-volume finite-element method. SPE Reservoir Evaluation & Engineering. 18(02), 115-132.

Leandro, J., Chen, A. S., & Schumann, A., 2014. A 2D parallel diffusive wave model for floodplain inundation with variable time step (P-DWave). Journal of Hydrology. 517, 250-259.

Liang, Q., Borthwick, A. G. L., & Stelling, G., 2004. Simulation of dam‐and dyke‐break hydrodynamics on dynamically adaptive quadtree grids. International journal for numerical methods in fluids. 46(2), 127-162.

Liang, D., Falconer, R. A., & Lin, B., 2007. Coupling surface and subsurface flows in a depth averaged flood wave model. Journal of Hydrology. 337(1), 147-158.

Liang, Q., & Borthwick, A. G., 2009. Adaptive quadtree simulation of shallow flows with wet–dry fronts over complex topography. Computers & Fluids. 38(2), 221-234.

Liang, Q., 2012. A simplified adaptive Cartesian grid system for solving the 2D shallow water equations. International Journal for Numerical Methods in Fluids. 69(2), 442-458.

Maronga B., Gryschka M., Heinze R., Hoffman F., Kanani-Suhring F., Keck M., Ketelsen K., Letzel M.O., Suhring M., Raasch S., 2015. The Parallelized Large-Eddy Simulation Model (PALM) version 4.0 for atmospheric and oceanic flows: model formulation, recent developments, and future perspectives. *Geoscientific Model Development*, **8**, 2515-2551

Mascarenhas, F. C. B., Toda, K., Miguez, M. G., & Inoue, K., 2005. Flood risk simulation, WIT, Southampton, Boston.

Matthai, S. K., Mezentsev, A. A., & Belayneh, M., 2007. Finite element-node-centered finite-volume two-phase-flow experiments with fractured rock represented by unstructured hybrid-element meshes. SPE Reservoir Evaluation & Engineering. 10(06), 740-756.

Medeiros, S. C., & Hagen, S. C., 2013. Review of wetting and drying algorithms for numerical tidal flow models. International journal for numerical methods in fluids. 71(4), 473-487.

Pain, C. C., Umpleby, A. P., De Oliveira, C. R. E., & Goddard, A. J. H., 2001. Tetrahedral mesh optimisation and adaptivity for steady-state and transient finite element calculations. Computer Methods in Applied Mechanics and Engineering. 190(29), 3771-3796.

Pavlidis D., Gorman G.J., Gomes J.L.M.A., Pain C.C, ApSimon H., 2010. Synthetic-Eddy Method for Urban Atmospheric Flow Modelling. *Boundary-Layer Meteorology*, **136**, 285-299

Pavlidis, D., Xie, Z., Percival, J. R., Gomes, J. L., Pain, C. C., & Matar, O. K., 2014. Two-and three-phase horizontal slug flow simulations using an interface-capturing compositional approach. International Journal of Multiphase Flow. 67, 85-91.

Piggott, M. D., Pain, C. C., Gorman, G. J., Power, P. W., & Goddard, A. J. H., 2005. h, r, and hr adaptivity with applications in numerical ocean modelling. Ocean Modelling. 10(1), 95-113.

Popinet, S., 2012. Adaptive modelling of long-distance wave propagation and fine-scale flooding during the Tohoku tsunami. Natural Hazards and Earth System Sciences. 12(4), p.1213.

Salinas, P., Pavlidis, D., Xie, Z., Jacquemyn, C., Melnikova, Y., Jackson, M. D., & Pain, C. C., 2017. Improving the robustness of the control volume finite element method with application to multiphase porous media flow. International Journal for Numerical Methods in Fluids.

Savre J., Percival J., Herzog M. and Pain C.C, 2016: Two-dimensional evaluation of ATHAM-Fluidity, a nonhydrostatic atmospheric model using mixed continuous/discontinuous finite elements and anisotropic grid optimisation. *Monthly Weather Review*, **144**, 4349-4372

Schmitt, T. G., Thomas, M., & Ettrich, N., 2004. Analysis and modeling of flooding in urban drainage systems. Journal of Hydrology. 299(3), 300-311.

Schubert, J. E., Sanders, B. F., Smith, M. J., & Wright, N. G., 2008. Unstructured mesh generation and landcover-based resistance for hydrodynamic modeling of urban flooding. Advances in Water Resources. 31(12), 1603-1621.

Seifert A. and Beheng K.D., 2006: A two-moment cloud microphysics parameterization for mixed-phase clouds. Part 1: Model description. *Meteorology and Atmospheric Physics*, **92**, 45-66

Semadeni-Davies, A., Hernebring, C., Svensson, G., & Gustafsson, L.-G., 2008. The impacts of climate change and urbanisation on drainage in helsingborg, swede: Suburban stormwater. Journal of Hydrology.350, 114-125.

Smith, L. S., Liang, Q., & Quinn, P. F., 2015. Towards a hydrodynamic modelling framework appropriate for applications in urban flood assessment and mitigation using heterogeneous computing. Urban Water Journal. 12(1), 67-78.

Soledad, B. R., 2014. Modelling flooding from the sea interacting with the drainage system under the influence of combined flood hazards to develop risk management strategies for the coastal region of Greve, Denmark. (Master's thesis, University of Nice Sophia Antipolis, Nice, France).

Son, A. L., Kim, B., & Han, K. Y., 2016. A Simple and Robust Method for Simultaneous Consideration of Overland and Underground Space in Urban Flood Modeling. Water, 8(11), 494.

Smagorinsky J., 1963. General Circulation Experiments with the Primitive Equations. *Monthly Weather Review*, **91**, 99-163

Smith, L. S., Liang, Q., & Quinn, P. F., 2015. Towards a hydrodynamic modelling framework appropriate for applications in urban flood assessment and mitigation using heterogeneous computing. Urban Water Journal. 12(1), 67-78.

Su, K., Latham, J. P., Pavlidis, D., Xiang, J., Fang, F., Mostaghimi, P., Percival, J.R, Pain, C. C., & Jackson, M. D., 2015. Multiphase flow simulation through porous media with explicitly resolved fractures. Geofluids. 15(4), 592-607.

Van Dijk, E., van der Meulen, J., Kluck, J., & Straatman, J. H. M., 2014. Comparing modelling techniques for analysing urban pluvial flooding. Water science and technology. 69(2), 305-311.

Wang, J. P., & Liang, Q., 2011. Testing a new adaptive grid‐based shallow flow model for different types of flood simulations. Journal of Flood Risk Management. 4(2), 96-103.

Xie, Z., Hewitt, G. F., Pavlidis, D., Salinas, P., Pain, C. C., & Matar, O. K., 2017. Numerical study of three-dimensional droplet impact on a flowing liquid film in annular two-phase flow. Chemical Engineering Science. 166, 303-312.

Zhang, T., Feng, P., Maksimović, Č., & Bates, P. D., 2016. Application of a three-dimensional unstructured-mesh finite-element flooding model and comparison with two-dimensional approaches. Water Resources Management. 30(2), 823-841.

Zheng, J., Zhu, J., Wang, Z., Fang, F., Pain, C. C., & Xiang, J., 2015. Towards a new multiscale air quality transport model using the fully unstructured anisotropic adaptive mesh technology of Fluidity (version 4.1. 9). Geoscientific Model Development. 8, 3421-3440.

Zhou, F., Chen, G., Huang, Y., Yang, J. Z., & Feng, H., 2013. An adaptive moving finite volume scheme for modeling flood inundation over dry and complex topography. Water Resources Research. 49(4), 1914-1928.

Xie Z.-T. and Castro I.P., 2008. Efficient Generation of Inflow Conditions for Large Eddy Simulation of Street-Scale Flows. *Flow, Turbulence and Combustion*, **81**, 449-470